Aalborg Universitet

Modeling, Stability Analysis, and Control of Wind Generation System Connected to Weak Grid

Huang, Liang

MODELING, STABILITY ANALYSIS, AND CONTROL OF WIND GENERATION SYSTEM CONNECTED TO WEAK GRID

BY
LIANG HUANG

DISSERTATION SUBMITTED 2023

AALBORG UNIVERSITY
DENMARK

Modeling, Stability Analysis, and Control of Wind Generation System Connected to Weak Grid

Ph.D. Dissertation

Liang Huang

Curriculum Vitae

Liang Huang

Liang Huang received the B.S. and M.S. degrees in electrical engineering from Northeastern University, Shenyang, China, in 2013 and 2015, respectively. From 2015 to 2019, he worked as an R&D engineer in Welling Motor R&D Center, Shanghai, China. Since 2020, he has been working toward the Ph.D. degree in electrical engineering from Aalborg University, Aalborg, Denmark. In the meanwhile, he was a visiting scholar in the L2EP laboratory at Ecole Centrale de Lille (France) from March 2022 to May 2022. His current research interests include small-signal modeling, stability, and control of grid-connected inverters/PMSGs/DFIGs in wind energy conversion systems.

Curriculum Vitae

Abstract

System inertia and voltage stability are two main characteristics of the electrical power system. In traditional power systems, the system inertia depends on the kinetic energy in the rotor of the traditional synchronous generators (SGs). However, as the penetration of wind power generation rises, numerous SGs will be replaced by converter-interfaced generators (CIGs). Thus, the system inertia will be reduced significantly, which may threaten the frequency stability. Moreover, the long distance between the main grid and the wind farm usually causes a large transmission impedance and a low short-circuit ratio (SCR). In the low-SCR grid, maintaining voltage stability is a challenge. Therefore, this Ph.D. project focuses on inventing improved control solutions to enhance the voltage stability and frequency stability of wind generation systems connected to weak grids.

Typically, grid-connected inverters in wind generation systems need a phase-locked loop (PLL) for voltage synchronization. This PLL-based control method is usually called grid-following (GFL) control method, which is the first research target of the thesis. Specifically, small-signal impedance models and state-space models of GFL inverters are built to analyze the voltage instability mechanism. According to the small-signal impedance model, it is found that the positive feedback introduced by the PLL can lead to negative resistance characteristics, which are identified as the reason of the instability. In order to mitigate the positive feedback and weaken the negative resistance characteristic, a double-PLL-based impedance reshaping control method is proposed, which can not only extend the small-signal stability range, but also improve the dynamic performance of the PLL. Thus, the voltage instability issue of the conventional GFL inverters in weak grids can be solved.

Secondly, grid-forming (GFM) control methods become the next research focus of the thesis, because GFM inverters are necessary for low-inertia grids to improve the frequency stability. Considering that GFM control schemes have not been unified or standardized yet, three commonly used GFM control schemes are compared initially. It is found that a virtual-admittance-based GFM control scheme has a wider stability range than a virtual-impedance-based scheme and the typical control scheme without a virtual impedance.

So, the virtual-admittance-based GFM control scheme is chosen to be used. Then, the parameter design method for the virtual admittance is studied and a simple design method is proposed. By using the proposed design approach, GFM inverters are able to be stable within a wide range of SCR. Moreover, it is found that GFM inverters with a typical current reference limiting method suffer from instability issues during large grid disturbances. To solve this problem, a power-angle-based overcurrent protection approach is proposed, which can maintain the stability of GFM inverters during large grid frequency or voltage disturbances. Thus, with the proposed overcurrent protection method, GFM inverters can operate stably even under large grid disturbances.

Afterwards, to study stability issues of wind generators, small-signal models of Type-3 and Type-4 wind generation systems are built. In terms of Type-4 wind generation systems, only considering the grid-side converter (GSC) is enough to derive the small-signal impedance model and perform the stability analysis. However, for Type-3 wind generation systems, it is difficult to obtain the full-order impedance model of the doubly-fed induction generator (DFIG) system due to both dc-side and ac-side couplings between the GSC and the rotor-side converter (RSC). To address this difficulty, a two-port-network-based decoupled impedance modeling method is proposed, which is able to decouple the ac-side coupling so that the RSC, GSC, and dc-link coupling can be modeled separately. By using the proposed modeling approach, the impact of the dc-link coupling in the DFIG system with either GFL or GFM control can be analyzed quantitatively. Thus, according to small-signal models of PMSG and DFIG systems, the small-signal stability of grid-connected wind generators can be analyzed accurately.

Then, the proposed improved GFL and GFM control methods are applied to two paralleled permanent magnet synchronous generator (PMSG)-based Type-4 wind generators, and it is found that the stability and transient performance of GFL and GFM Type-4 wind generators can be improved. So, the voltage and frequency stability requirements mentioned in the beginning are basically satisfied. Finally, a more realistic case study of Anholt Offshore Wind Power Plant is carried out, which shows good stability and transient performance of the proposed GFL and GFM control solutions.

The outcomes of this Ph.D. project will be helpful to address stability challenges of power systems with a high percentage of wind power generation.

Resumé

System-inerti, frekvens- og spændingsstabilitet er tre vigtige hovedkarakteristika ved det moderne elektriske energisystem. I det traditionelle el-system afhænger system-inertien af den kinetiske energi i rotoren på de traditionelle synkrone generatorer (SG'er). Men efterhånden som udbredelsen af vindkraftproduktion stiger, vil adskillige SG'er blive erstattet af effektelektroniske omformer-baserede (inverter) generator (CIG'er) som typisk er i vindmøller og sol-celler. Dermed vil system-inertien blive reduceret væsentligt, hvilket kan true frekvensstabiliteten, som er afgørende for et sikkert el-net. Desuden forårsager den lange afstand mellem hoved el-nettet og de fremtidige vindmølleparker normalt en stor transmissions-impedans og som dermed har et lavt kortslutningsforhold (SCR). I et lav-SCR-net er det en udfordring at opretholde ovennævnte spændingsstabilitet. Derfor fokuserer dette Ph.D.-projekt på at finde forbedrede styringsløsninger til at forbedre spændings- og frekvensstabiliteten af vindproduktionssystemer forbundet til svage net.

Typisk bruger net-tilsluttede invertere i vindmøller en faselåst kontrolsløjfe (PLL) til at synkronisere med el-nettets spænding for at være tilsluttet sikkert. Denne PLL-baserede kontrolmetode kaldes normalt grid-following (GFL) kontrol og denne kontrolmetode er afhandlingens første forskningsmål at analysere. I den sammenhæng anvendes småsignal-impedansmodeller og state-space-modeller af GFL-invertere til at analysere spændings-ustabiliteten i el-nettet. Småsignal-impedansmodellerne viser i afhandlingen, at en positiv feedback introduceret af PLL'en kan føre til negative modstands-karakteristika, som kan give anledning til spændings-ustabilitet. For at afbøde denne positive feedback og svække den negative modstands-karakteristik af inverteren foreslås en dobbelt-PLL-baseret impedanskompensering, som nemt kan inkluderes i kontrolmetoden, som ikke kun forbedrer stabilitetsområdet ved små forstyrrelser, men forbedrer også PLL'ens dynamiske ydeevne generelt. Således kan spændings-ustabiliteten for de konventionelle GFL-invertere i svage el-net løses.

Et andet aspekt i afhandlingen er grid-forming (GFM) kontrolmetoder, hvor inverteren opfører sig som en traditionel synkron generator og viser sig nødvendige i lavinerti-net for at kunne forbedre frekvensstabiliteten og

kunne starte el-nettet op. I betragtning af, at GFM-kontrol metoderne ikke er blevet standardiseret endnu, sammenlignes i afhandlingen tre almindeligt kendte GFM-kontrol-metoder indledningsvis. Det viser sig, at et virtuelt admittans-baseret GFM-kontrol metode har et bedre stabilitetsområde end et virtuel-impedans-baseret metode. Derfor er den virtuelle admittans baserede GFM-kontrol metode valgt til at blive undersøgt nærmere i afhandlingen. Efterfølgende studeres metoder til at designe/bestemme parametrene for den virtuelle admittans som viser sig muligt at gøre simpelt. Den foreslåede design-metode gør GFM-invertere i stand til at være stabile inden for en bred vifte af SCR. Desuden viser det sig, at GFM-invertere, som typisk anvender en begrænsningsmetode for strøm-referencen, ofte lider af ustabilitetsproblemer under store net-forstyrrelser. For at løse dette problem foreslås en adaptiv effektvinkel-baseret overstrømsbeskyttelsesmetode, som kan opretholde stabiliteten af GFM-invertere selv under store netspændings- eller frekvens-forstyrrelser. Med den foreslåede overstrømsbeskyttelsesmetode kan GFM-invertere således fungere meget stabilt selv under store netforstyrrelser.

Dernæst studeres stabilitetsproblemer for to typer vindmøllegeneratorer, hvor der udvikles småsignalmodeller af Type-3 og Type-4 vindmølle systemer. Med hensyn til Type-4 vindmøllesystemer er der i afhandlingen kun overvejelser omkring netside-omformeren (GSC) i forhold til at udlede småsignalimpedansmodellerne og udføre en stabilitetsanalyse. For Type-3 vindmølle systemet er det imidlertid vanskeligt at udlede en impedansmodel af fuld orden for den dobbeltfødede induktions generator (DFIG) på grund af at der eksisterer både DC-side og AC-side koblinger mellem netside-omformeren (GSC) og rotor-side konverteren (RSC). For at løse denne vanskelighed foreslås en to-port-netværksbaseret afkoblet impedans-modelleringsmetode, som er i stand til at afkoble AC-siden, så RSC, GSC og dc-link-koblingen kan modelleres separat – for derefter at bruge superpositions-princippet til at få den fulde model. Ved at bruge den foreslåede modelleringsmetode kan indvirkningen af dc-link-koblingen i DFIG-systemet med enten GFL eller GFM-styringen analyseres kvantitativt og kvalitativt. Småsignalmodellerne for Permanent Magnet Synkron-generatorer (PMSG i Type 4) og DFIG-systemer kan bruges til at analysere nøjagtig net-tilsluttede vindmølle systemers stabilitet.

De foreslåede GFL og GFM-kontrolmetoder anvendes derefter på to parallelle Type-4 vindmølle generatorer, og det viser sig, at stabiliteten og ydeevnen af GFL og GFM bliver væsentlig forbedret ved både svage og stærke el-net, hvorfor spændings- og frekvensstabilitets-kravene, som er nævnt i begyndelsen af afhandlingen grundlæggende er opfyldt. Endelig udføres et mere realistisk studie af Anholt Hav vindmølle park, som også viser god stabilitet ydeevne, når de foreslåede GFL og GFM-kontrolløsninger anvendes.

Resultaterne af dette Ph.D. projekt er brugbar til at løse fremtidige stabilitetsudfordringer i el-systemer med en høj procentdel af vindkraftproduktion og med svage el-net.

Contents

Contents

Contents

Preface

The content presented in this dissertation is a summary of the outcome of the Ph.D. project *"Modeling, Stability Analysis, and Control of Wind Generation System Connected to Weak Grid"*, which was carried out at AAU Energy, Aalborg University, Denmark.

First of all, I would like to express my sincere appreciation to my supervisor, Professor Frede Blaabjerg, for his excellent guidance, inspiration, and encouragement throughout my entire Ph.D. study. His profound knowledge and outstanding leadership impressed me a lot, which helps me to overcome many difficulties in my Ph.D. project and come up with lots of interesting ideas. Besides, I would like to thank my co-supervisors, Associate Professor Dao Zhou and Postdoc Chao Wu, for their remarkable guidance and patient assistance during my Ph.D. study. With their guidance, I learned how to write a high-level academic paper and make a presentation in a logical manner. These skills will help me to become a better researcher.

I would also like to thank Professor Xavier Guillaud for providing me an opportunity to study abroad at Ecole Centrale de Lille, France. In Xavier's research group, we had a lot of discussions about the different grid-following and grid-forming control methods with Ph.D. student Yahya Lamrani and his colleagues. Their valuable input improved my understanding of my research topics. I feel grateful for having been there.

Moreover, I would like to pay my special thanks to Ph.D. students Meng Chen, Shan He, Jing Yuan, Yubo Song, Daniela Pagnani, Dimitrios Dimitropoulos, Chaochao Song, Yun Yu, Liang Zhao, Shiyi Liu, and all colleagues and secretaries in the department of AAU Energy. With their help and support, work and life become more pleasant during my Ph.D. study period.

Finally, I would like to express my deep gratitude to my family, who have always supported me in my life. Without their support and encouragement, this work would not have been accomplished.

Liang Huang
Aalborg University, February 12, 2023

Preface

Part I

Report

Chapter 1

Introduction

1.1 Background

In the past decades, conventional fossil-based centralized power generation plants are deemed unsustainable because of the predicted drain of fossil-based resources and global warming issues. Consequently, many companies and institutions have been working on research and development of renewable energy sources. Thus, the modern electrical power system is in a dramatic change from centralized generation to distributed renewable energy generations, such as wind power, solar, bioenergy, geothermal, and tidal power plants [1]. Among these renewable energy sources, wind power could become the world's foremost generation source, because there are abundant wind resources around the world and wind energy can easily be obtained without much physical restriction. According to the plan of the International Renewable Energy Agency, the world's installed wind power capacity is forecasted to be 6000 GW by 2050 [2]. In respect to Europe, the total wind energy share is expected to be nearly 50% in 2050 [3], that is around 400 GW, as illustrated in Fig. 1.1. Besides, it is reported by the Danish Energy Agency that the electricity supply capacity of wind power in Denmark is expected to be 12 GW by 2030, as shown in Fig. 1.2. To this end, the renewables share of the electricity consumption in Denmark is expected to reach 111% in 2030 [4].

As the penetration of wind power generation rises, numerous centralized and large synchronous generators (SGs) will be replaced by distributed converter-interfaced generators (CIGs). However, the general features and characteristics of CIGs are quite different from that of the SGs [5]. Specifically, the traditional SGs have a strong synchronous frequency coupling with the grid. When the grid frequency is varied because of the load variation, the rotor speed of the SG is also changed. Thus, the kinetic energy stored in the rotor plays the role of being an energy buffer to support the grid frequency, so

3

Electricity mix to 2050 in Europe
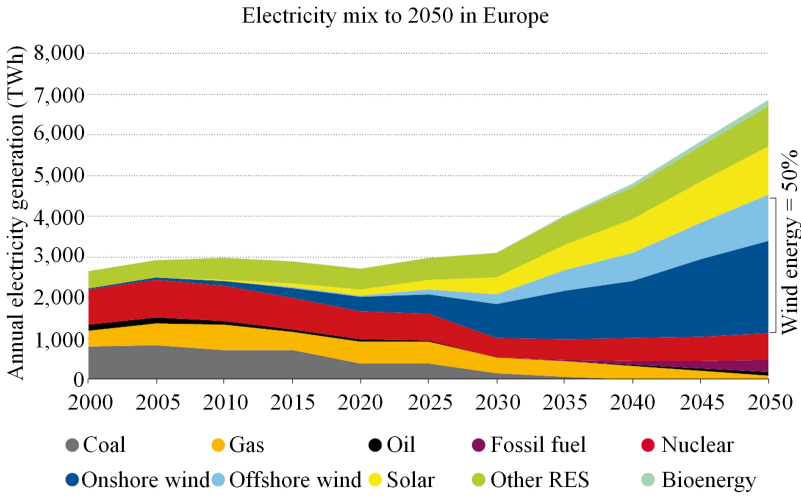
Fig. 1.1: Electricity production mix in Europe. Source: [3].

Capacity of solar and wind power to 2030 in Denmark (MW)
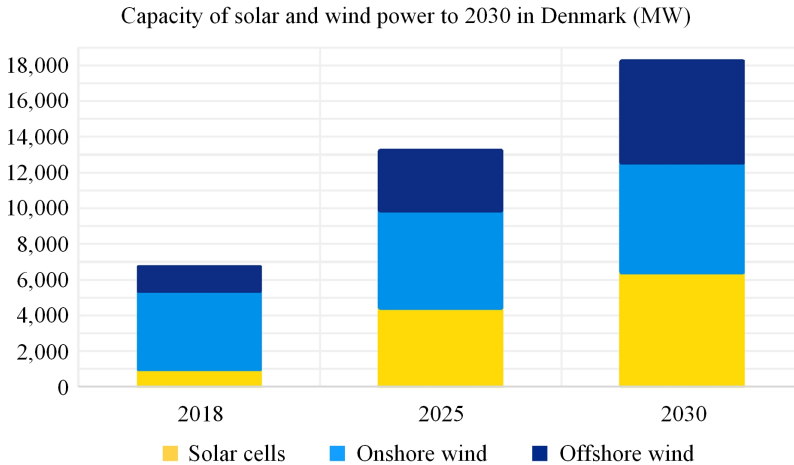
Fig. 1.2: Electricity supply capacity of wind power and solar power in Denmark. Source: [4].

the frequency stability of the power grid can be maintained in this way. Differently, the wind generators have no synchronous frequency coupling with the grid, because they are connected to the power grid via a back-to-back power electronic converter, which completely follows the grid frequency by using a phase-locked loop (PLL). Thus, when the grid frequency is reduced, the wind generators do not provide frequency support to the grid. Hence, the frequency stability of the power grid with a high percentage of wind power generation is hard to be maintained [6]. Besides, although the CIGs with the
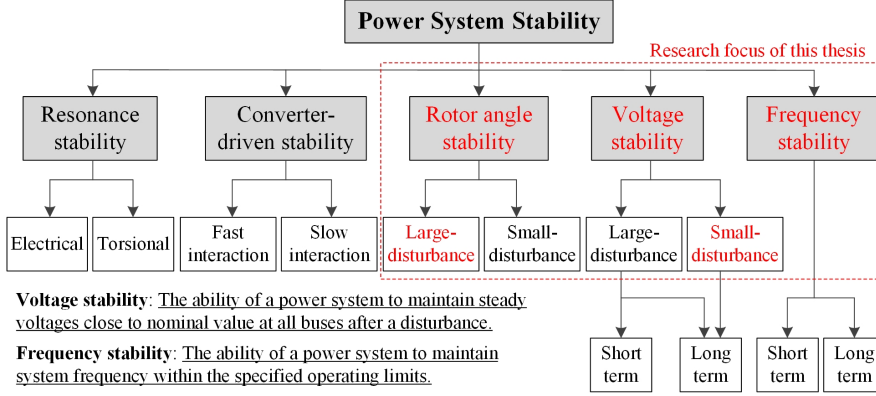
Fig. 1.3: Classification and definition of power system stability. Source: [9].

power synchronization control can enhance the frequency stability, they have rotor angle instability issues under weak grid or grid fault conditions.

Moreover, since the locations with abundant wind resources are often far away from the load center, the wind farms are usually placed distant from the main grid. Thus, transmission lines between the main grid and the wind farm would be very long. However, the long-distance transmission lines cause large transmission impedances and low short-circuit ratios (SCRs), which may threaten the voltage stability [7]. For example, many sub-synchronous oscillation events associated with wind power plants connected to weak grids have occurred in America, China, Canada, Australia, United Kingdom (UK) in recent ten years [8].

Overall, the power system consisting of massive CIGs may encounter different kinds of stability issues, including resonance stability, converter-driven stability, rotor angle stability, voltage stability, and frequency stability [9], as illustrated in Fig. 1.3. Besides, these stability issues can be further classified as fast interaction, slow interaction, small-disturbance, large-disturbance, short-term, and long-term stability issues. So, the stability problems have become key problems of future power systems with a high proportion of CIGs [10]. Therefore, more demanding specifications (i.e., Grid Codes) have continuously been issued and updated [11].

1.1.1 Requirements of Grid Codes

In order to ensure the power system operates safely, the grid voltage and frequency must meet the Grid Codes. Table 1.1 presents the requirements for the grid voltage in UK Grid Codes [12]. According to the Grid Codes, the voltage on the 400 kV part of the power system at each connection site will normally remain within ±5% of the nominal value. Voltages on the 275 kV and 132 kV at each connection site will remain within ±10% of the nominal

Table 1.1: Requirements for grid voltage variations in UK Grid Codes [12].

Nominal Voltage	Normal Operating Range
400 kV	400 kV $\pm5\%$
275 kV	275 kV $\pm10\%$
132 kV	132 kV $\pm10\%$
< 132 kV	$V_N \pm 6\%$

Table 1.2: Requirements for grid frequency variations in UK Grid Codes [12].

Frequency Range	Requirements
51.5 - 52 Hz	Operation for at least 15 minutes
51 - 51.5 Hz	Operation for at least 90 minutes
50.5 - 51 Hz	Continuous operation is required
49.5 - 50.5 Hz	Normal operation
49 - 49.5 Hz	Continuous operation is required
47.5 - 49 Hz	Operation for at least 90 minutes
47 - 47.5 Hz	Operation for at least 20 seconds
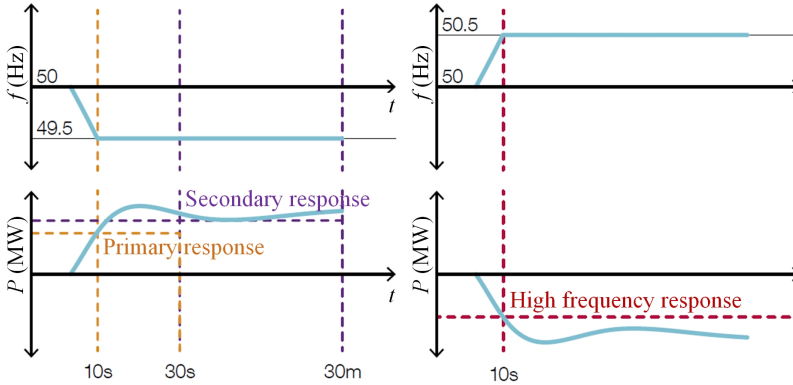
Fig. 1.4: Frequency dynamic response requirements for power plants. Source: [13].

value. Besides, voltages below 132 kV at each connection site should remain within $\pm6\%$ of the nominal value. In summary, the grid voltage must be controlled within $\pm5\% \sim 10\%$ of the nominal value. Otherwise, the voltage stability cannot be maintained [12].

Table 1.2 provides the requirements for grid frequency in UK Grid Codes. According to the Grid Codes, the frequency of the power system shall be controlled within $49.5 \sim 50.5$ Hz normally. For exceptional circumstances, the frequency could rise to 52 Hz or fall to 47 Hz but they should meet the requirements listed in Table 1.2. When the grid frequency is beyond $47 \sim 52$ Hz, the frequency stability of the power system cannot be maintained [12].

Table 1.3: LVRT requirements for offshore transmission systems in UK Grid Codes [12].

Voltage magnitude	Requirements
0.9 - 1.0 p.u.	Normal operation
0.85 p.u.	Operation for at least 3 minutes
0.80 p.u.	Operation for at least 2.5 seconds
0.50 p.u.	Operation for at least 0.71 seconds
0.15 p.u.	Operation for at least 0.14 seconds
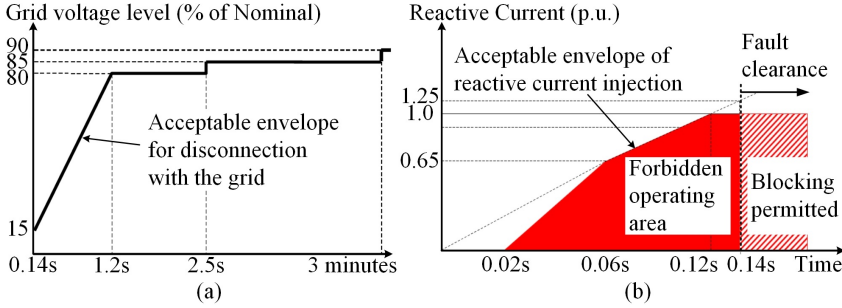
Fig. 1.5: Requirements of converter-based plant under grid fault conditions (a) LVRT requirements; (b) Fast reactive current injection requirements. Source: [14] and [15].

Moreover, to assist in maintaining the frequency stability of power systems, the Grid Codes also specify the frequency dynamic response requirements for power plants. It defines 'Primary', 'Secondary', and 'High frequency' responses as the change of the active power in response to the change of frequency, as illustrated in Fig. 1.4, where Primary response is the minimum increase within 10 seconds and sustainable for 30 seconds, Secondary response is the minimum increase within 30 seconds and sustainable for 30 minutes. Besides, High frequency response is the minimum decrease within 10 seconds and sustained thereafter [13].

Furthermore, Table 1.3 and Fig. 1.5(a) show the low-voltage ride-through (LVRT) requirements for offshore transmission systems in UK Grid Codes. It requires that generation units should remain connection with the grid for at least a certain time during grid voltage fault [14]. Besides, Fig. 1.5(b) shows a minimum requirement of the reactive current injection for converter-based plants. It requires that the converter should inject reactive current fastly during the grid fault [15]. However, as the penetration of wind power generation rises, meeting above requirements becomes more challenging [16].

1.1.2 Development of Wind Turbine Generation Systems

Because of the predicted exhaustion of fossil-based resources and global warming issues, wind energy generation will grow year by year in the power

system. The development of wind turbine (WT) technology has lasted more than 40 years. In 1990s, the WT generation systems were mostly employed by fixed speed WT generators [17]. However, their wind energy capture ability is relatively low and can only provide limited service for the power grid [18]. After 2000, variable-speed WT generators with power converters were widely used in global markets, because they have higher wind energy capture ability, efficiency, and they could be better integrated into the power grid [19]. At present, the WT generators can be divided into the following four types.

Type-1 wind generators are squirrel cage induction generators driven by fixed-speed WTs. Fixed-speed WTs are the most general utility-scale WTs in operation. The WTs operate with tiny variations of the rotor speed. They employ squirrel-cage induction generators connected to the grid directly. Although they are relatively robust and reliable, this technology has low wind energy capture ability and it lacks power controllability [20, 21].

Type-2 wind generators are induction generators with variable external rotor resistance driven by variable-speed, pitch-regulated WTs. The variable-speed WTs can work at a wider range of the rotor speed. Power control and speed control allow these WTs to obtain more energy than fixed-speed WTs. Nevertheless, the slip power on the rotor resistance is lost as heat [21].

Type-3 wind generators are doubly-fed induction generators (DFIGs) with partial-scale converters, driven by variable-speed, pitch-regulated WTs. DFIG turbines are controlled by a back-to-back converter on the rotor side [21]. Flux vector or voltage vector control allows decoupled reacitve and active power and maximum power point tracking (MPPT) [22, 23]. Because the converter just handles the power on the rotor side, only partial power is enough for the converter, which can reduce the cost of the overall system.

Type-4 wind generators are synchronous or asynchronous (induction) generators with full-scale converter interfaces, driven by variable-speed and pitch-regulated WTs. In Type-4 WT generators, a back-to-back converter connects the WT and grid [24, 25]. The WTs can be equipped with synchronous or asynchronous generators [26]. Compared with asynchronous generators, permanent magnet synchronous generators (PMSGs) have higher efficiency. Besides, the gear box can be eliminated by using the direct-drive PMSGs [27].

Compared with Type-1 and Type-2 WT generators, Type-3 and Type-4 WT generators have higher energy capture ability and controllability. Hence, they have become major commercial wind generators on the market, which are widely used by global WT manufacturers, such as Vestas, General Electric, Siemens Gamesa, and Goldwind [19]. Wind power plants including Type-4 or Type-3 wind generators are presented in Fig. 1.6, where Type-3 wind generators include a rotor-side converter (RSC) and a grid-side converter (GSC), while Type-4 wind generators include a machine-side converter (MSC) and a GSC. As shown in Fig. 1.6, either the grid-following control or the grid-forming control can be applied to Type-4 and Type-3 wind generators. Since
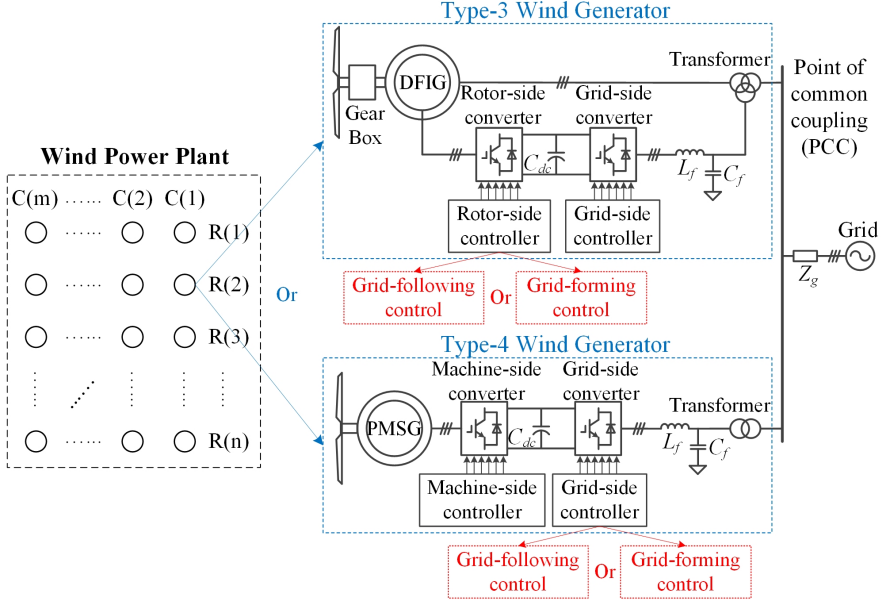
Fig. 1.6: Type-4 or Type-3 wind generation system in a wind power plant with two possible control approaches.

the grid-following/forming control scheme on Type-4 and Type-3 generators are similar, they do not need to be differentiated especially. The general grid-following control scheme and the grid-forming control scheme will be discussed in the following sections.

1.1.3 State-of-the-Art of Grid-Following Inverter

Grid-following (GFL) control scheme is the most common applied control schemes of WT generators. The general GFL control scheme on the GSC of a Type-4 wind generator is presented in Fig. 1.7, where a PLL is utilized to estimate the phase of the voltage at the point of common coupling (PCC) to keep synchronization with the grid. Besides, the d-axis and q-axis current components are regulated by using vector current control, which makes the output reactive and active power to be controlled accordingly.

Since the GFL control approach relies on the estimated phase of the PCC voltage, it works well in strong grids, where the PCC voltage is stable and unchangeable. However, in weak grid cases, a higher power flow from the converter to the grid leads to more severe voltage variations at the PCC due to the large transmission impedance, which may challenge the voltage stability. To study the instability issues of the GFL converter, many modeling and control methods have been proposed in the existing research [28–36].
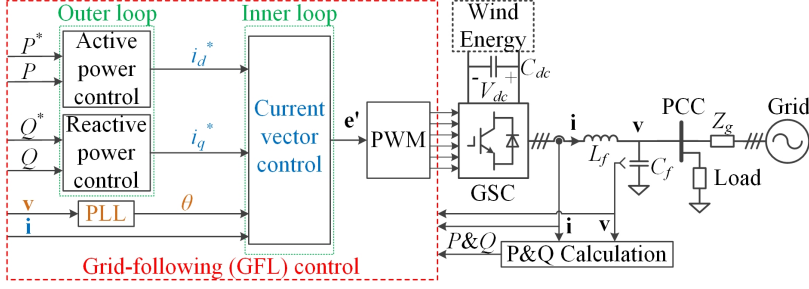
Fig. 1.7: General control scheme of a grid-following converter.

To study the stability issues, the time-domain state-space model [28] and the frequency-domain impedance model [29] are two common methods. Compared with the state-space model, the impedance model is easier for modular modeling and analysis [30], and it has obvious advantages for analyzing the "black-box" system [31]. Hence, the impedance model has attracted a lot of research attention. Initially, the impedance analysis method was used for dc systems [32]. In the recent 20 years, the impedance analysis method has been gradually applied to ac systems. In 2011, an impedance stability criterion for inverters was proposed in [32], which reveals the equivalent relationship between the impedance stability criterion and the Nyquist stability criterion. Then, real-value d-q impedance models and complex-value sequence impedance models were investigated [33–35], which showed impedance characteristics in different reference frames. Besides, single-input single-output (SISO) stability analyzing approaches for the multiple-input multiple-output (MIMO) system were proposed in [36], which makes the Bode diagram method available for stability analysis.

Moreover, to analyze the instability mechanism of GFL converter systems, some researchers neglect outer power control loops and just consider inner current control loops [37], while other researchers just study outer power control loops [38]. Nevertheless, to obtain more precise analysis data, all the control loops need to be included. In [39], the bandwidth interactions of all the control loops are analyzed thoroughly, but just two factors are studied each time. Hence, the relationship among bandwidths of the four control loops is still unclear. In [40], the impedance characteristics of the four elements in the 2×2 matrix are presented in Bode diagrams, which show that the q–q negative resistance is the potential reason for instability.

Furthermore, in order to mitigate the aforementioned instability problems, some stability-enhanced GFL control methods have been proposed. For example, a simple stability-enhanced method by reducing the bandwidth of the PLL was proposed in [40], which can weaken the negative resistance of GFL converters. However, the drawback of this method is that the dynamic
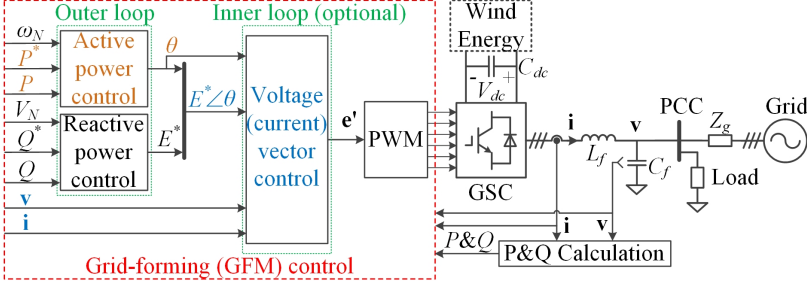
Fig. 1.8: General control scheme of a grid-forming converter.

performance of PLL is deteriorated. Besides, an H-infinity tuning method was proposed in [41], which can optimize the control parameters to enhance the stability. However, the internal control law of this method is too complicated, which makes it hard to be applied in practice. In addition, an improved control method with a symmetrical PLL was proposed in [42]. However, the constant voltage amplitude reference in the symmetrical PLL might cause control errors. Overall, existing improved GFL control methods still have some limitations, which need further study to develop an improved method with better performance.

1.1.4 State-of-the-Art of Grid-Forming Inverter

Since the converters with GFL control lack the voltage source characteristics, making it difficult for island operation, an alternative control scheme called "grid-forming" (GFM) control have attracted more attention in recent years. The general GFM control scheme on the GSC of Type-4 wind generators is presented in Fig. 1.8. With the GFM control scheme, the converter output voltage phase and amplitude are controlled respectively. Thus, similar to SGs, the converter voltage and the grid voltage can be synchronized by using the power synchronization control [43]. In Fig. 1.8, the reactive and active power controllers at the outer loop can be realized by different methods, such as the virtual synchronous generator (VSG), droop, and proportional integral (PI) control. Besides, the inner control loop is optional, which means that the converter can still work without the inner control loop. However, with the inner control loop, there are some extra benefits, such as more flexible virtual impedance implementation, accurate current control, etc. Currently, all kinds of GFM control schemes have been proposed in literature [43–50]. Among them, droop or VSG-based dual-loop vector control approach seems more attractive [51–53], where a virtual admittance or impedance is often utilized to enhance the small-signal stability.

Although the above mentioned GFM control methods work well in nor-

Table 1.4: Disadvantages and advantages of existing overcurrent protection approaches for grid forming converters [J3].

Methods	No need of grid fault detection	Smooth transient transition	Robust to SCR variation	Effective in grid voltage sag case	Effective in grid frequency drop case
Switching control modes [55]	✗	✗	✓	✓	✓
Adding virtual impedance [57]	✓	✗	✗	✓	✓
Tuning power reference [58]	✗	✓	✓	✓	✗
Voltage-based feedforward [59]	✓	✓	✓	✓	✗
Power-based feedforward [60]	✓	✓	✓	✗	✓

mal grid cases, they may have troubles in abnormal grid cases. For example, because power converters can just undertake a few percentage of overcurrent (e.g., 20%) in steady state, the converters suffer from the risk of overcurrent in the case of overload or grid fault, which might injure converters. To protect power converters against some extreme situations, such as line-tripping, short circuit fault, heavy load connection and disconnection, extra overcurrent protection is essential [54].

To address the overcurrent problem of GFM converters, several possible overcurrent protection solutions have been proposed in [55–60], which are compared in Table 1.4. A first approach is switching control modes from the GFM mode to the GFL mode during grid fault event [55]. Nevertheless, the grid fault detection is essential for this approach. It raises the control complexity. Moreover, during the fault recovery period, the integrator wind-up problem might deteriorate transient performance [56]. A second approach is introducing a virtual impedance between the grid and the converter. Thus, the output current can be restricted [57]. Nevertheless, the effect of this approach is sensitive to the transmission impedance of the grid. Moreover, the steady-state current is hard to be restricted at a predesigned value (e.g., 1 p.u.) during the grid fault period [58]. A third approach is tuning the power reference based on the grid voltage in the fault period [58]. This approach might be valid in grid voltage sag cases. Nevertheless, it does not work in grid frequency drop cases. A fourth approach is adding a frequency feedforward based on the voltage, which introduces a feedforward term from the q-axis voltage to the active power droop controller [59]. Nevertheless, this approach is just valid for the case of grid voltage sag, but not valid for the case of grid frequency drop. Another approach is adding a frequency feedforward according to the active power, which builds a feedforward term to the active power droop controller according to the power feedback [60]. However, this approach is just valid for the case of grid frequency drop, while it is not valid for the grid voltage sag scenario. Overall, existing overcurrent protection methods of GFM converters still have some limitations, which need further exploration to develop an improved method with better stability and transient performance.

1.2 Research Objectives and Limitations

To raise the performance of existing wind power generators, upgrading the hardware is a possible solution, but the cost may be increased a lot. However, the control algorithm inside the controllers can be upgraded without increasing too much cost. Hence, from a pure control algorithm perspective, there are two possible ways to go to raise the performance of grid-connected converters/wind generators. One way is to develop an improved GFL control scheme based on the original GFL control scheme. The other way is utilizing the GFM control scheme to replace the GFL control scheme. However, there are some challenges in both two ways as discussed previously.

1.2.1 Research Questions

In order to make wind generation systems connected to weak grids still meet voltage and frequency stability requirements in Grid Codes, this Ph.D. project aims to invent improved control solutions to enhance stability of wind generation systems. The major research questions are listed as follows:

How do WT generators connected to weak grids still meet voltage and frequency stability requirements specified in the Grid Codes?

- How to build small-signal models of GFL/GFM inverters, Type-4 and Type-3 WT generators to analyze their stability?

- How do GFL inverters operate stably at the rated power under weak grid conditions with low SCRs?

- How do GFM inverters with current limitation operate stably under large grid voltage and frequency disturbances?

- What is the potential control solution for Type-4 and Type-3 WT generators to operate stably in weak grids?

1.2.2 Research Objectives

To answer the aforementioned questions, the following research objectives of this thesis are defined as follows:

- **Analyzing the active power transfer ability of grid-connected converter systems:** The active power transfer ability of the grid-connected converter system is very important to be analyzed in order to find its stability limits. So, the maximum active power transfer ability of the grid-connected converter system with different SCRs and ratios of the grid resistance and inductance needs to be studied.

- **Developing an improved GFL control strategy to extend the small-signal stability range of GFL converters:** The instability mechanism of the typical GFL converter needs to be revealed clearly. Then, an improved GFL control approach needs to be developed.

- **Small-signal modeling and stability analysis for GFM converters:** The small-signal model of GFM converters needs to be built to study its small-signal stability. Then, the control parameters can be designed properly according to the necessary stability margin.

- **Developing an effective overcurrent protection method for GFM converters during large disturbances:** The problem of the typical current reference limiting approach for GFM converters needs to be analyzed. Then, an effective overcurrent protection method needs to be developed to protect and stabilize GFM converters during large grid disturbances.

- **Modeling and impedance characteristic analysis for grid-connected PMSG and DFIG systems:** To study the small-signal stability of PMSG and DFIG systems, small-signal impedance models of PMSG and DFIG systems need to be built. Besides, the terminal impedance characteristics of PMSG and DFIG systems with GFL and GFM control methods should be compared.

- **Investigating the performance of paralleled wind generators at a larger scale:** The performance of paralleled connected wind generators with GFL and GFM control schemes in a wind farm needs to be analyzed and compared. Besides, a larger-scale high-power wind generation system with GFL and GFM control schemes is worth being investigated.

1.2.3 Research Limitations

Considering that the actual wind power generation systems are very large and complex, some assumptions and simplifications are necessary for this study. So, several limitations of this thesis are summarized, as listed below:

- When studying the PMSG and DFIG-based WT generators, the rotor speed of the generator is assumed to be constant, so the mechanical dynamics of the WT are ignored.

- For the power grid, only the symmetrical three-phase grid case is considered, while the asymmetrical cases (e.g., single-phase grid fault) have not been studied. Besides, it is assumed that the grid voltage only includes sinusoidal voltage at the fundamental frequency, while the harmonics in the grid are not included.

- For the grid impedance, only the inductance-dominated case is considered, while the resistance-dominated case or the capacitance compensation case has not been considered.

- Other auxiliary devices (e.g., energy storage systems, reactive power compensators, etc) in the power system have not been considered.

- The experiments in this thesis are only carried out in a laboratory environment, where the power and voltage levels are not as high as that in the real power transmission system.

1.3 Thesis Outline

The research outcomes of this Ph.D. project are documented in this thesis according to published articles. The overall thesis includes two parts: **Report** and **Selected Publications**. Fig. 1.9 shows the structure of the thesis. The selected publications for each chapter are also denoted. Notably, the articles J2, J3, J5, C4, C5, and C7 are included in the thesis for assessment, but C8 and J6 are not included since they have not been finished at the current stage.

In the report, *Chapter 1* gives an introduction about the research background, objectives, and hypothesis of the thesis. Based on the research objectives, the following five chapters investigate stability-enhanced control solutions for GFL converters, GFM converters, PMSGs, DFIGs, and larger-scale wind generation systems, respectively.

Chapter 2 focuses on small-signal voltage stability issues of GFL converters connected to weak grids with low SCRs. Firstly, the instability mechanism of the conventional GFL converter is revealed. Then, a new double-PLL-based impedance reshaping control approach is put forward to extend the small-signal stability range. Besides, a standard quantitative stability evaluation method for GFL converters is also introduced.

Chapter 3 aims to study synchronization stability issues of GFM converters with overcurrent protection methods during large disturbances. Firstly, the problem of the typical current reference limiting approach on GFM converters is reviewed. Then, a new power-angle-based overcurrent protection approach is proposed to make a stable equilibrium point existed after a large grid disturbance.

Chapter 4 targets the control and impedance modeling of grid-connected PMSGs. Initially, the dc voltage control schemes performed by the MSC and GSC are compared. Then, impedance characteristics of GFL-PMSGs with the machine-side dc voltage control and with an ideal dc voltage source are compared. Afterwards, impedance characteristics of GFM-PMSGs with the machine-side dc voltage control are investigated.
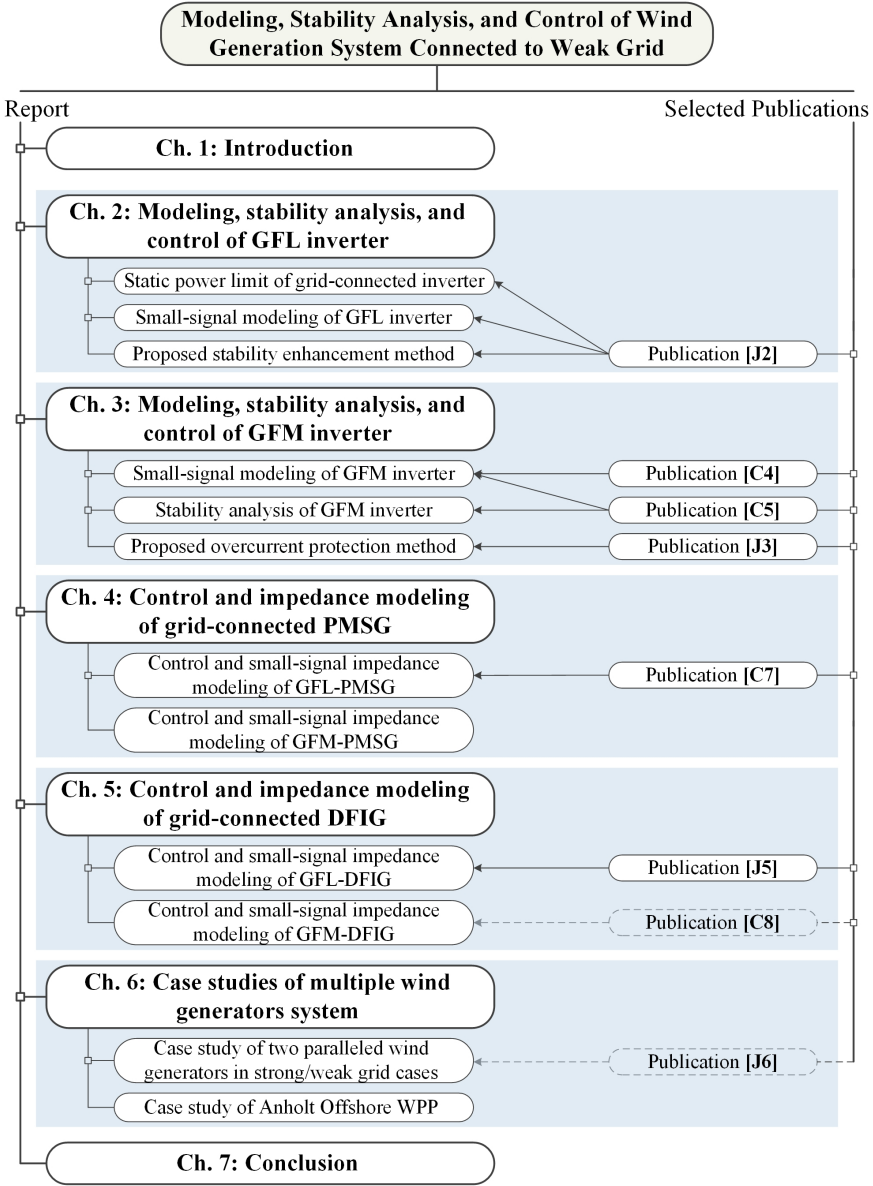
Fig. 1.9: Overall structure and selected publications of the Ph.D. thesis.

Chapter 5 deals with the control and impedance modeling of grid-connected DFIGs. Initially, a two-port-network-based decoupled impedance modeling method for the DFIG system is introduced. Then, impedance characteristics of GFL-DFIGs including dc-link voltage dynamics are analyzed. Afterwards, a virtual-admittance-based GFM control scheme is used on the RSC

and impedance characteristics of GFM-DFIGs are investigated.

Chapter 6 studies paralleled wind generators at a larger scale. At first, two paralleled WT generators with the proposed GFL/GFM control solutions in strong and weak grid cases are analyzed. Then, a more realistic case of Anholt Offshore Wind Power Plant with GFL/GFM wind generators is studied to evaluate the effectiveness of the proposed control solutions.

Finally, *Chapter 7* sums up the contributions of the thesis. Furthermore, some interesting and significant research points that have not been covered in this thesis are pointed out, which can be studied further in the future.

1.4 List of Publications

The outcomes of this project are published in the following publications, some of which are selected in the thesis for assessment.

Journal Papers

J1. **L. Huang**, C. Wu, D. Zhou, and F. Blaabjerg, "Impact of grid strength and impedance characteristics on the maximum power transfer capability of grid-connected inverters," *Appl. Sci.*, vol. 11, no.9, pp. 1-15, May 2021.

J2. **L. Huang**, C. Wu, D. Zhou, and F. Blaabjerg, "A double-PLLs-based impedance reshaping method for extending stability range of grid-following inverter under weak grid," *IEEE Trans. Power Electron.*, vol. 37, no. 4, pp. 4091-4104, Apr. 2022. (Selected in the thesis for assessment)

J3. **L. Huang**, C. Wu, D. Zhou, and F. Blaabjerg, "A power-angle-based adaptive overcurrent protection scheme for grid-forming inverter under large grid disturbances," *IEEE Trans. Ind. Electron.*, vol. 70, no. 6, pp. 5927-5936, Jun. 2023. (Selected in the thesis for assessment)

J4. **L. Huang**, C. Wu, D. Zhou, L. Chen, D. Pagnani, and F. Blaabjerg, "Challenges and potential solutions of grid-forming converters applied to wind power generation system – An overview," *Front. Energy Res.*, vol. 11, pp. 1-14, Jan. 2023.

J5. **L. Huang**, C. Wu, D. Zhou, and F. Blaabjerg, "Two-port-network-based decoupled impedance modeling method of DFIG system and dc-link coupling analysis," *Int. J. Electr. Power Energy Syst.*, Status: under review. (Selected in the thesis for assessment)

J6. **L. Huang**, C. Wu, D. Zhou, and F. Blaabjerg, "Performance evaluation of the power system with mixed grid-following and grid-forming converters," Status: to be submitted to IEEE Trans. Smart Grid.

Conference Papers

C1. **L. Huang**, C. Wu, D. Zhou, and F. Blaabjerg, "Grid impedance impact on the maximum power transfer capability of grid-connected inverter," in *Proc. IEEE 12th Energy Conv. Congr. Exp. - Asia (ECCE-Asia)*, Singapore, May 2021, pp. 1487–1490.

C2. **L. Huang**, C. Wu, D. Zhou, and F. Blaabjerg, "Comparison of three small-signal stability analysis methods for grid-following inverter," in *Proc. Int. Conf. Optim. Electr. Electron. Equip. (OPTIM)*, Brasov, Romania, Sep. 2021, pp. 34–41.

C3. **L. Huang**, C. Wu, D. Zhou, and F. Blaabjerg, "A simple impedance reshaping method for stability enhancement of grid-following inverter under weak grid," in *Proc. IEEE 12th Int. Symp. Power Electron. Distr. Gen. Syst. (PEDG)*, Chicago, IL, USA, Jun. 2021, pp. 1–6.

C4. **L. Huang**, C. Wu, D. Zhou, and F. Blaabjerg, "A simplified SISO small-signal model for analyzing instability mechanism of grid-forming inverter under stronger grid," in *Proc. IEEE 22nd Worksh. Contr. Model. Power Electron. (COMPEL)*, Cartagena, Colombia, Nov. 2021, pp. 1–6. (Selected in the thesis for assessment)

C5. **L. Huang**, C. Wu, D. Zhou, and F. Blaabjerg, "Impact of virtual admittance on small-signal stability of grid-forming inverters," in *Proc. 6th IEEE Worksh. Electron. Grid (eGRID)*, New Orleans, LA, USA, Nov. 2021, pp. 1–8. (Selected in the thesis for assessment)

C6. **L. Huang**, C. Wu, D. Zhou, and F. Blaabjerg, "A power angle limiting method for improving stability of grid-forming inverter under overcurrent condition," in *Proc. 2022 IEEE Energy Conv. Congr. Exp. (ECCE)*, Detroit, MI, USA, Oct. 2022, pp. 1–6.

C7. **L. Huang**, C. Wu, D. Zhou, and F. Blaabjerg, "Comparison of DC-link voltage control schemes on grid-side and machine-side for Type-4 wind generation system under weak grid," in *Proc. 47th Ann. Conf. IEEE Ind. Electron. Soc. (IECON)*, Toronto, ON, Canada, Oct. 2021, pp. 1–6. (Selected in the thesis for assessment)

C8. **L. Huang**, C. Wu, D. Zhou, and F. Blaabjerg, "A decomposed two-port network impedance modeling method of Type-3 wind generation system with grid-forming control," Status: to be submitted to IEEE ECCE-2023.
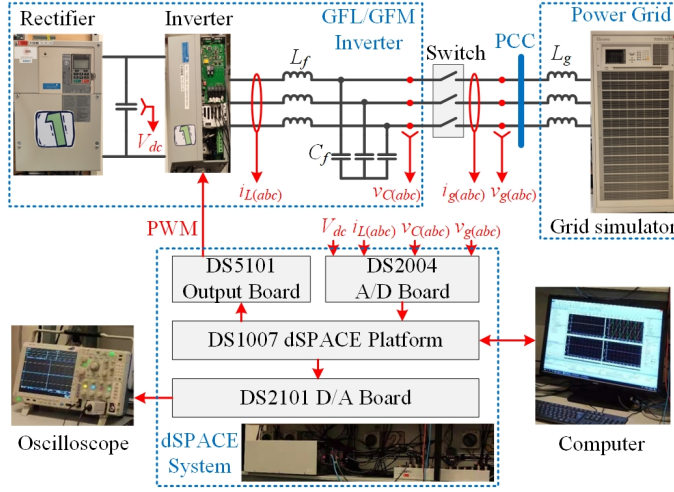
Fig. 1.10: Experimental setup utilized in this thesis.

Table 1.5: Main parameters of experimental setup.

Parameters	Values
Grid phase voltage (peak value), V_g	50 V (1 p.u.)
Grid frequency, f_g	50 Hz
Output dc voltage of rectifier, V_{dc}	600 V
Rated apparent power of inverter, S_N	800 VA (1 p.u.)
Rated active power of inverter, P_N	800 W (1 p.u.)
Rated phase voltage of inverter (peak value), V_N	50 V (1 p.u.)
Rated/maximum output current of inverter, I_{max}	10.6 A (1 p.u.)
Swiching frequency of inverter, f_{sw}	10 kHz
Sampling frequency, f_s	10 kHz

1.5 Experimental Setup Utilized in This Thesis

The experimental results shown in this thesis are acquired by using the setup presented in Fig. 1.10. The overall system can be separated into three parts: 1) The grid-side subsystem (including a grid simulator and grid inductors); 2) The converter-side subsystem (including a back-to-back converter and L-C filters); 3) The control system (including a dSPACE system with A/D and D/A boards). Specifically, in the grid-side subsystem, a grid simulator (Chroma 61845) and larger/smaller inductors L_g are used to build a weak/strong grid condition. In the converter-side subsystem, a rectifier (Yaskawa D1000) is responsible to provide a constant dc voltage, while an inverter (Danfoss

FC103P11KT11) with the L-C filters works as a GFL or GFM inverter to inject power into the grid. Besides, dSPACE system (i.e., DS1007 dSPACE platform, DS2101 D/A board, DS2004 A/D board, and DS5101 output board) is used to implement different control algorithms. Moreover, the control command for the dSPACE system is generated by the computer and the output waveforms are recorded by an oscilloscope. The detailed parameters of each experimental case will be introduced in the corresponding chapters.

Chapter 2

Modeling, Stability Analysis, and Control of GFL Inverter

Considering that the GFL inverter scheme is a mainstream scheme in existing wind power generation systems, this chapter will provide a detailed analysis for GFL inverters, from small-signal modeling, stability analysis, to finding an improved control solution. With the proposed solution, voltage stability issues of GFL inverters in weak grid cases can be addressed. Finally, simulation and experimental results will be given at the end of the chapter.

2.1 Static Power Limit of Grid-Connected Inverter

As the penetration of wind power rises, the power grid will become weaker. For the weak grid, the active power transfer capability of the inverter system is limited. To study the power limitation problems, two aspects need to be considered. Namely, when only considering steady-state algebraic equations of the system, the power transfer capability is restricted by the "static power limit" [61], because there will be no solution to the algebraic equations if the power is beyond the "static power limit". Aside from this, when considering dynamic differential equations of the system, the small-signal model and the corresponding small-signal stability boundary can be obtained. Thus, the power transfer capability is also limited by the stability boundary [J2], because the system will be unstable if the power is beyond the stability boundary. Considering that the static power limit is an important indicator of the system, it is discussed first in this section.

The configuration of typical wind power generation systems with full-power converters is presented in Fig. 2.1, where all the generators are connected at the point of common coupling (PCC). Generally, the ac/dc con-
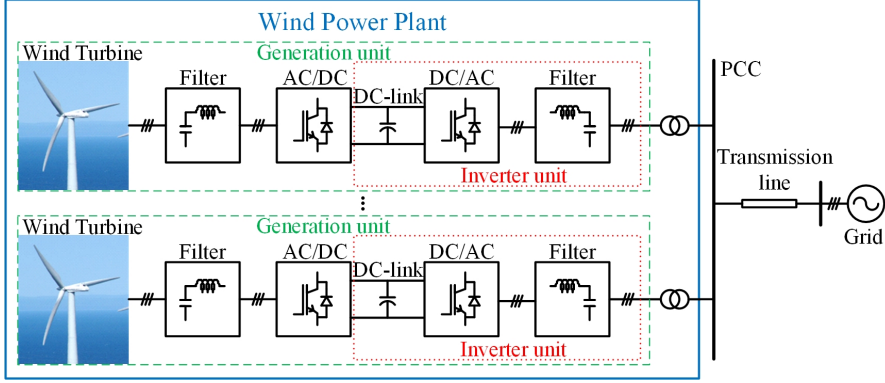
Fig. 2.1: Typical configuration of a grid-connected wind power plant. Source: [J1].
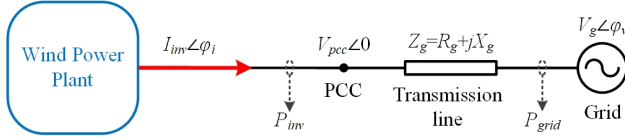
Fig. 2.2: Equivalent circuit of the grid-connected wind power plant. Source: [J1].

verter works with the MPPT control, while the dc/ac converter is used for grid connection. To simplify the analysis, the equivalent circuit of wind generation systems is presented in Fig. 2.2, where $V_g\angle\varphi_v$ is the vector of the grid voltage and $I_{inv}\angle\varphi_i$ is the vector of the total inverter current. Assuming that the PCC voltage vector is aligned to d-axis in the d-q frame, the PCC voltage can be represented by $V_{pcc}\angle 0$.

To analyze the grid strength, the definition of the SCR is provided as:

$$SCR = \frac{S_{SC}}{S_N} = \frac{V_g^2 / |Z_g|}{I_{inv(rated)} \cdot V_{pcc(rated)}} \tag{2.1}$$

where S_N is the apparent power of the wind power plant, S_{SC} is the short-circuit apparent power at the PCC, $V_{pcc(rated)}$ is the rated PCC voltage, and $I_{inv(rated)}$ is the rated output current of the wind power plant.

Assuming that $V_{pcc(rated)}$ is equal to the grid voltage V_g, and $I_{inv(rated)}$ is equal to the maximum current $I_{inv(max)}$, the grid impedance can be expressed by the SCR according to (2.1), which is expressed as:

$$|Z_g| = \sqrt{X_g^2 + R_g^2} = \frac{V_g}{SCR \cdot I_{inv(max)}} \tag{2.2}$$

Besides, according to Fig. 2.2, the expression of the inverter current in the wind power plant and the grid voltage can be deduced as:

$$V_{pcc}\angle 0 = V_g\angle\varphi_v + (R_g + jX_g) \cdot I_{inv}\angle\varphi_i \tag{2.3}$$
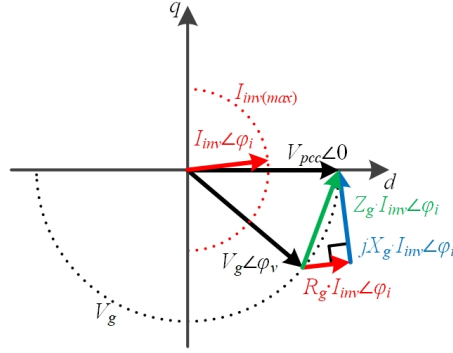
Fig. 2.3: Voltage vector diagram of grid-connected inverter system shown in Fig. 2.2 when the current limitation is considered. Source: [J1].

Moreover, the vector $I_{inv}\angle\varphi_i$ in (2.3) can be represented by the d-component "$i_d = I_{inv} \cdot \cos(\varphi_i)$" and the q-component "$i_q = I_{inv} \cdot \sin(\varphi_i)$". Take "$V_{pcc} = V_g$", then (2.3) can be deduced as:

$$(X_g^2 + R_g^2) \cdot (i_d^2 + i_q^2) + 2V_g(X_g i_q - R_g i_d) = 0 \tag{2.4}$$

2.1.1 Case 1: with Current Limitation

In practice, the maximum output current of inverters should be limited within the rated range. Thus, considering the output current limitation of the inverter, the vector diagram of the system is illustrated in Fig. 2.3, where the red and black dotted curves are the possible trajectories of the vectors $I_{inv}\angle\varphi_i$ and $V_g\angle\varphi_v$, respectively. When the inverter current is equal to $I_{inv(max)}$, the d-component current component can be presented as:

$$i_d = \sqrt{I_{inv(max)}^2 - i_q^2} \tag{2.5}$$

By substituting (2.5) into (2.4), a standardized quadratic equation of i_q can be deduced as:

$$\frac{1}{R_g^2 + X_g^2} \cdot i_q^2 + \frac{X_g I_{inv(max)}^2}{(R_g^2 + X_g^2)V_g} \cdot i_q + \left[\frac{I_{inv(max)}^4}{4V_g^2} - \frac{R_g^2 I_{inv(max)}^2}{(R_g^2 + X_g^2)^2}\right] = 0 \tag{2.6}$$

Then, i_q can be obtained by solving (2.6).

$$i_q = R_g I_{inv(max)} \cdot \sqrt{\frac{1}{R_g^2 + X_g^2} - \frac{I_{inv(max)}^2}{4V_g^2}} - \frac{X_g I_{inv(max)}^2}{2V_g} \tag{2.7}$$

When substituting (2.2) and (2.7) into (2.5), the output power P in per unit (p.u.) value is deduced as (2.8).

23
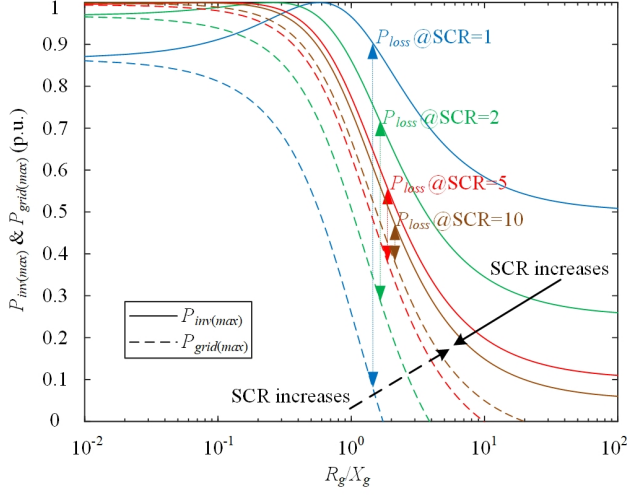
Fig. 2.4: Maximum output power of grid-connected inverter when the current limitation is considered ($P_{inv(max)}$: inverter output power; $P_{grid(max)}$: received power of the grid). Source: [J1].

$$P_{inv(pu)} = \frac{P_{inv}}{S_N} = \frac{V_g \cdot i_d}{V_g \cdot I_{inv(max)}} = \frac{\sqrt{SCR^2 - \frac{1}{4}} + \frac{R_g}{2X_g}}{SCR \cdot \sqrt{1 + \frac{R_g^2}{X_g^2}}} \qquad (2.8)$$

Moreover, according to (2.1) and (2.2), the lost power on the transmission line can be calculated as:

$$P_{loss(pu)} = \frac{P_{loss}}{S_N} = \frac{I_{inv(max)}^2 \cdot R_g}{V_g \cdot I_{inv(max)}} = \frac{\frac{R_g}{X_g}}{SCR \cdot \sqrt{1 + \frac{R_g^2}{X_g^2}}} \qquad (2.9)$$

Thus, based on (2.8) and (2.9), the received power of the grid is given as:

$$P_{grid(pu)} = P_{inv(pu)} - P_{loss(pu)} = \frac{\sqrt{SCR^2 - \frac{1}{4}} - \frac{R_g}{2X_g}}{SCR \cdot \sqrt{1 + \frac{R_g^2}{X_g^2}}} \qquad (2.10)$$

Therefore, according to (2.8) and (2.10), the maximum output power of grid-connected inverter with current limitation is illustrated in Fig. 2.4. It shows that as the SCR increases or R_g/X_g decreases, the maximum transferred power to the grid $P_{grid(max)}$ will increase. Namely, a larger SCR and a smaller R_g/X_g are better for the power transmission.

Notably, the inverter output power $P_{inv(max)}$ increases as the SCR decreases in the resistive grid case ($R_g/X_g > 1$), since much reactive power need to be provided to keep the PCC voltage as same as the rated value. However, it is not economical to do so. Modifying the reference value of PCC voltage slightly higher than the rated value may be a better solution [J1].
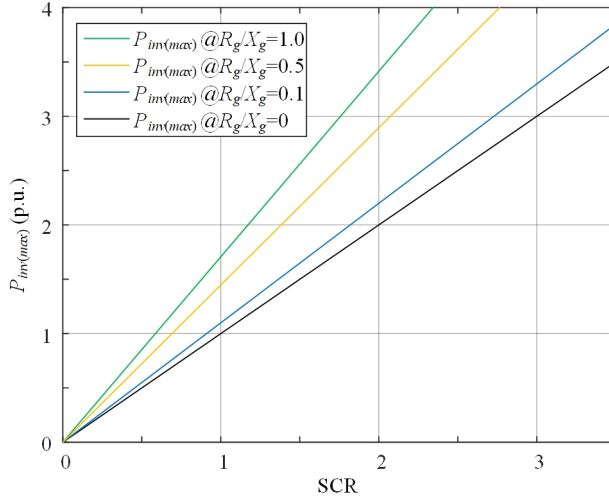
Fig. 2.5: Ideal maximum output power of grid-connected inverter when the current limitation is excluded. Source: [J1].

2.1.2 Case 2: without Current Limitation

When the current limitation of the inverter is utilized, both the output current and power of the inverter are limited, which is not convenient for analyzing the potential maximum power output capability of the inverter. Hence, an ideal case without the current limit will be discussed as follows.

Substituting (2.1) into (2.4), the relationship between i_d and i_q is given by:

$$i_{q(pu)}^2 + \frac{2 \cdot SCR}{\sqrt{(R_g/X_g)^2 + 1}} \cdot i_{q(pu)} + \left[i_{d(pu)}^2 - \frac{2 \cdot SCR \cdot (R_g/X_g)}{\sqrt{(R_g/X_g)^2 + 1}} \cdot i_{d(pu)} \right] = 0 \tag{2.11}$$

Considering (2.11) as a quadratic expression of $i_{q(pu)}$, only when (2.12) is fulfilled, (2.11) has solutions.

$$\Delta = \frac{4 \cdot SCR^2}{(R_g/X_g)^2 + 1} + \frac{8 \cdot SCR \cdot (R_g/X_g)}{\sqrt{(R_g/X_g)^2 + 1}} \cdot i_{d(pu)} - 4 \cdot i_{d(pu)}^2 \geq 0 \tag{2.12}$$

According to (2.12), the maximum value of $i_{d(pu)}$ is derived as (2.13). Moreover, since the amplitude of PCC voltage is treated to be equal to the rated value, the p.u. values of i_d and P_{inv} are the same. So, the ideal maximum output power of the inverter is able to be derived as:

$$P_{inv(pu)(max)} = i_{d(pu)(max)} = \left[\frac{(R_g/X_g)}{\sqrt{(R_g/X_g)^2 + 1}} + 1 \right] \cdot SCR \tag{2.13}$$

25
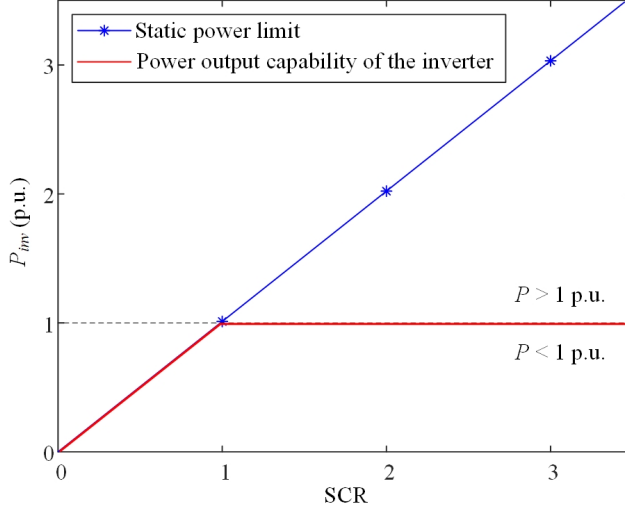
Fig. 2.6: Relationship of the static power limit and SCR with $R_g/X_g \approx 0$. Source: [J2].

Therefore, the relationship of the SCR and the ideal maximum output power $P_{inv(max)}$ with different R_g/X_g is presented in Fig. 2.5. It shows that the relationship of $P_{inv(max)}$ and the SCR is linear. For the inductive case ($R_g/X_g = 0$), SCR = 1 is a critical point since the maximum power $P_{inv(max)}$ is smaller than 1 p.u. when the SCR is smaller than 1. So, the maximum output power of grid-connected inverters is limited naturally in the case of weak grid. This maximum output power of grid-connected inverters is called "static power limit" in [61].

Based on the above analysis, the maximum power output capability of the inverter in the inductive grid case ($R_g/X_g \approx 0$) is illustrated by the red line in Fig. 2.6. Obviously, the active power output capability of inverters is restricted by the "static power limit" in weak grids with SCR ≤ 1. Nevertheless, when the dynamic power limit is considered, the power limitation problem will become worse, which will be explained in the following section.

2.2 Dynamic Power Limit of GFL Inverter

Aside from the static power limit, the dynamic power limit can also restrict the power output ability of inverters. The dynamic power limit is named from [J2], which stands for the small-signal stability boundary of the system. This section will discuss the dynamic power limit of GFL inverters.

The system and control diagram of the conventional GFL inverter system is presented in Fig. 2.7, where $V_c \angle \theta_c$ is the terminal voltage of the converter, $V_o \angle \theta_o$ is the PCC voltage, and $V_g \angle \theta_g$ is the grid voltage. Besides, L_g and
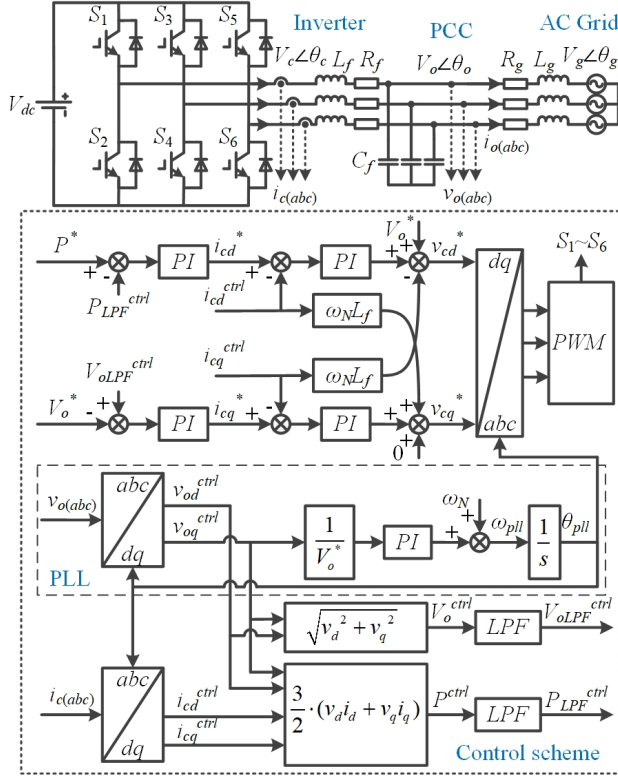
Fig. 2.7: Grid-connected inverter with conventional GFL control scheme. Source: [J2].

R_g are grid inductance and resistance. C_f and L_f are filter capacitance and inductance. To avoid the ac-side low-frequency passive resonance, the filter capacitance C_f can be designed as small as possible.

The control scheme presented in Fig. 2.7 includes an inner current control loop and an outer reactive/active power control loop. Since the PCC voltage needs support in weak grids, the ac voltage amplitude is chosen as the control target rather than the reactive power. Besides, the whole control scheme is carried out in the d-q frame. And it is synchronized with the grid voltage at the PCC.

2.2.1 Small-Signal Modeling of GFL Inverter

To study the stability of the inverter system, the linearized small-signal model is a useful tool. Specifically, the system is able to be linearized at an operating point. Thus, it is easier to use mature linear methods to analyze the stability. Notably, in the thesis, the subscript '$_0$' represents a steady-state operation point. Besides, 'Δ' represents a small-signal perturbation.

Table 2.1: Comparison of state-space model and impedance model. Source: [C2]

Methods	State-space model	Impedance model
Universality	High	Medium [32]
Availability for black-box system	No	Yes [62]
Visualization of internal structure	Medium	High [30]
Scalability for larger scale system	Medium	High [63]

Fig. 2.8: Small-signal d-q impedance model and equivalent circuit of GFL inverter. Source: [J2].

The state-space model in time-domain and impedance model in frequency-domain are two widely used small-signal models. In [C2], two models' similarities and differences are compared. It is found that these two models can predict the same stability boundary of the GFL inverter. However, they have different advantages. As shown in Table 2.1, the impedance model has the advantages of high visualization, high scalability, and availability for the "black-box" system without internal information. Therefore, the impedance model will be used more in the thesis to investigate the small-signal stability.

Fig. 2.9: Flowchart for seeking the stability boundary of the inverter system. Source: [J2].

The small-signal impedance model of the GFL inverter system is presented in Fig. 2.8. The superscript 'ctrl' represents control d-q frame. The symbol **B** represents a 2×2 matrix (See [J2] for detailed expressions). As shown in Fig. 2.8, the system is able to be separated into two subsystems. Namely, the grid-side subsystem is represented by a voltage source connecting to an impedance $\mathbf{Z_g}(s)$, and the converter-side subsystem is modeled by a current source paralleled with an admittance $\mathbf{Y}(s)$. Thus, the converter output current can be derived as:

$$\Delta \mathbf{i_{cdq}} = \left[\Delta \mathbf{i_{sdq}} - \mathbf{Y}(s) \cdot \Delta \mathbf{v_{gdq}} \right] \cdot \frac{1}{\mathbf{I} + \mathbf{Y}(s) \cdot \mathbf{Z_g}(s)} \qquad (2.14)$$

Based on the internal structure of the impedance model in Fig. 2.8, the equivalent impedance and admittance can be deduced as:

$$\mathbf{Z_g}(s) = (\mathbf{B_{Cf}} + \mathbf{B_{Lg}}^{-1})^{-1} \approx \mathbf{B_{Lg}} \qquad (2.15)$$

$$
\begin{aligned}
\mathbf{Y}(s) = &[\mathbf{B_{PI\text{-}I}} - \mathbf{B_{decpl}} + \mathbf{B_{Lf}} + \mathbf{B_{PI\text{-}I}}\mathbf{B_{PI\text{-}PV}}\mathbf{B_{LPF}}\mathbf{B_v}]^{-1} \\
&\cdot [\mathbf{I} - (\mathbf{B_{PI\text{-}I}} - \mathbf{B_{decpl}} + \mathbf{B_{PI\text{-}I}}\mathbf{B_{PI\text{-}PV}}\mathbf{B_{LPF}}\mathbf{B_v}) \\
&\cdot \mathbf{B_{pll\text{-}Ic}} - \mathbf{B_{pll\text{-}Vc}} + \mathbf{B_{PI\text{-}I}}\mathbf{B_{PI\text{-}PV}}\mathbf{B_{LPF}}\mathbf{B_i} \\
&\cdot (\mathbf{I} - \mathbf{B_{pll\text{-}Vo}})]
\end{aligned}
\qquad (2.16)
$$
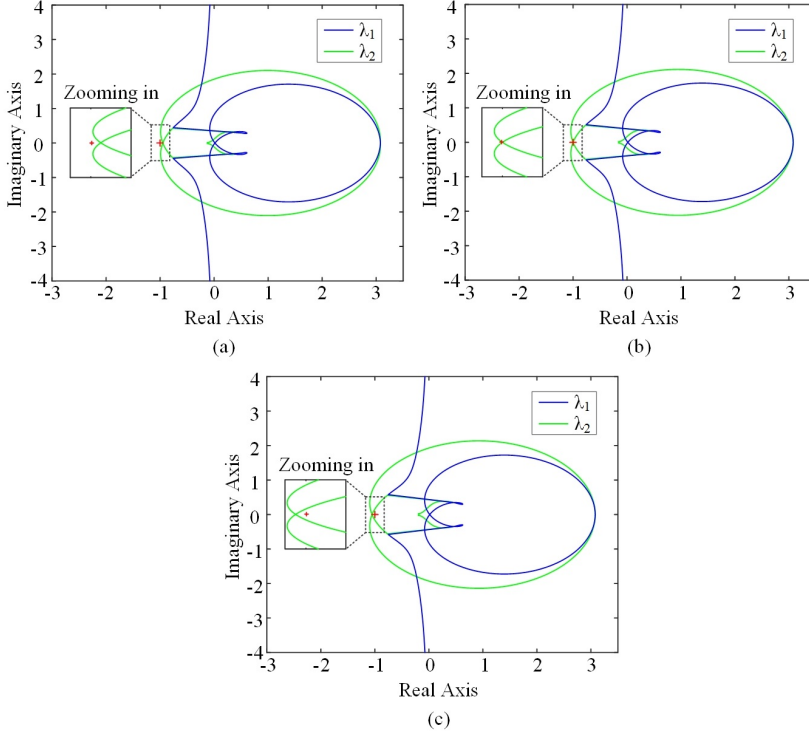
Fig. 2.10: Generalized Nyquist diagrams of $\mathbf{Y}(s) \cdot \mathbf{Z_g}(s)$ in the weak grid case with SCR = 1. (a) $P = 0.5$ p.u.; (b) $P = 0.55$ p.u.; (c) $P = 0.6$ p.u. Source: [J2].

According to generalized Nyquist (GN) stability criterion, $\mathbf{Y}(s) \cdot \mathbf{Z_g}(s)$ in (2.14) can be used for stability analysis [39]. The flowchart to find the stability boundary is presented in Fig. 2.9. Firstly, given all control parameters and the steady-state operating point, $\mathbf{Y}(s) \cdot \mathbf{Z_g}(s)$ can be obtained based on (2.15) and (2.16). Then, the GN diagrams of $\mathbf{Y}(s) \cdot \mathbf{Z_g}(s)$ can be plotted for analyzing the stability of the system. Following the flowchart in Fig. 2.9, the stability boundary of the grid-connected system is able to be sought.

For example, when the SCR is 1, the GN diagrams of $\mathbf{Y}(s) \cdot \mathbf{Z_g}(s)$ at different steady-state working points are plotted in Fig. 2.10. As presented in Fig. 2.10(a), when P is equal to 0.5 p.u., the point (-1, j0) is not encircled by the GN curves. So, the system is stable. Differently, as presented in Fig. 2.10(c), when P is equal to 0.6 p.u., the point (-1, j0) is encircled by the GN curves. So, the system is not stable. Besides, as illustrateted in Fig. 2.10(b), when P is equal to 0.55 p.u., the point (-1, j0) is on the GN curves. Thus, the stability boundary can be sought, that is 0.55 p.u. With this method, the stability boundaries when the SCR is equal to 2 and 3 can also be found, which are 1.65 p.u. and 2.75 p.u. Then, the dynamic power limit can be plotted.
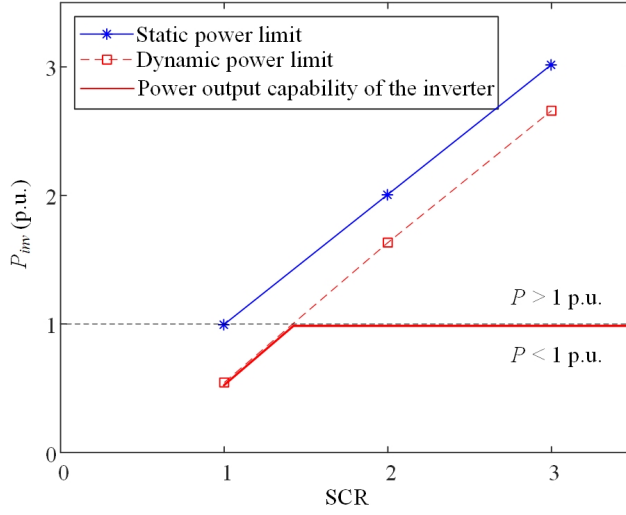
Fig. 2.11: Relationship of the dynamic power limit and SCR. Source: [J2].
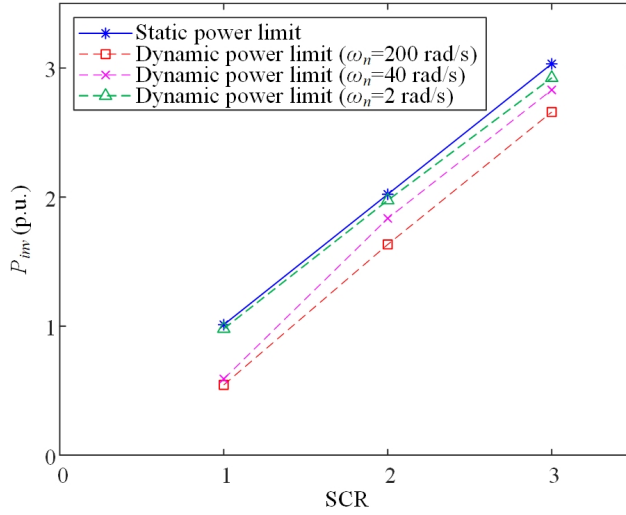
Fig. 2.12: Relationship of the dynamic power limits and SCR with dissimilar PLL bandwidths. Source: [J2].

2.2.2 Small-Signal Stability Boundary of GFL Inverter

According to stability analysis in Section 2.2.1, the relationship of dynamic power limits and the SCR is presented in Fig. 2.11, where the static power limit is also included. It shows that the static power limit is higher than all dynamic power limits. So, the power output ability of the inverter is restricted

31

by the dynamic power limit, particularly for weak grids with SCR ≤ 1.5.

Since the dynamic power limit depends on the specific control schemes and parameters, it can be improved when the control schemes and parameters are well-designed. A simple stability-enhanced method by tuning the PLL bandwidth has been introduced in [40]. The dynamic power limits with dissimilar PLL bandwidths are presented in Fig. 2.12. Notably, ω_n is the natural angular frequency of the PLL, that is proportional to the PLL bandwidth. Fig. 2.12 shows that the dynamic power limit increases as ω_n decreases. Namely, a lower bandwidth of the PLL is beneficial for enhancing the small-signal stability of GFL converters. Nevertheless, while the PLL bandwidth is designed to be very low, its dynamic performance will be worsened. So, a tradeoff between the dynamic performance and stability is necessary for this approach. To solve this issue, another method by reshaping the output impedance of converters could be a better choice [64].

2.3   Proposed Impedance Reshaping Method

For enhancing the small-signal stability of the GFL converter system while not worsening the dynamic performance, an interesting impedance reshaping method is proposed in [64]. The idea of this approach is to modify the control structure in the impedance model to reshape the output impedance characteristics. Following this idea, impedance reshaping approaches by adding impedance controllers on the q–q channel have been proposed in [65] and [66]. Nevertheless, the negative resistance on the d–q channel introduced by the PLL has not been addressed. It might also cause instability. Therefore, to extend the stability range to the greatest extent, the negative resistances on both q–q and d–q channels introduced by the PLL should be addressed. A new improved GFL control solution will be provided in this section.

To obtain more intuitive analysis results, suitable simplification is needed. Assuming that the bandwidth of the inner current control loop is high enough (i.e., $\omega_i = \infty$) and the filter resistance R_f is equal to 0, the admittance $\mathbf{Y}(s)$ in (2.16) can be approximately derived as:

$$\mathbf{Y}(s) \approx \begin{bmatrix} \frac{(1-G_p)}{sL_f+\omega_iL_f} + \frac{G_p}{R_d} & \frac{G_p+(1-G_p)\cdot G_{pll}}{-R_q} \\ \frac{\omega_v}{-sX_m} & \frac{(1-G_{pll})}{sL_f+\omega_iL_f} + \frac{G_{pll}}{-R_d} \end{bmatrix} \quad (2.17)$$

where $R_q = V_o/(-i_{cq0}) > 0$, $R_d = V_o/i_{cd0} > 0$, $X_m = V_o/I_{max} > 0$, $G_p = \omega_p/(s+\omega_p)$, and $G_{pll} = (2\xi\omega_ns+\omega_n^2)/(s^2+2\xi\omega_ns+\omega_n^2)$.

It can be seen from (2.17) that a negative resistance term $G_{pll}/(-R_d)$ on the q–q channel and a negative resistance term $[G_p + (1 - G_p) \cdot G_{pll}]/(-R_q)$ on the d–q channel exist. Therefore, how to mitigate these negative resistances will become the key research focus here.
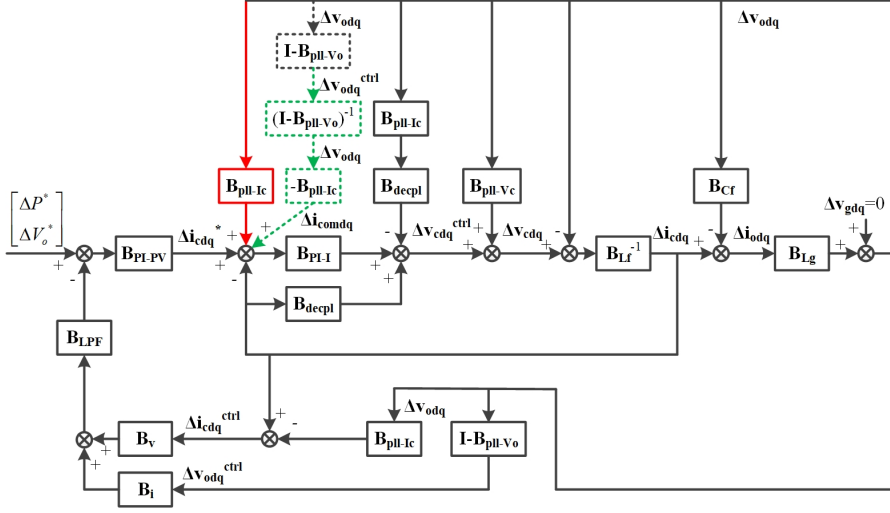
Fig. 2.13: Small-signal d-q impedance model with expected reshaped impedance. Source: [J2].

2.3.1 Initial Improved GFL Control Scheme

In fact, the negative resistances on q–q and d–q channels in (2.17) are caused by the positive feedback in the small-signal impedance model (marked in red) in Fig. 2.13 (Notably, Fig. 2.13 is completely equivalent to Fig. 2.8). To mitigate the positive feedback, an additional negative feedback can be introduced, which is marked by dotted line. Besides, to realize the expected reshaped impedance in the actual control scheme, a few practical factors need to be taken into account. Since the voltage $\Delta \mathbf{v_{odq}}^{\text{ctrl}}$ can be measured instead of $\Delta \mathbf{v_{odq}}$, the added transfer function is changed from $\Delta \mathbf{v_{odq}}^{\text{ctrl}}$ as input to $\Delta \mathbf{i_{comdq}}$ as output. It has been highlighted in green in Fig. 2.13. Thus, the expression of the compensating term $\Delta \mathbf{i_{comdq}}$ can be deduced by:

$$\begin{bmatrix} \Delta i_{\text{com}d} \\ \Delta i_{\text{com}q} \end{bmatrix} = -\mathbf{B}_{\text{pll-Ic}} \cdot (\mathbf{I} - \mathbf{B}_{\text{pll-Vo}})^{-1} \cdot \begin{bmatrix} \Delta v_{od}^{\text{ctrl}} \\ \Delta v_{oq}^{\text{ctrl}} \end{bmatrix} \tag{2.18}$$

By substituting the expressions of $\mathbf{B}_{\text{pll-Ic}}$ and $\mathbf{B}_{\text{pll-Vo}}$ (See [J2]) into (2.18), it can be derived as:

$$\begin{bmatrix} \Delta i_{\text{com}d} \\ \Delta i_{\text{com}q} \end{bmatrix} = \frac{\Delta v_{oq}^{\text{ctrl}}}{V_o} \cdot (K_{p\_pll} + \frac{K_{i\_pll}}{s}) \cdot \frac{1}{s} \cdot \begin{bmatrix} i_{cq0} \\ -i_{cd0} \end{bmatrix} \tag{2.19}$$

To implement the reshaped small-signal impedance in the actual control scheme, the reference values of the current in the control scheme presented in Fig. 2.7 can be utilized for representing steady-state currents i_{cd0} and i_{cq0} in (2.19). Thus, according to (2.19), an initial improved GFL control solution is shown in Fig. 2.14, where two current compensating terms and an integral term marked in green are added.

Fig. 2.14: Proposed initial improved GFL control solution. Source: [J2].

Fig. 2.15: Impedance characteristics of reshaped and original $Y_{dq}(s)$ and $Y_{qq}(s)$ in the case of P = 0.6 p.u. and SCR = 1 (a) $Y_{dq}(s)$; (b) $Y_{qq}(s)$. Source: [J2].

According to the proposed initial improved GFL control solution presented in Fig. 2.14, the small-signal model can be built once more. Then, the reshaped output admittance of the converter $\mathbf{Y_r}(s)$ can be deduced (See [J2]). Fig. 2.15 shows the characteristics of the orignal impedance $\mathbf{Y}(s)$ and the reshaped impedance $\mathbf{Y_r}(s)$, where a steady-state operation point with SCR = 1 and P = 0.6 p.u. are used as an example. Fig. 2.15 shows that $Y_{qq}(s)$ has been reshaped from negative resistances to positive resistances in the range from 27 Hz to 44 Hz. In addition, $Y_{dq}(s)$ has been reshaped from the negative resistances to positive resistances in the range from 16 Hz to 89 Hz. Furthermore, the amplitude of $Y_{dq}(s)$ is decreased more than 20 dB, so the couplings between the q-axis and d-axis can be mitigated too.

To observe the achievement of the proposed control solution regarding the

Fig. 2.16: Generalized Nyquist diagrams of $\mathbf{Y_r}(s) \cdot \mathbf{Z_g}(s)$ in the case of SCR = 1. (a) $P = 0.6$ p.u.; (b) $P = 0.9$ p.u. Source: [J2].
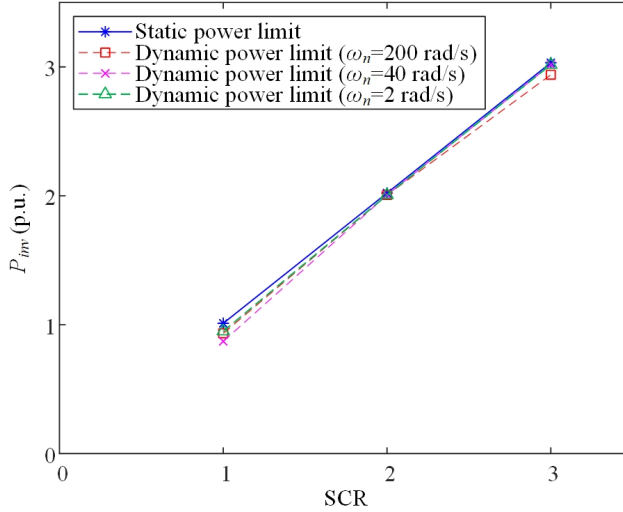
Fig. 2.17: Relationship between dynamic power limits and SCRs with dissimilar PLL bandwidths by applying the proposed initial improved solution. Source: [J2].

stability, the GN criterion is utilized once more. The GN diagrams of $\mathbf{Y_r}(s) \cdot \mathbf{Z_g}(s)$ in the case of SCR = 1 are plotted in Fig. 2.16. Comparing Fig. 2.16(a) with Fig. 2.10(c), it shows that while P is 0.6 p.u., the unstable system has been modified to be a stable system with the proposed control solution. In addition, as presented in Fig. 2.16(b), when the active power is raised to 0.9 p.u., the system is also kept stable. Therefore, the stability range can be extended by the proposed control solution.

Based on the Nyquist stability analysis by using $\mathbf{Y_r}(s) \cdot \mathbf{Z_g}(s)$, the small-signal stability bounary (dynamic power limit) of the proposed control solu-

Fig. 2.18: Proposed further improved GFL control solution. Source: [J2].

tion can be found. The relationship between the SCR and dynamic power limits with dissimilar PLL bandwidths by applying proposed initial improved solution are presented in Fig. 2.17. It indicates that the bandwidth of PLL has tiny impact on the dynamic power limit. In this case, all dy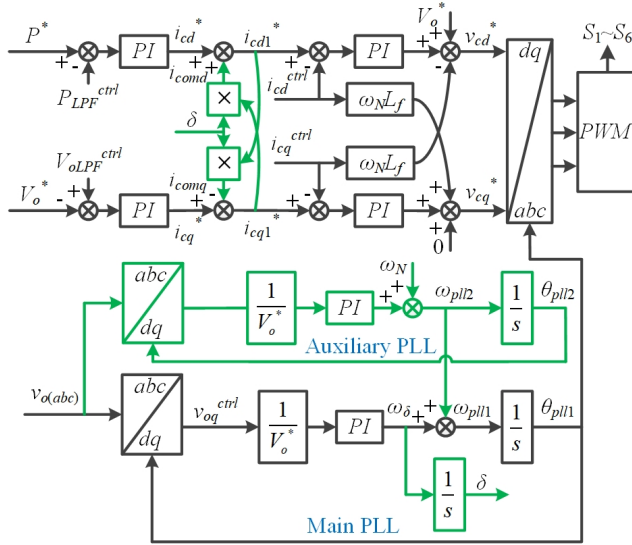namic power limits are near the static power limit. Consequently, the power output ability of GFL inverters can be improved.

2.3.2 Further Improved GFL Control Scheme

Even though the proposed initial improved control solution is able to enlarge the stability range of the grid-connected system, it just works in an ideal case where the angular frequency of the grid is invariable and equal to the nominal value ω_N. Nevertheless, such an ideal case may not be met in practice. In Fig. 2.14, when the angular frequency of the grid is not as same as ω_N, ω_{pll} is not equal to ω_N. Thus, ω_δ is not equal to zero in steady-state. While ω_δ is higher than zero, δ will continuously rise because of the integrator, and vice versa. Ultimately, the system will be out of control. To solve this issue, an additional auxiliary PLL is added to estimate the grid frequency, which can generate a frequency feedforward term. Hence, the proposed further improved solution is presented in Fig. 2.18.

Notably, the major aim to introduce another PLL is to keep the feedforward frequency same as the grid frequency in steady-state. So, ω_{pll1} is equal to ω_{pll2}, and ω_δ is equal to zero, which leads to a constant δ. Hence, the bandwidth of the auxiliary PLL needs to be designed much lower than that

Fig. 2.19: Simulation results of GFL inverters in the case of SCR = 1. (a) Using conventional GFL control scheme; (b) Using proposed improved GFL control scheme. Source: [J2].

of the main PLL (e.g., 1/10).

To demonstrate the effectiveness of the proposed solution, an 800 W GFL inverter model is built in MATLAB/Simulink (See [J2] for detailed parameters). The simulation results of conventional GFL control approach and proposed improved GFL control method are illustrated in Fig. 2.19(a) and (b). As shown in Fig. 2.19(a), with the conventional GFL control approach, the oscillation of the PCC voltage appears while the active power is near 0.6 p.u. Then, the PCC voltage is out of control. Differently, as presented in Fig. 2.19(b), the
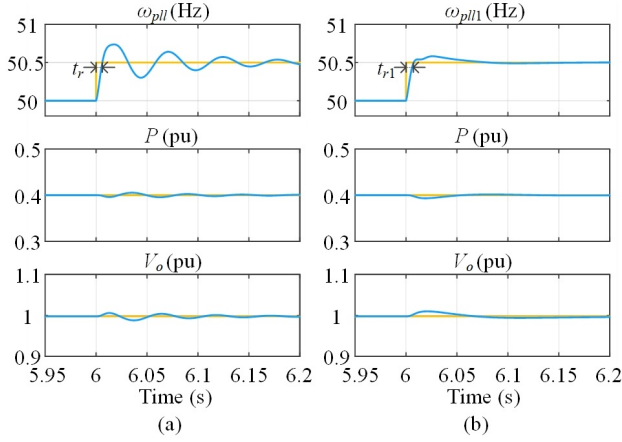
Fig. 2.20: Comparison of two GFL control schemes with ω_n = 200 rad/s in the case of grid frequency variation. (a) Conventional GFL control scheme; (b) Proposed improved GFL control solution. Source: [J2].

PCC voltage is under control by using the proposed improved GFL control scheme. Notably, the GFL inverter is also kept stable while the active power increases to 0.9 p.u. The simulation results are persistent to the theoretical analysis results presented in Fig. 2.10(c) and Fig. 2.16(b).

To show that the frequency response of the PLL is not slowed down by the proposed improved double-PLL-based control solution, simulation results of the conventional and proposed GFL control schemes are presented in Fig. 2.20 for comparison. It indicates that the rise time t_r in Fig. 2.20(a) is generally same as the rise time t_{r1} in Fig. 2.20(b) while the grid frequency is stepped to 50.5 Hz.

Moreover, the experiment is carried out to validate the effect of the proposed improved GFL control solution, where the experimental parameters are as same as that used in simulation (See [J2] for detailed parameters). As shown in Fig. 1.10 in Section 1, the Danfoss FC103P11KT11 is used to implement a grid-connected inverter, and the dSPACE1007 is used to implement the control algorithms. Besides, a grid simulator (Chroma 61845) and inductors (L_g) are used to achieve a strong/weak grid condition. The experimental outcomes of the conventional and proposed GFL control schemes are illustrated in Fig. 2.21(a) and (b).

Fig. 2.21(a) shows that when the power P is raised to 0.6 p.u., the GFL inverter system is unstable by using the conventional GFL control scheme. However, as presented in Fig. 2.21(b), the GFL inverter system is stable by using the proposed improved GFL control solution. Besides, when the power P reaches 0.9 p.u., the GFL inverter system is still stable. These experimental results match the simulation results presented in Fig. 2.19(a) and (b) well.
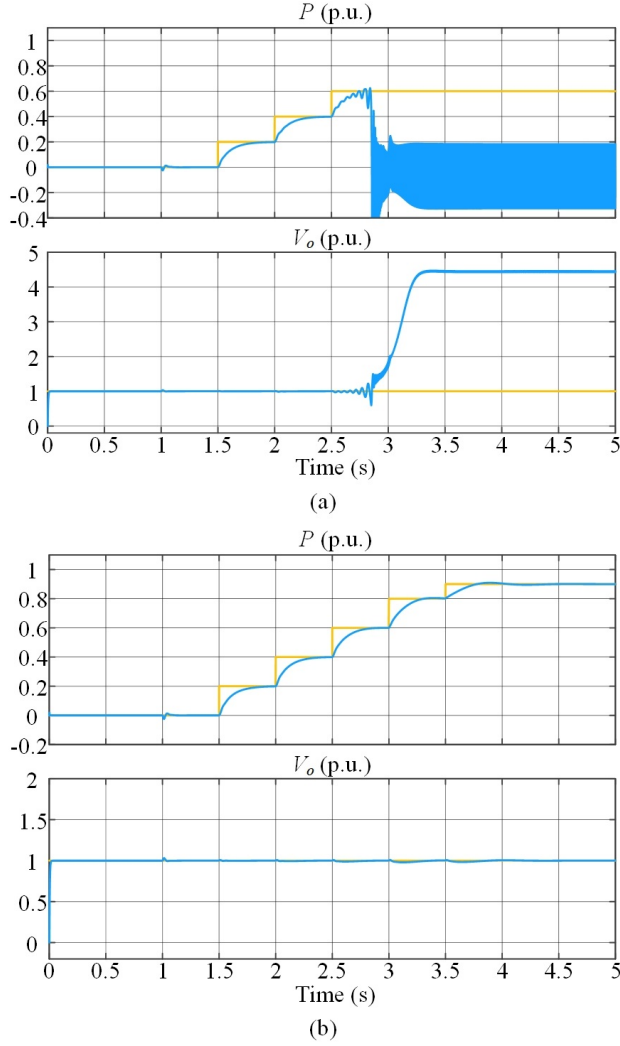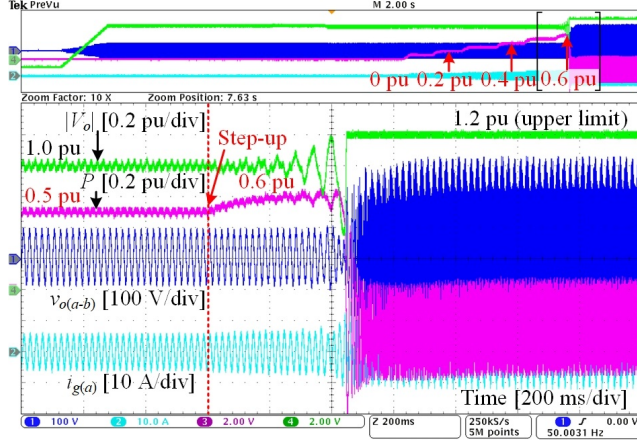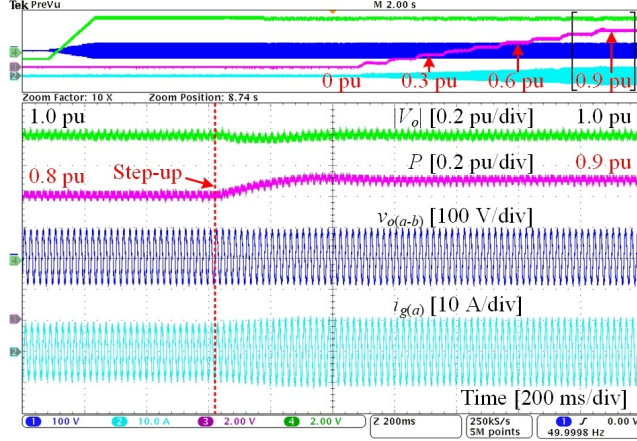
Fig. 2.21: Experimental results of GFL inverter in the case of SCR = 1. (a) Using conventional GFL control method; (b) Using proposed improved GFL control method in Fig. 2.18 (CH4: PCC voltage amplitude; CH3: active power; CH2: grid phase current; CH1: phase-to-phase voltage at the PCC). Source: [J2].

2.4 Summary

This chapter has provided a comprehensive discussion of modeling and small-signal stability analysis of GFL inverters. At first, a small-signal stability evaluation approach through comparing the static power limit and the dynamic power limit is introduced, which is beneficial for analyzing the small-signal stability quantitatively. It is found that the power output ability of conventional GFL inverters is restricted by the dynamic power limit under weak grid conditions, perticularly in the case of "SCR ≤ 1.5". To extend the dynamic

power limit, an initial impedance reshaping approach has been proposed. It can mitigate the positive feedback in the small-signal impedance model of GFL inverters. Then, a corresponding improved GFL control scheme is also proposed to implement the expected reshaped impedance in the actual control scheme. With the proposed improved GFL control scheme, the dynamic power limit of GFL inverters can be extended close to the static power limit no matter the bandwidth of the PLL is larger or smaller. Thus, the voltage instability issue of conventional GFL inverters connected to weak grids is solved. Finally, simulations and experiments have demonstrated the effectiveness of the proposed improved GFL control solution.

Chapter 3

Modeling, Stability Analysis, and Control of GFM Inverter

In the future power system, only having GFL inverters may not be enough, since GFM inverters are necessary for the island operation and the frequency support. This chapter will provide a detailed analysis for GFM inverters, from small-signal stability analysis in normal grid cases, large-signal stability analysis in abnormal grid cases, to finding an improved control solution. With the proposed solution, "rotor angle" stability issues of GFM inverters under large grid disturbances can be addressed. Eventually, simulation and experimental results will be given at the end of the chapter.

3.1 Comparative Study of GFM Inverters

Although the GFL inverter scheme is a mainstream scheme in existing wind power generation systems, it has challenges to provide frequency support and to operate in island conditions. Therefore, another type of inverter called "grid-forming (GFM)" inverter attracts more interest recently. Because GFM inverters can support the grid frequency and operate in island conditions, they are considered to be promising solutions for the future power system [67,68]. Until now, all kinds of GFM control approaches have been proposed in existing literature [69]. Considering that existing GFM control schemes have not been unified or standardized yet, the difference among different GFM control schemes will be discussed initially in this section.

Currently, alternative GFM control schemes and concepts have been presented, such as power synchronization (PS) control, virtual synchronous generator (VSG), synchronous power control, synchronverter, virtual synchronous machine (VSM), etc. They comply with the same PS control law. So, a gen-
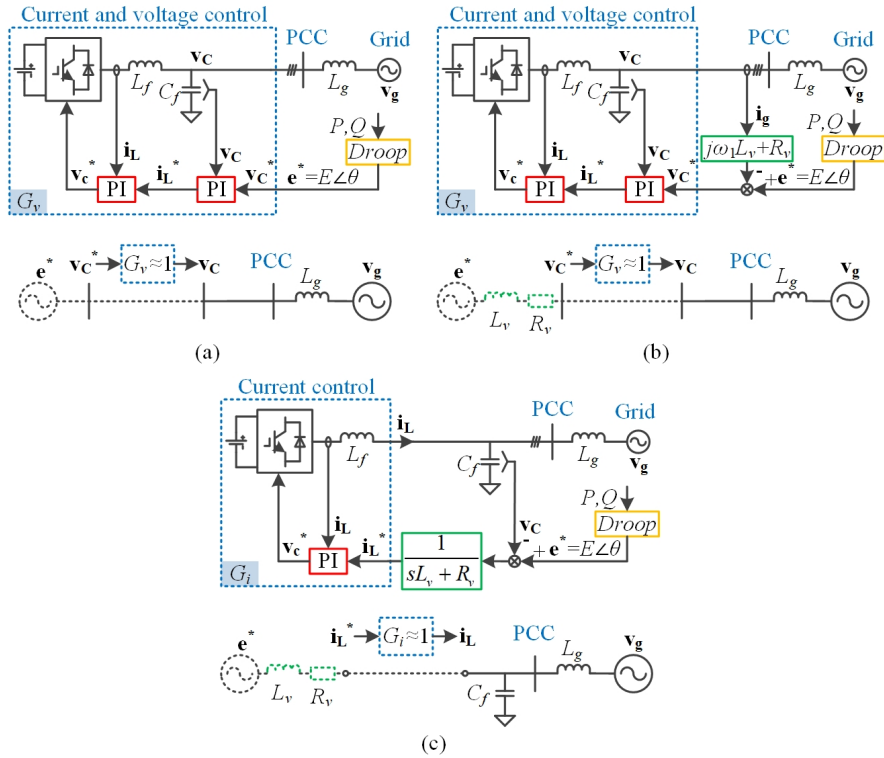
Fig. 3.1: Three typical GFM control schemes and their equivalent circuits. (a) Typical dual-inner-loop control approach; (b) Virtual impedance control approach; (c) Virtual admittance control approach. Source: [C5].

eral GFM control structure has been summarized in [43] and [J4], as shown in Fig. 1.8. According to whether including inner control loops or not, GFM control methods can be classified into two categories: single-loop control scheme and multiple-loop control scheme [70]. Relatively, the single-loop GFM control scheme without inner control loops is simpler and more robust. Nevertheless, the multiple-loop GFM control scheme with inner control loops has some extra advantages, such as more flexible virtual impedance implementation and accurate current control. Moreover, having the inner current control loop is advantageous for adding output current limits to avoid overcurrent of converters under large grid disturbances [J3]. Therefore, multiple-loop GFM control approaches will be mainly discussed in this thesis.

In terms of multiple-loop GFM control schemes, three typical schemes have been widely reported in literature, which are the typical dual-inner-loop control approach [52], [71], the virtual impedance control approach [72–74], and the virtual admittance control approach [75], as presented in Fig. 3.1.

The dual-inner-loop GFM control approach is presented in Fig. 3.1(a),
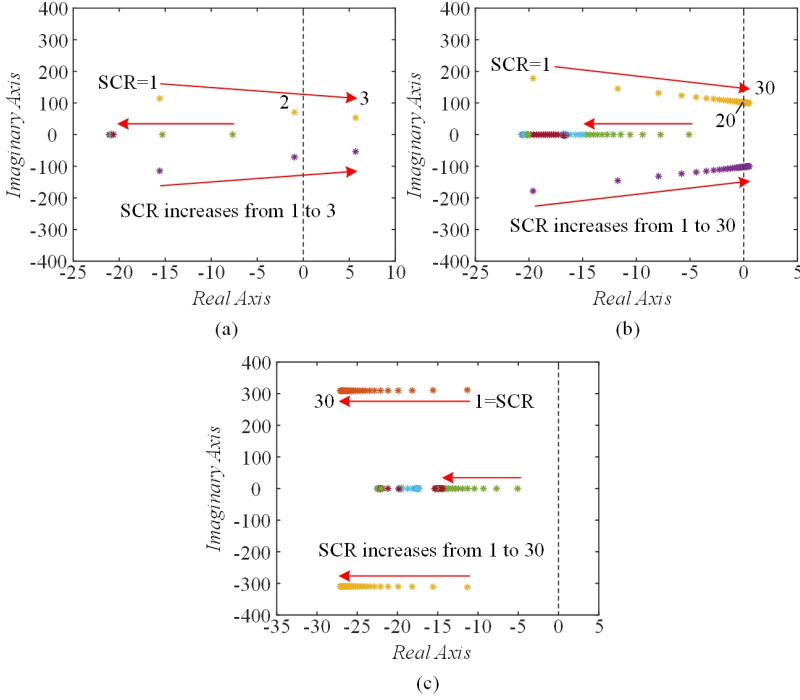
Fig. 3.2: Dominant eigenvalues of state-space models of three typical GFM control schemes. (a) Conventional dual-inner-loop control method; (b) Virtual impedance method; (c) Virtual admittance method. Source: [C5].

where G_v is the closed-loop transfer function of the inner voltage loop (See [C4] for detailed control scheme). Since inner loops are usually controlled much faster than the outer loop, the transfer function G_v is approximately equal to 1 when analyzing the outer power loop. Thus, the equivalent circuit of this method can be represented by two voltage sources e^* and v_g connecting through a grid inductance L_g. The virtual impedance control approach is presented in Fig. 3.1(b). Due to having a virtual impedance, the equivalent circuit of this method can be represented by two voltage sources e^* and v_g connecting through the inductances L_v and L_g. The virtual admittance control approach is presented in Fig. 3.1(c), where G_i is the closed-loop transfer function of the inner current loop (See Fig. 3.3 for detailed control scheme). Its equivalent circuit can be represented by two voltage sources e^* and v_g connecting through the inductances L_v and L_g.

To analyze the stability of these three methods, small-signal state-space models of them are built in [C5]. According to the state-space models, the dominant eigenvalues of these three methods with different SCRs are illustrated in Fig. 3.2. Fig. 3.2(a) shows that the system becomes unstable when

the SCR is raised to 3. So, stability range of the dual-inner-loop GFM control approach regarding the SCR can be considered as [1, 2]. Besides, Fig. 3.2(b) shows that the system becomes unstable when the SCR is increased to 20. Hence, the stability range of the virtual impedance approach can be treated as [1, 19]. Moreover, Fig. 3.2(c) presents eigenvalues of GFM inverters with the virtual admittance control. It shows that the eigenvalues go to left as the SCR increases. So, the stability range of the virtual admittance approach regarding the SCR can be considered to be [1, ∞]. Overall, since the virtual admittance scheme has wider stability range than other two schemes, the virtual admittance scheme will be the research focus in the following sections.

3.2 Virtual-Admittance-Based GFM Inverter

As illustrated in Fig. 3.1(c), the virtual admittance consists of two parameters, i.e., the virtual inductance L_v and virtual resistance R_v. Alternatively, the virtual admittance can also be expressed by the phase and the magnitude in the complex-value form. Namely, $Y_v = [|Z_v| \angle \arctan(X_v/R_v)]^{-1}$. The impact of R_v/X_v and $|Z_v|$ on small-signal stability will be discussed as follows.

3.2.1 Small-Signal Modeling of GFM Inverter

The detailed control structure of virtual-admittance-based GFM control approach is presented in Fig. 3.3, where '$ctrl$' represents the control d-q frame [C4]. To analyze its small-signal stability, the state-space model will be built as follows. Notably, 'Δ' represents a small-signal disturbance. According to Fig. 3.1(c), small-signal differential expressions of L_g-C_f-L_f in the system d-q frame can be deduced as:

$$\begin{cases} \Delta v_{Cd} - \Delta v_{gd} = L_g \frac{d\Delta i_{gd}}{dt} + R_g \Delta i_{gd} - \omega_N L_g \Delta i_{gq} \\ \Delta v_{Cq} - \Delta v_{gq} = L_g \frac{d\Delta i_{gq}}{dt} + R_g \Delta i_{gq} + \omega_N L_g \Delta i_{gd} \end{cases} \quad (3.1)$$

$$\begin{cases} \Delta i_{Ld} - \Delta i_{gd} = C_f \frac{d\Delta v_{Cd}}{dt} - \omega_N C_f \Delta v_{Cq} \\ \Delta i_{Lq} - \Delta i_{gq} = C_f \frac{d\Delta v_{Cq}}{dt} + \omega_N C_f \Delta v_{Cd} \end{cases} \quad (3.2)$$

$$\begin{cases} \Delta v_{Cd}^* - \Delta v_{Cd} = L_f \frac{d\Delta i_{Ld}}{dt} + R_f \Delta i_{Ld} - \omega_N L_f \Delta i_{Lq} \\ \Delta v_{Cq}^* - \Delta v_{Cq} = L_f \frac{d\Delta i_{Lq}}{dt} + R_f \Delta i_{Lq} + \omega_N L_f \Delta i_{Ld} \end{cases} \quad (3.3)$$

Small-signal expressions of coordinate transformations are given by (3.4)–(3.7), where $\Delta \theta_{ps}$ is the angle between control and system d-q frames [C4].

$$\begin{cases} \Delta v_{Cd}{}^{ctrl} = \Delta v_{Cd} + v_{Cq0} \cdot \Delta \theta_{ps} \\ \Delta v_{Cq}{}^{ctrl} = \Delta v_{Cq} - v_{Cd0} \cdot \Delta \theta_{ps} \end{cases} \quad (3.4)$$

$$\begin{cases} \Delta i_{gd}{}^{ctrl} = \Delta i_{gd} + i_{gq0} \cdot \Delta \theta_{ps} \\ \Delta i_{gq}{}^{ctrl} = \Delta i_{gq} - i_{gd0} \cdot \Delta \theta_{ps} \end{cases} \quad (3.5)$$
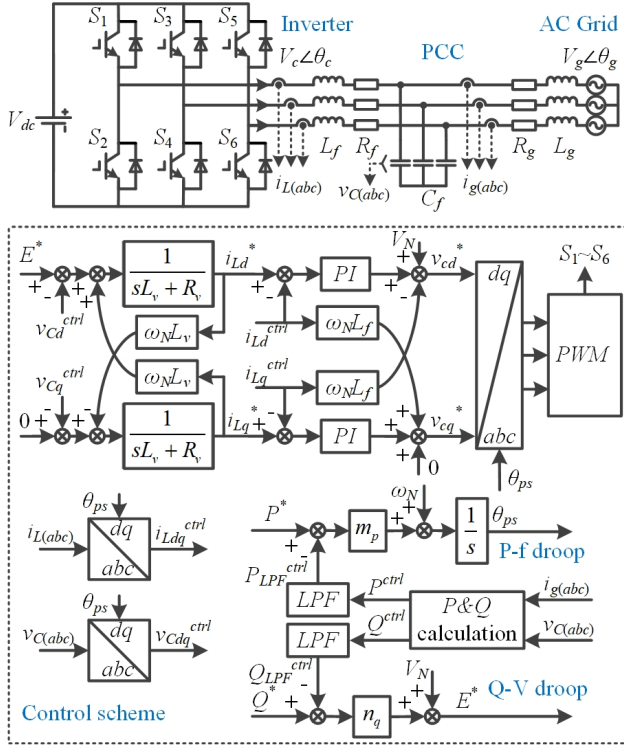
Fig. 3.3: Grid-connected inverter with virtual-admittance-based GFM control.

$$\begin{cases} \Delta i_{Ld}{}^{ctrl} = \Delta i_{Ld} + i_{Lq0} \cdot \Delta\theta_{ps} \\ \Delta i_{Lq}{}^{ctrl} = \Delta i_{Lq} - i_{Ld0} \cdot \Delta\theta_{ps} \end{cases} \tag{3.6}$$

$$\begin{cases} \Delta v_{cd}{}^* = \Delta v_{cd}{}^{*ctrl} - v_{cq0} \cdot \Delta\theta_{ps} \\ \Delta v_{cq}{}^* = \Delta v_{cq}{}^{*ctrl} + v_{cd0} \cdot \Delta\theta_{ps} \end{cases} \tag{3.7}$$

Besides, the small-signal expressions of the current control loops are deduced as:

$$\begin{cases} \frac{d\Delta Int_{id}}{dt} = \Delta i_{Ld}{}^* - \Delta i_{Ld}{}^{ctrl} \\ \Delta v_{cd}{}^{*ctrl} = K_{p\_id}(\Delta i_{Ld}{}^* - \Delta i_{Ld}{}^{ctrl}) + K_{i\_id}\Delta Int_{id} - \omega_N L_f \Delta i_{Lq}{}^{ctrl} \end{cases} \tag{3.8}$$

$$\begin{cases} \frac{d\Delta Int_{iq}}{dt} = \Delta i_{Lq}{}^* - \Delta i_{Lq}{}^{ctrl} \\ \Delta v_{cq}{}^{*ctrl} = K_{p\_iq}(\Delta i_{Lq}{}^* - \Delta i_{Lq}{}^{ctrl}) + K_{i\_iq}\Delta Int_{iq} + \omega_N L_f \Delta i_{Ld}{}^{ctrl} \end{cases} \tag{3.9}$$

where "Int" denotes a variable related to the integral operation.

Small-signal expressions of the virtual admittance are presented as:

$$\begin{cases} L_v \frac{d\Delta i_{Ld}{}^*}{dt} + R_v\Delta i_{Ld}{}^* - \omega_N L_v \Delta i_{Lq}{}^* = \Delta E - \Delta v_{Cd}{}^{ctrl} \\ L_v \frac{d\Delta i_{Lq}{}^*}{dt} + R_v\Delta i_{Lq}{}^* + \omega_N L_v \Delta i_{Ld}{}^* = 0 - \Delta v_{Cq}{}^{ctrl} \end{cases} \tag{3.10}$$

Further, the small-signal expressions of reactive and active power are calculated as:

$$\begin{cases} \Delta P^{ctrl} = \frac{3}{2}\begin{bmatrix} i_{gd0} & i_{gq0} \end{bmatrix} \cdot \begin{bmatrix} \Delta v_{Cd}^{ctrl} \\ \Delta v_{Cq}^{ctrl} \end{bmatrix} + \frac{3}{2}\begin{bmatrix} v_{Cd0} & v_{Cq0} \end{bmatrix} \cdot \begin{bmatrix} \Delta i_{gd}^{ctrl} \\ \Delta i_{gq}^{ctrl} \end{bmatrix} \\ \Delta Q^{ctrl} = \frac{3}{2}\begin{bmatrix} -i_{gq0} & i_{gd0} \end{bmatrix} \cdot \begin{bmatrix} \Delta v_{Cd}^{ctrl} \\ \Delta v_{Cq}^{ctrl} \end{bmatrix} + \frac{3}{2}\begin{bmatrix} v_{Cq0} & -v_{Cd0} \end{bmatrix} \cdot \begin{bmatrix} \Delta i_{gd}^{ctrl} \\ \Delta i_{gq}^{ctrl} \end{bmatrix} \end{cases}$$
(3.11)

In addition, small-signal expressions of the low-pass filters (LPFs) used for active and reactive power are provided as:

$$\begin{cases} \frac{d\Delta P_{LPF}^{ctrl}}{dt} + \omega_{LPF} \cdot \Delta P_{LPF}^{ctrl} = \omega_{LPF} \cdot \Delta P^{ctrl} \\ \frac{d\Delta Q_{LPF}^{ctrl}}{dt} + \omega_{LPF} \cdot \Delta Q_{PPF}^{ctrl} = \omega_{LPF} \cdot \Delta Q^{ctrl} \end{cases}$$
(3.12)

What is more, the small-signal expressions of P-f and Q-V droop control can be organized as:

$$\begin{cases} \frac{d\Delta\theta_{ps}}{dt} = \Delta\omega_{ps} = m_p \cdot (\Delta P^* - \Delta P_{LPF}^{ctrl}) \\ \Delta E = n_q \cdot (\Delta Q^* - \Delta Q_{LPF}^{ctrl}) \end{cases}$$
(3.13)

According to (3.1)–(3.13), the state-space model of GFM inverters with a virtual admittance can be deduced as:

$$\Delta\dot{\mathbf{x}}_{(13\times1)} = \mathbf{A}_{(13\times13)} \cdot \Delta\mathbf{x}_{(13\times1)} + \mathbf{B}_{(13\times4)} \cdot \Delta\mathbf{u}_{(4\times1)}$$
(3.14)

where $\Delta\mathbf{x}_{(13\times1)} = [\Delta i_{gd}, \Delta i_{gq}, \Delta v_{Cd}, \Delta v_{Cq}, \Delta i_{Ld}, \Delta i_{Lq}, \Delta Int_{id}, \Delta Int_{iq}, \Delta i_{Ld}^*, \Delta i_{Lq}^*,$ $\Delta P_{LPF}^{ctrl}, \Delta\theta_{ps}, \Delta Q_{LPF}^{ctrl}]^T$ and $\Delta\mathbf{u}_{(4\times1)} = [\Delta v_{gd}, \Delta v_{gq}, \Delta P^*, \Delta Q^*]$.

Since the small-signal stability only depends on the matrix $\mathbf{A}_{(13\times13)}$ (See [C5] for detailed expression), it will be used for stability analysis.

3.2.2 Eigenvalue Analysis for GFM Inverter

Based on the matrix $\mathbf{A}_{(13\times13)}$ in (3.14), the eigenvalues on the complex plane are illustrated in Fig. 3.4. Fig. 3.4(a) shows that as the magnitude $|Z_v|$ increases, the dominant eigenvalues move to left, so the small-signal stability becomes better. Besides, Fig. 3.4(b) shows that the dominant eigenvalues move to right when the ratio R_v/X_v increases, so the small-signal stability becomes worse. The critical stable points are found when $|Z_v| = 0.4$ p.u. and $R_v/X_v = 1.1$. Therefore, a larger $|Z_v|$ and a smaller R_v/X_v are advantageous for enhancing small-signal stability. Specifically, when designing the virtual admittance Y_v, the parameter $|Z_v|$ should be higher than 0.4 p.u., while the parameter R_v/X_v should be lower than 1.1.

Moreover, the state-space model in initial start-up process without the grid can also be built, which is simpler than the model in grid-connected mode (the order of matrix $\mathbf{A}$ is reduced from 13 to 8). The eigenvalue analysis for GFM inverter in the initial start-up mode is presented in Fig. 3.5.

Fig. 3.4: Eigenvalue analysis for GFM inverter with virtual admittance control in grid-connected mode with SCR = 2. (a) Eigenvalue analysis with different $|Z_v|$; (b) Eigenvalue analysis with different R_v/X_v. Source: [C5].

Fig. 3.5(a) shows that the critical stable value for $|Z_v|$ is 0.4 p.u., while Fig. 3.5(b) shows that the critical stable value for R_v/X_v is 1.1. They agree with the results in Fig. 3.4. Thus, the small-signal models of GFM inverters in the initial start-up and grid-connected modes have same dominant eigenvalues. Hence, both the two models can be used to analyze the stability of GFM inverters.

3.2.3 Simplified SISO Stability Analysis Method

In the previous section, the state-space models of GFM inverters have been built to analyze the small-signal stability. However, they are not convenient to use, because the state-space models are relatively complicated. In this section, a simple SISO stability analysis approach based on the impedance model of GFM inverters will be introduced, which is easier to use.
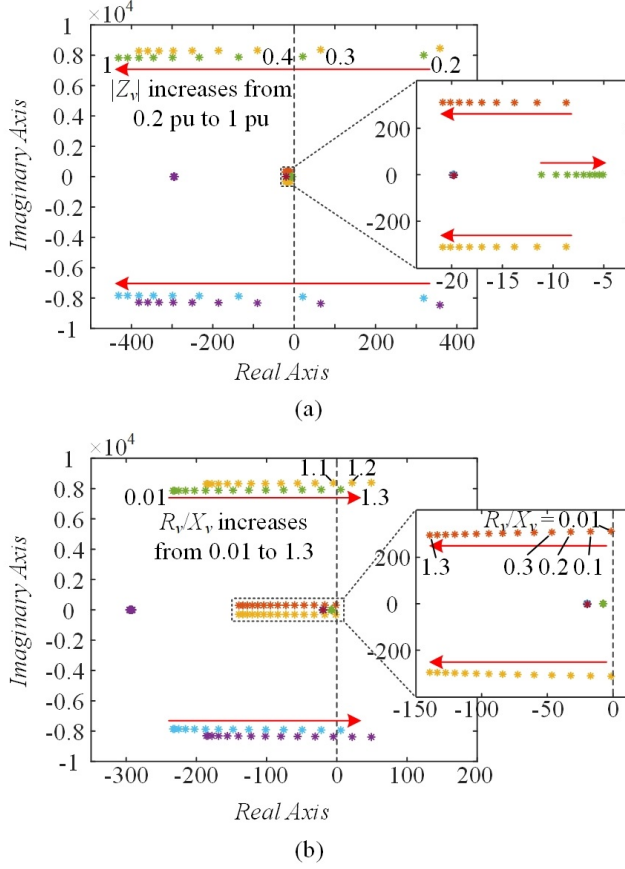
(a)

(b)
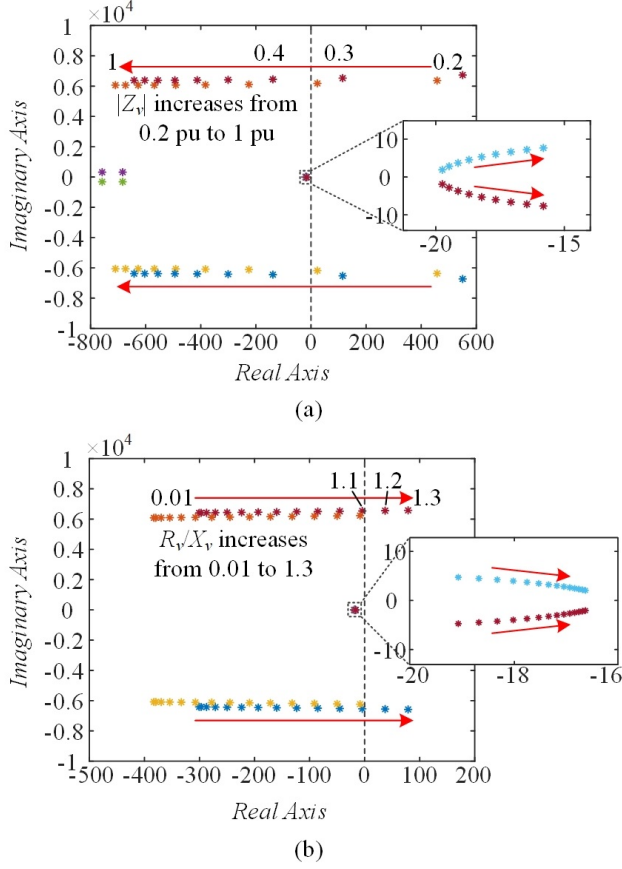
Fig. 3.5: Eigenvalue analysis for GFM inverter with virtual admittance control in initial start-up mode with SCR = 2. (a) Eigenvalue analysis with different $|Z_v|$; (b) Eigenvalue analysis with different R_v/X_v. Source: [C5].

Since time-domain and frequency-domain models are convertible equivalently, the time-domain state-space model in (3.14) is able to be transformed to the frequency-domain model in Fig. 3.6, where the model in grid-connected mode is presented in Fig. 3.6(a), while the model in initial start-up mode is shown in Fig. 3.6(b). As aforementioned, both the two models can be used to analyze the stability. Thus, according to Fig. 3.6(b), the open-loop transfer function (from $\Delta \mathbf{e_{dq}}^*$ to $\Delta \mathbf{v_{Cdq}}$) can be deduced as:

$$\mathbf{T}_{\text{ol}}(s) = \mathbf{B}_{\text{Lv}}{}^{-1} \cdot [(\mathbf{B}_{\text{Lf}} + \mathbf{B}_{\text{PI-I}} - \mathbf{B}_{\text{decpl}})\mathbf{B}_{\text{Cf}} + \mathbf{I}]^{-1} \cdot \mathbf{B}_{\text{PI-I}} \qquad (3.15)$$

Furthermore, since all the matrixes $\mathbf{B}$ in (3.15) are symmetric (See [C4] for detailed expressions), they can be transformed to the complex vector form. Thus, the corresponding complex vector expression can be deduced as:

3.2. Virtual-Admittance-Based GFM Inverter

(a)

(b)
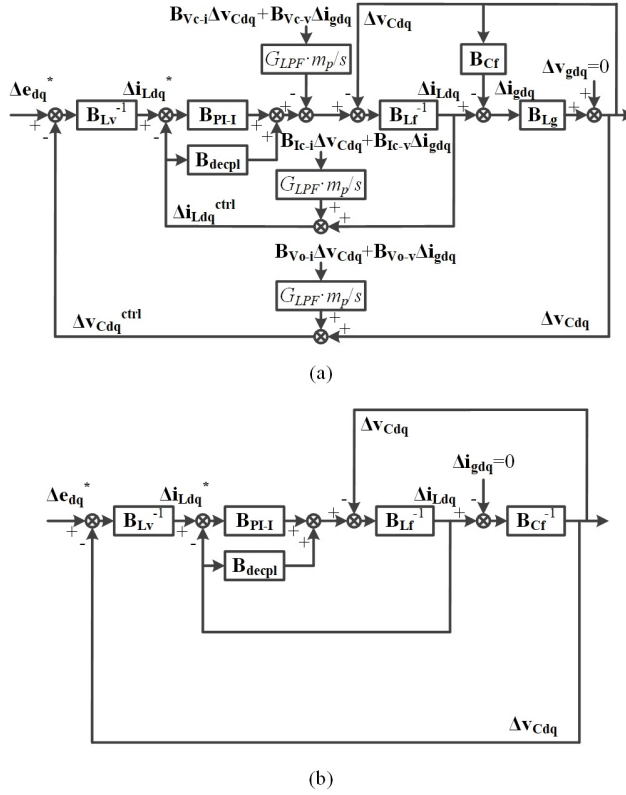
Fig. 3.6: Frequency-domain d-q impedance models of GFM inverter with virtual admittance control. (a) Grid-connected mode; (b) Initial start-up mode without the grid. Source: [C5].

$$T_{ol}(s) = \frac{\frac{1}{sL_v + R_v + j\omega_1 L_v} \cdot (K_{p\_idq} + K_{i\_idq}/s)}{(sL_f + R_f + K_{p\_idq} + K_{i\_idq}/s) \cdot (sC_f + j\omega_1 C_f) + 1} \tag{3.16}$$

Thus, the conventional SISO stability analysis method based on Bode diagrams can be utilized for stability analysis. According to the transfer function $T_{ol}(s)$ in (3.16), the Bode diagrams of $T_{ol}(s)$ are presented in Fig. 3.7. Fig. 3.7(a) shows that the GFM inverter is unstable when $|Z_v|$ is lower than 0.4 p.u. Reversely, when $|Z_v|$ is higher than 0.4 p.u., it is stable. Hence, 0.4 p.u. can be treated as a critical stable value of $|Z_v|$. Similary, the Bode diagrams in Fig. 3.7(b) indicate that the critical stable value of R_v/X_v is 1.1. The outcomes shown in Fig. 3.7 agree well with that in Fig. 3.4 and Fig. 3.5. Therefore, the SISO stability analysis method can be used for designing the parameters $|Z_v|$ and R_v/X_v, which is easier and more convenient to use.

In order to validate the correctness of above analysis, a time-domain simulation model of virtual-admittance-based GFM converter is established in MATLAB/Simulink. The simulation outcomes with various R_v/X_v and $|Z_v|$

49
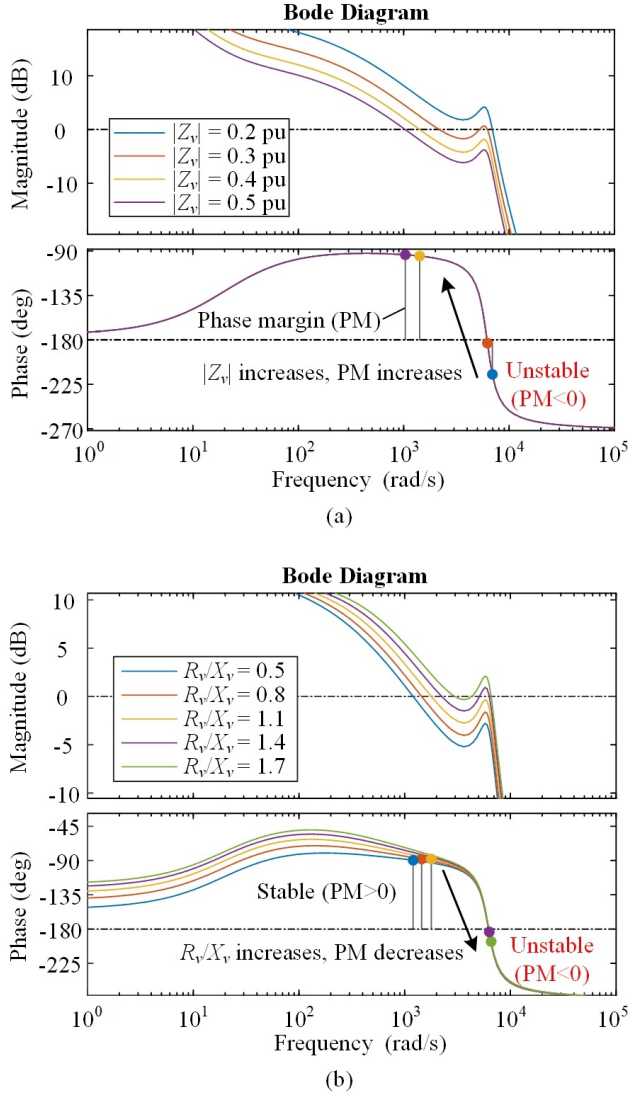
Fig. 3.7: Bode diagrams of the transfer function $T_{ol}(s)$. (a) Phase magin with different $|Z_v|$; (b) Phase magin with different R_v/X_v. Source: [C5].

are presented in Fig. 3.8 and Fig. 3.9, where a strong grid case (SCR = 30) and a weak grid case (SCR = 1) are chosen to check the stability. Fig. 3.8 shows that when $|Z_v|$ is decreased from 0.5 p.u. to 0.3 p.u., the GFM inverter becomes unstable. Later, when $|Z_v|$ is increased to 0.5 p.u., it is stable again. Moreover, Fig. 3.9 shows that when R_v/X_v is raised from 0.1 to 1.2, the GFM inverter becomes unstable. Later, when R_v/X_v is reduced to 0.1, it is stable again. Obviously, the identical stability feature can be seen in both weak and
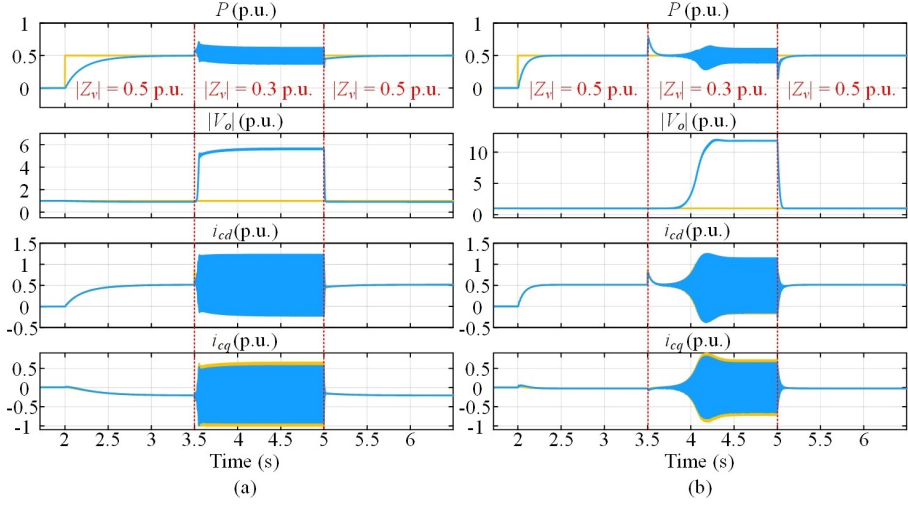
Fig. 3.8: Simulation results of virtual-admittance-based GFM inverters ($|Z_v|$ changes between 0.5 p.u. and 0.3 p.u.). (a) Weak grid case (SCR = 1); (b) Strong grid case (SCR = 30). Source: [C5].
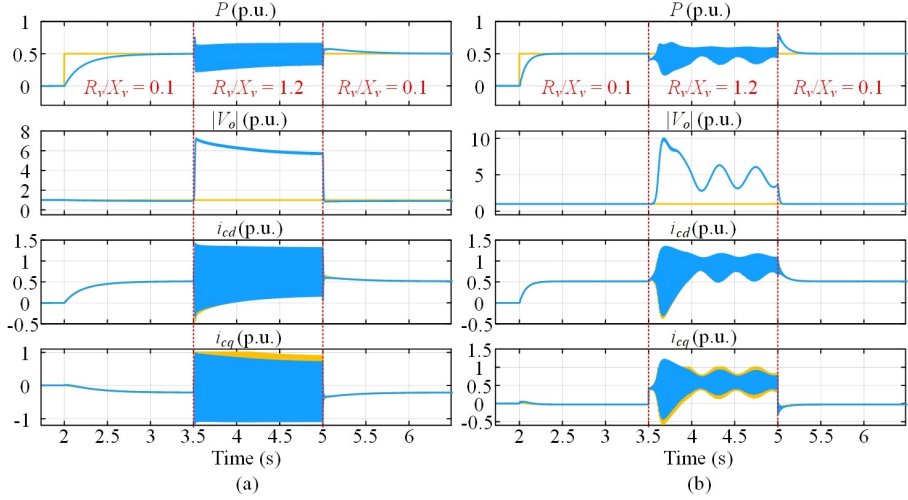
Fig. 3.9: Simulation results of virtual-admittance-based GFM inverters (R_v/X_v changes between 0.1 and 1.2). (a) Weak grid case (SCR = 1); (b) Strong grid case (SCR = 30). Source: [C5].

strong grid cases. These simulation outcomes are consistent to the previous analysis in Fig. 3.7. In addition, Fig. 3.8 and Fig. 3.9 show that when $|Z_v|$ and R_v/X_v are well-designed, the GFM inverter with virtual admittance control can be stablized within a wide range of the SCR. So, the small-signal stability of GFM inverters is already acceptable, but they have instability problems under large grid disturbances. It will be discussed in the next section.

3.3 Proposed Overcurrent Protection Method

As discussed in the previous section, GFM inverters with virtual admittance control show good small-signal stability when the control parameters are well-designed. Hence, the small-signal stability of the GFM inverter with virtual admittance control is acceptable in normal grid cases. However, the overcurrent protection of GFM inverters under large disturbances is still a challenge, because the typical current reference limitation approach tends to be unstable during large voltage or frequency disturbances, and existing improved overcurrent protection methods have their own limitations [J3]. Therefore, an effecitve overcurrent protection method for GFM inverters need to be developed, which will be discussed in this section.

3.3.1 Problems of Existing Overcurrent Protection Methods

To prevent the output current of the inverter from exceeding the rated value, an additional current reference limiter is usually utilized. When the current reference limiter is embedded in the GFM inverter, the overall schematic diagram is presented in Fig. 3.10(a), where the subscripts '$_{dq}$, $_{\alpha\beta}$, and $_{abc}$' denote variables in dissimilar coordinate systems. Same as Fig. 3.1(c), the virtual admittance control is used for the voltage control, and the PI control is used for the current control. Besides, the typical Q-V and P-f droop control at the outer loop are used to control the reactive and active power. To simplify the analysis, the equivalent circuit is also provided in Fig. 3.10(b), where a virtual inductance L_v and a virtual resistance R_v are included. Considering R_v is relatively small, it is assumed to be 0 when analyzing the outer power loop.

Firstly, to have better understanding for the instability problem resulted from the current reference limitation approach on GFM inverters, the theoretical analysis in [54] and [76] is revisited. The current and voltage vector diagrams of GFM inverters are presented in Fig. 3.11. ϕ is the angle between $\mathbf{i_L}$ and $\mathbf{e}^*$, while δ is the angle between $\mathbf{v_g}$ and $\mathbf{e}^*$. Fig. 3.11(a) shows that when the limiter is not saturated (under the normal condition), the output power of GFM inverters is determined by the voltage vectors $\mathbf{v_g}$ and $\mathbf{e}^*$. Thus, the output power fulfills the P-δ equation (3.17) very well. Differently, as illustrated in Fig. 3.11(b), when the limiter is saturated (under the overcurrent condition), GFM inverters is able to be treated as a current source with the constant amplitude. In this case, the output power of GFM inverters depends on the vectors $\mathbf{v_g}$ and $\mathbf{i_L}$, which meets (3.18).

$$P = \frac{3}{2} \cdot \frac{V_g \cdot E^*}{X_v + X_g} \cdot \sin(\delta) \tag{3.17}$$

where V_g and E^* are the amplitudes of vectors $\mathbf{v_g}$ and $\mathbf{e}^*$.
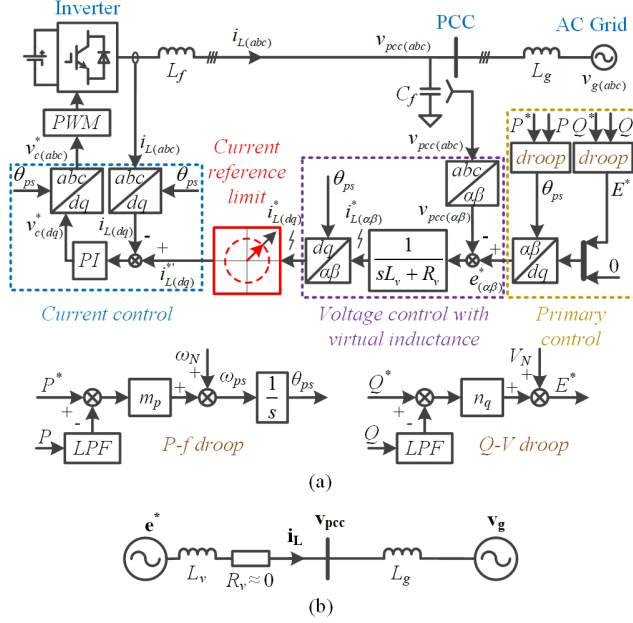
Fig. 3.10: Configuration of typical droop-based GFM inverters with a current reference limiter. (a) An existing GFM inverter control approach; (b) The equivalent circuit. Source: [J3].
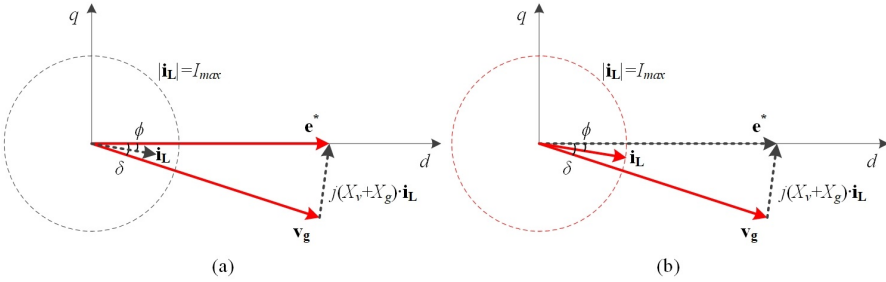
Fig. 3.11: Current and voltage vector diagrams of GFM inverters. (a) Unsaturated case of the limiter; (b) Saturated case of the limiter. Source: [J3].

$$P = \frac{3}{2} \cdot V_g \cdot I_{max} \cdot \cos(\delta - \phi) \tag{3.18}$$

Like [76], the angle ϕ in Fig. 3.11 is supposed to be tiny for the qualitative analysis. So, based on (3.17) and (3.18), operation trajectories of GFM inverters in the case of grid frequency drop are presented in Fig. 3.12. Fig. 3.12(a) shows that the operation trajectory complies with the curve A-B-C-D when there is no current limit. Supposing that the amplitude of the current gets its maximum value I_{max} at point B. Thus, the steady-state operating point will
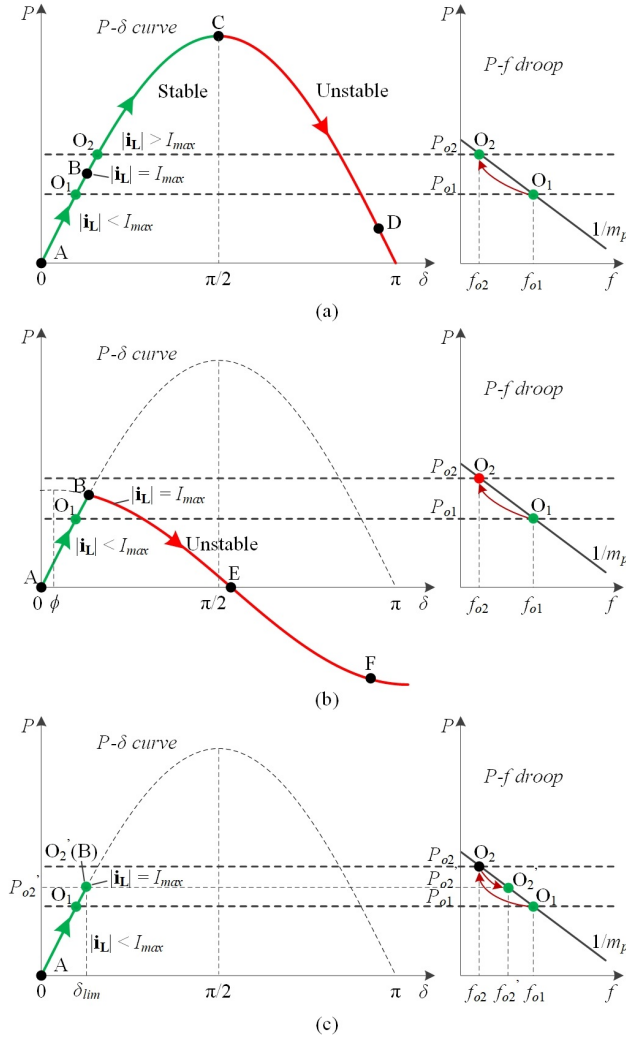
Fig. 3.12: Theoretical trajectories of GFM inverters in the case of grid frequency drop. (a) Without current limitation; (b) With current reference limitation; (c) With power angle limitation. Source: [J3].

move from O_1 to O_2 when the frequency of the grid is reduced from f_{o1} to f_{o2}. So, the output current amplitude is larger than I_{max}. Under this circumstance, the GFM inverter can operate stably. However, the output current is beyond its rated range. To restrict the output current, a conventional way is to restrict the reference value of the current controller. Fig. 3.12(b) shows that the operation trajectory complies with the curve A-B-E-F when the current reference limiter is used. In this case, there will be no equilibrium point on the *P-δ* trajectory when the grid frequency is dropped from f_{o1} to f_{o2}.
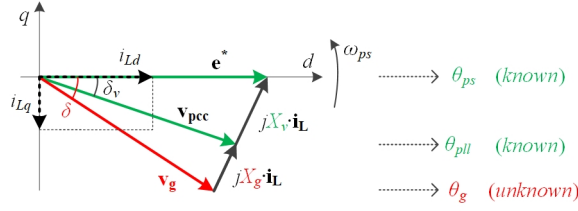
Fig. 3.13: Voltage vector diagrams of GFM inverters in the d-q frame. Source: [J3].
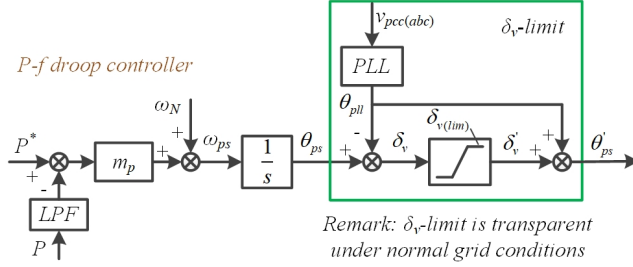
Fig. 3.14: Proposed virtual power angle limitation approach. Source: [J3].

Obviously, the GFM inverter becomes unstable. To address such instability issue, a novel idea is proposed. As illustrated in Fig. 3.12(c), when the grid frequency is dropped to f_{o2}, the output power is able to be restricted to P_{o2}' if the power angle could be restricted to δ_{lim}. So, the operation trajectory stay at point B eventually. It means that point O_2' is the ultimate stable equilibrium point. The detailed control scheme of the proposed idea will be illustrated in the following sections.

3.3.2 Proposed Initial Power-Angle Limiting Method

To achieve the proposed idea of power angle limitation shown in Fig. 3.12(c), a few actual factors should be considered. The vector diagram of GFM inverters with a virtual inductance is presented in Fig. 3.13. Since grid inductance L_g and the grid voltage $\mathbf{v_g}$ are unknown generally, the actual power angle δ is hard to be got. So, the power angle δ is not easy to be applied to implement the power limitation directly. Nevertheless, a virtual power angle δ_v can be got easily, which is equal to the difference of two angles θ_{ps}-θ_{pll}. Notably, θ_{ps} is the phase of $\mathbf{e}^*$, output from the P-f droop controller. And θ_{pll} is the phase of $\mathbf{v_{pcc}}$. It is able to be got by a PLL [J2].

Therefore, the proposed power angle limitation approach is presented in Fig. 3.14. It shows that the δ_v-*limit* block in Fig. 3.14 is transparent in the normal case (i.e., $\delta_v' = \delta_v$ and $\theta_{ps}' = \theta_{ps}$). However, in the overcurrent case, δ_v' is equal to the limiting value $\delta_{v(lim)}$.
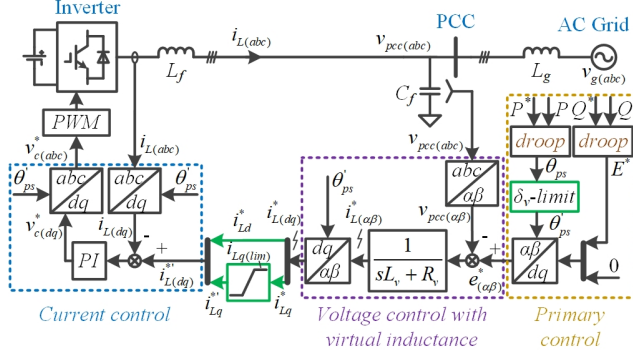
Fig. 3.15: Proposed overcurrent protection solution for GFM inverters. Source: [J3].

According to Fig. 3.13, the relationship between the virtual power angle δ_v and active power P fulfills the P-δ equation presented in (3.19).

$$P = \frac{3}{2} \cdot \frac{V_{pcc} \cdot E^*}{X_v} \cdot \sin(\delta_v) \tag{3.19}$$

where V_{pcc} and E^* are the magnitude of the vectors $\mathbf{v_{pcc}}$ and $\mathbf{e}^*$.

Hence, the equation of the virtual power angle δ_v can be deduced as:

$$\delta_v = \arcsin\left(\frac{P}{3/2 \cdot E^* \cdot V_{pcc}/X_v}\right) \tag{3.20}$$

In addition, based on the current and voltage vector diagrams in Fig. 3.13, it shows that the relationship of the d-component current i_{Ld} and the power P fulfills (3.21).

$$P = 3/2 \cdot E^* \cdot i_{Ld} \tag{3.21}$$

Substituting (3.21) into (3.20), the equation of the virtual power angle is able to be deduced as (3.22).

$$\delta_v = \arcsin\left(\frac{i_{Ld} \cdot X_v}{V_{pcc}}\right) \tag{3.22}$$

Consequently, the limiting value $\delta_{v(lim)}$ can be derived as:

$$\delta_{v(lim)} = \arcsin\left(\frac{i_{Ld(lim)} \cdot X_v}{V_{pcc}}\right) \tag{3.23}$$

where $i_{Ld(lim)}$ is the limit of the d-axis current component.

In this thesis, the maximum current I_{max} of inverters is designed as 1 p.u. for analysis. Moreover, to remain a little reactive power output capability, the limit of d-component current $i_{Ld(lim)}$ is designed to be 0.9 p.u. Besides, to ensure the amplitude of the output current is no more than I_{max}, the q-component current could be restricted by $i_{Lq(lim)}$ in (3.24).

$$i_{Lq(lim)} = \sqrt{I_{max}{}^2 - i_{Ld}^*{}^2} \qquad (3.24)$$

Based on the above analysis, the proposed overcurrent protection approach for GFM inverters is presented in Fig. 3.15, where the difference between Fig. 3.10 and Fig. 3.15 is marked in green. In Fig. 3.15, the reactive power seems not being restricted. Nevertheless, the reactive power is restricted indirectly as long as i_{Lq}^* is limited.

Therefore, the output power and the current can be limited by the proposed virtual power angle limiting approach in the frequency drop scenario. Nevertheless, it may still be unstable in the grid voltage sag scenario, since there will be no equilibrium point when the amplitude of grid voltage is very low during the fault event. To make the proposed approach also effective in the grid voltage sag scenario, the limiting value of the virtual power angle in (3.23) should be redesigned [J3].

3.3.3 Proposed Improved Power-Angle Limiting Method

According to (3.19), the amplitude of grid voltage V_g is proportional to the active power P. So, while V_g is decreased, P is also decreased. Thus, the inverter might not have the ability to output enough power to the grid in the grid voltage sag scenario. Therefore, suitable power reduction is needed, because it can ensure the existence of a stable equilibrium point.

Theoretical trajectories of GFM inverters in the case of grid voltage sag are presented in Fig. 3.16. Fig. 3.16(a) shows that while the amplitude of the grid voltage is decreased from V_{g0} to V_{g1}, the operation trajectory is altered from A-B-C-D to A-B'-C'-D'. So, even though P can be restricted to P_{lim}, there will be no equilibrium point on A-B'-C'-D', since the maximum output power at the point C' is smaller than P_{lim}.

To solve the instability issue resulted from the grid voltage sag, modifying the power limiting value based on the amplitude of grid voltage is a possible way, such as "$P_{lim}^{new} = P_{lim} \cdot V_{g(p.u.)}$" [58]. Fig. 3.16(b) shows that while the limiting value of P is changed to P_{lim}^{new}, a new stable equilibrium point B' appears after the grid voltage sag. Besides, it can be seen from (3.19), the amplitude of the PCC voltage is also proportional to the active power P, so the limiting value of P can be changed according to the PCC voltage, such as "$P_{lim}^{new} = P_{lim} \cdot V_{pcc(p.u.)}$".

Furthermore, since the d-axis current component i_{Ld} is also proportional to P according to (3.21), changing the d-axis current limitation is equivalent to changing the active power limitation. So, the limiting value $i_{Ld(lim)}$ is able to be redesigned as:

$$i_{Ld(lim)}^{new} = V_{pcc(p.u.)} \cdot i_{Ld(lim)} \qquad (3.25)$$

Thus, the limiting value of the virtual power angle in (3.23) is able to be redesigned as:
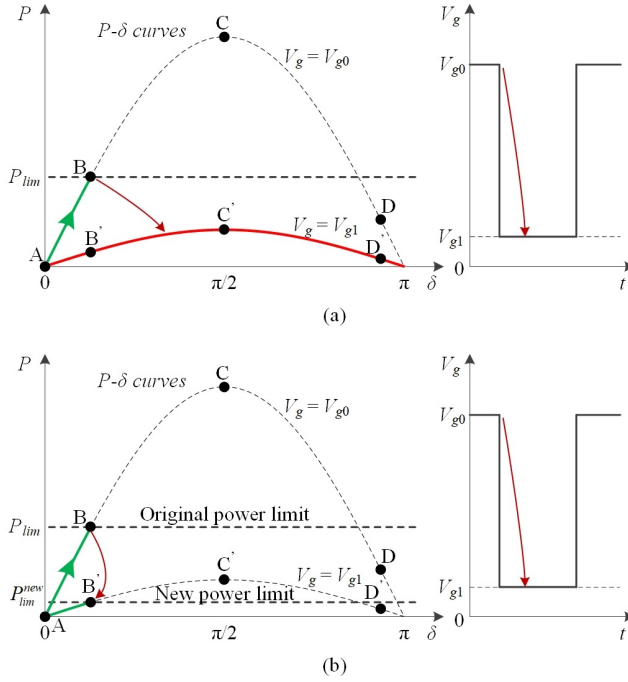
Fig. 3.16: Theoretical trajectories of GFM inverters in the case of grid voltage sag. (a) Initial power limitation approach; (b) Improved power limitation approach. Source: [J3].

$$\delta_{v(lim)}^{new} = \arcsin \left(\frac{V_{pcc(p.u.)} \cdot i_{Ld(lim)} \cdot X_v}{V_{pcc}} \right) \qquad (3.26)$$

So, based on the equation "$V_{pcc(p.u.)} = V_{pcc}/V_N$", (3.26) can be rewritten as:

$$\delta_{v(lim)}^{new} = \arcsin \left(\frac{i_{Ld(lim)} \cdot X_v}{V_N} \right) \qquad (3.27)$$

Notably, in (3.27), $i_{Ld(lim)}$ is the limiting value of d-component current, X_v is the virtual inductance, and V_N is the rated voltage. All these three parameters are constant. So, $\delta_{v(lim)}^{new}$ is also constant, which does not need to be tuned in any case. It is worth mentioning that although $\delta_{v(lim)}^{new}$ is invariable, P_{lim}^{new} can be adaptive to the variation of grid voltage, as illustrated in Fig. 3.16(b). Hence, this proposed approach does not need grid fault detection [J3].

To validate the effectiveness of proposed overcurrent protection method, an 800 W GFM inverter model is built in MATLAB/Simulink (See [J3] for the detailed parameters). The simulation results with different current limitation approaches in the case of grid frequency drop are presented in Fig. 3.17. The simulation outcomes in a strong grid case (SCR = 15) are compared in Fig. 3.17(a)-(c). In the beginning, the power reference is 0.5 p.u. Then, at the moment of 3s, a grid frequency drop event happens. Fig. 3.17(a) presents
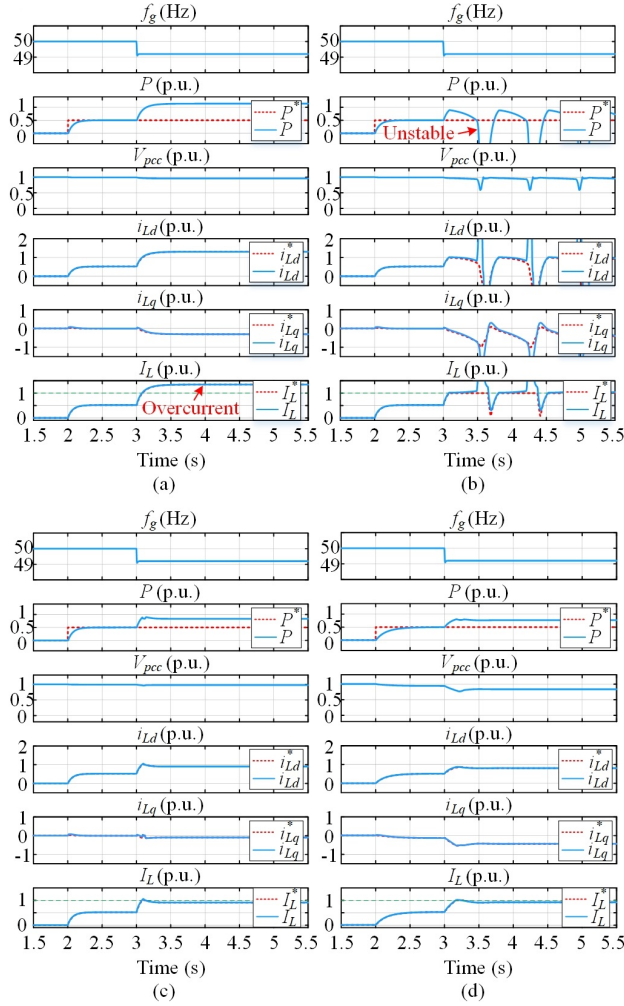
Fig. 3.17: Simulation outcomes of GFM inverters with dissimilar current limitation approaches in the case of grid frequency drop. (a) Without any current limitation (SCR = 15); (b) With current reference limitation (SCR = 15); (c) With power angle limitation (SCR = 15); (d) With power angle limitation (SCR = 1.5). Source: [J3].

the simulation outcome without any current limitation. It shows that while the grid frequency (f_g) is reduced to 49.2 Hz, the active power is larger than 1 p.u., which causes the overcurrent operation of the GFM inverter. Under this circumstance, the GFM inverter is stable, however, the output current is beyond its rated range. This result is consistent to the analyses in Fig. 3.12(a). Besides, Fig. 3.17(b) shows that while the typical current reference limitation approach is applied, the amplitude of the current reference is restricted to 1 p.u. Nevertheless, the GFM inverter becomes unstable when the grid fre-
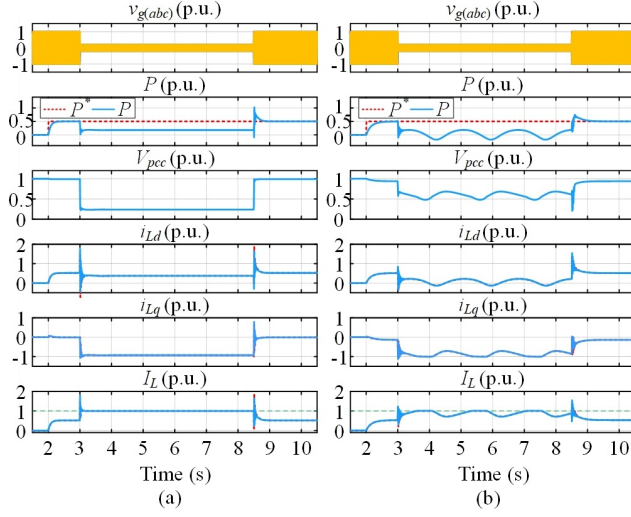
Fig. 3.18: Simulation outcomes of GFM inverters with proposed power angle limitation approach in the case of grid voltage sag. (a) SCR = 15; (b) SCR = 1.5. Source: [J3].

quency is reduced to 49.2 Hz and triggering the current limiter. This result agrees with the analyses in Fig. 3.12(b). Dissimilarly, Fig. 3.17(c) shows that while the power angle limitation approach is applied, the amplitude of the output current is able to be restricted within 1 p.u. stably when the grid frequency is reduced to 49.2 Hz. This result is consistent to the analyses in Fig. 3.12(c). Furthermore, a weak grid case (SCR = 1.5) is chosen to evaluate the effectiveness of the proposed approach. Fig. 3.17(d) shows that the proposed overcurrent protection approach is also effective in weak grid case.

Additionally, the simulation outcomes of the proposed overcurrent protection approach in the case of grid voltage sag are presented in Fig. 3.18, where the amplitude of the grid voltage is decreased from 1 p.u. to 0.2 p.u. The simulation results under strong grid conditions (SCR = 15) and weak grid conditions (SCR = 1.5) are presented in Fig. 3.18(a) and (b). It shows that the amplitude of the output current is able to be restricted within 1 p.u. by using the proposed power angle limiting approach in either weak or strong grid case. Besides, after the fault is cleared, the recovery process shows good transient performance.

Moreover, the experiment is carried out to validate the effect of the proposed overcurrent protection approach for GFM inverters, where the experimental parameters are as same as that used in simulation (See [J3] for detailed parameters). As shown in Fig. 1.10 in Section 1, the Danfoss FC103P11KT11 is used to implement a grid-connected inverter, and the dSPACE1007 is used to implement the control algorithms. Besides, a grid simulator (Chroma 61845) and inductors (L_g) are used to achieve a strong/weak grid condition.

3.3. Proposed Overcurrent Protection Method
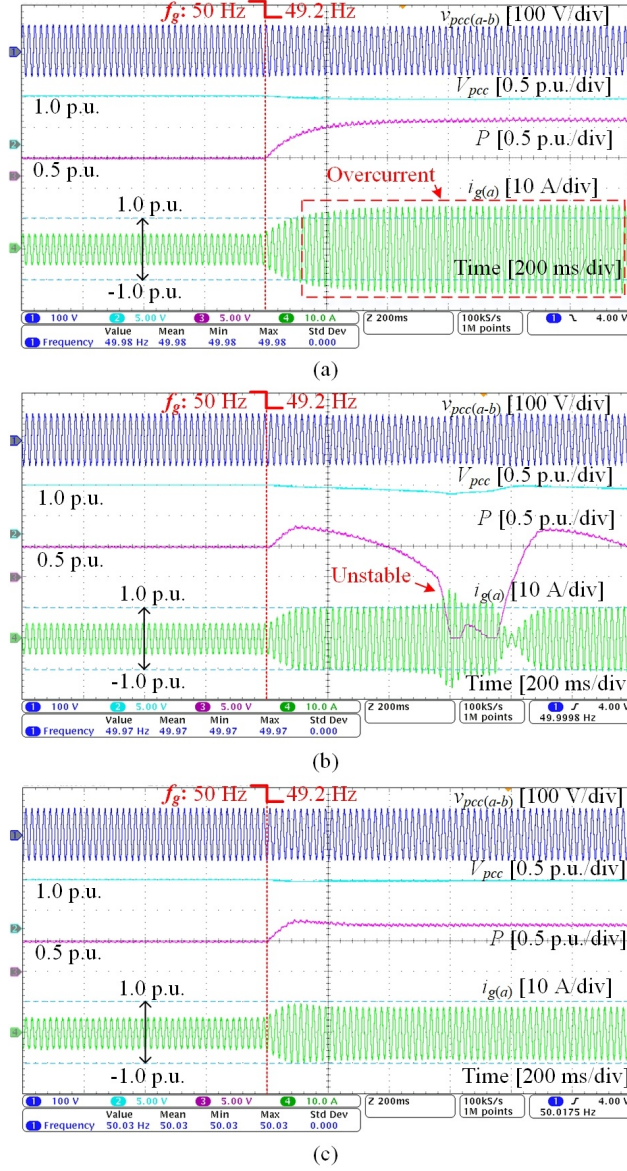
Fig. 3.19: Experimental results of dissimilar current limitation approaches under grid frequency drop from 50 Hz to 49.2 Hz in strong grids (SCR = 15) (CH4: grid phase current; CH3: active power; CH2: PCC voltage amplitude; CH1: phase-to-phase voltage at the PCC). (a) Without any current limitation; (b) With current reference limitation; (c) With proposed power angle limitation. Source: [J3].

The experimental outcomes with dissimilar current limitation approaches in the case of grid frequency drop are presented in Fig. 3.19, where a strong
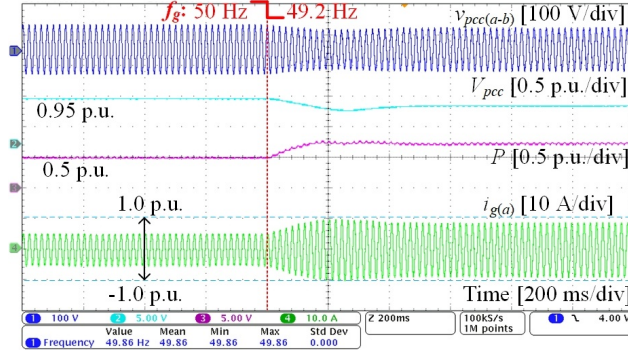
Fig. 3.20: Experimental results of power angle limitation approach under grid frequency drop from 50 Hz to 49.2 Hz in weak grids (SCR = 1.5) (CH4: grid phase current; CH3: active power; CH2: PCC voltage amplitude; CH1: phase-to-phase voltage at the PCC). Source: [J3].
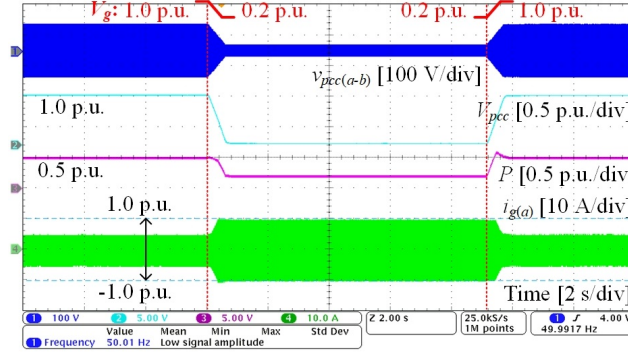
(a)
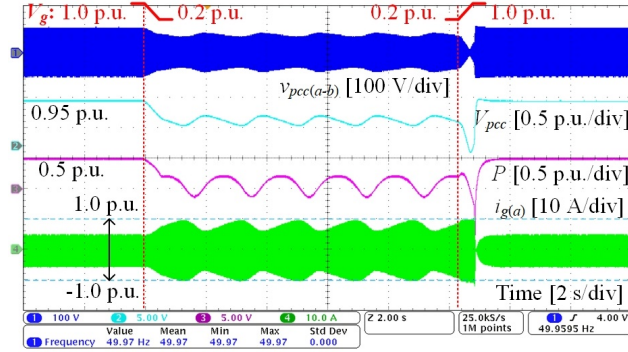
(b)

Fig. 3.21: Experimental results of power angle limitation approach under grid voltage sag from 1 p.u. to 0.2 p.u. (a) Strong grid case (SCR = 15); (b) Weak grid case (SCR = 1.5) (CH4: grid phase current; CH3: active power; CH2: PCC voltage amplitude; CH1: phase-to-phase voltage at the PCC). Source: [J3].

Table 3.1: Comparison of dissimilar overcurrent protection approaches [J3].

Methods	No need of grid fault detection	Smooth transient transition	Robust to SCR variation	Effective in grid voltage sag case	Effective in grid frequency drop case
Switching control modes [55]	✗	✗	✓	✓	✓
Adding virtual impedance [57]	✓	✗	✗	✓	✓
Tuning power reference [58]	✗	✓	✓	✓	✗
Voltage-based feedforward [59]	✓	✓	✓	✓	✗
Power-based feedforward [60]	✓	✓	✓	✗	✓
Proposed method	✓	✓	✓	✓	✓

grid case (SCR = 15) is chosen for study. Similar to the simulation, the initial power reference is 0.5 p.u. Fig. 3.19(a) presents the experimental outcome without any current limit. While the grid frequency (f_g) is decreased from 50 Hz to 49.2 Hz, the amplitude of the output current is raised to 1.3 p.u. roughly. Under this circumstance, the GFM inverter is stable. However, the output current is beyond the rated range. Besides, Fig. 3.19(b) shows that while the typical current reference limitation approach is applied, the GFM inverter becomes unstable when the grid frequency is reduced from 50 Hz to 49.2 Hz and triggering the current limiter. It agrees with the simulation outcomes in Fig. 3.17(b). Dissimilarly, Fig. 3.19(c) shows that when the proposed power angle limitation approach is applied, the output current is restricted within 1 p.u. stably when the grid frequency is dropped from 50 Hz to 49.2 Hz. It matches the simulation outcomes in Fig. 3.17(c).

Additionally, the experiment outcomes of the proposed overcurrent protection approach under weak grid conditions during grid frequency drop event are presented in Fig. 3.20. It shows that the amplitude of the current can be restricted within 1 p.u. when the grid frequency is reduced from 50 Hz to 49.2 Hz. This result matches the simulation outcomes in Fig. 3.17(d).

Further, the experiment outcomes of the proposed overcurrent protection approach during grid voltage sag event are presented in Fig. 3.21, where the amplitude of the grid voltage is decreased from 1 p.u. to 0.2 p.u. A weak grid case (SCR = 1.5) and a strong grid case (SCR = 15) are chosen for study. It shows that the amplitude of the output current can be restricted no more than 1 p.u. in either strong or weak grid case. The experiment outcomes in Fig. 3.21(a) and (b) are consistent to the simulation outcomes in Fig. 3.18(a) and (b). Notably, the low-frequency oscillation at nearly 0.5 Hz can be seen in Fig. 3.21(b). Finding an improved approach to get rid of the low-frequency oscillation is worth doing in the future.

Finally, advantages of the proposed approach compared to several existing approaches (i.e., control-mode-switching approach [55], virtual impedance approach [57], modifying power reference approach [58], voltage-based frequency feedforward approach [59], and power-based frequency feedforward approach [60]) are briefly discussed. As listed in Table 3.1, the proposed

overcurrent protection approach of GFM inverters is effective for either grid frequency drop or voltage sag case. Besides, seamless transition between the fault and normal grid cases are realized. Moreover, grid fault detection is unnecessary because the proposed approach can be adaptive to the variation of the amplitude of grid voltage. Therefore, this proposed overcurrent protection approach has more advantages than existing methods presented in [55–60], which seems to be a potential control solution to protect GFM inverters to avoid overcurrent.

3.4   Summary

This chapter has provided a comprehensive discussion of modeling, small-signal stability analysis, and overcurrent protection approaches of GFM inverters. At first, three typical GFM control schemes are compared under normal grid conditions. It is found that the virtual-admittance-based GFM control scheme has a wider stability range than the other two methods, so the virtual admittance control scheme is chosen to be studied. Then, a detailed state-space model and a simplified impedance model of GFM inverters with virtual admittance control are built to analyze the small-signal stability. Based on the stability analyses, the parameters of the virtual resistance R_v and the virtual inductance L_v are able to be designed properly to ensure the GFM inverter system is stable within a wide range of the SCR. Thus, the stability of GFM inverters under normal grid conditions is acceptable.

Afterwards, the stability of GFM inverters under abnormal grid conditions is studied. To make GFM inverters with the current limitation operate stably under large grid disturbances, a power-angle-based overcurrent protection method is proposed. The proposed approach can not only limit the current of GFM inverters effectively, but also ensure the existence of a stable equilibrium point under large grid voltage and frequency disturbances. Hence, the stability can be maintained. Besides, the proposed overcurrent protection approach has some significant advantages. For example, the proposed approach is effective for either grid voltage sag or grid frequency drop case. It does not need additional grid fault detection. In addition, smooth transition between the fault and normal grid conditions can be realized. This is beneficial for improving the transient performance. Finally, simulations and experiments have demonstrated the effectiveness of the proposed overcurrent protection approach for GFM inverters.

Chapter 4

Control and Impedance Modeling of Grid-Connected PMSG

In previous chapters, the GFL and GFM control schemes on grid-connected inverters have been discussed. However, the electrical machines in Type-4 and Type-3 wind generation systems (i.e., PMSGs and DFIGs) have not been considered, which will be discussed in the following chapters. In this chapter, the control and small-signal impedance modeling approaches of GFL and GFM Type-4 wind generation systems will be introduced. Finally, the calculated and measured impedances in the frequency domain will be compared to show the correctness of the developed modeling approach.

4.1 Control and Impedance Modeling of GFL-PMSG

In Type-4 wind power generators, the back-to-back converter has a dc bus (also called "dc link"). Whether the MSC or GSC should be responsible to regulate the dc-link voltage is still an open research question. In this section, the stability and dynamic performance of the Type-4 wind generators with two typical GFL control schemes (i.e., machine-side and grid-side dc-link voltage controls) will be compared at first.

   The GFL-PMSG with the dc voltage control on the GSC is presented in Fig. 4.1(a), where the MSC is utilized to control the rotor speed of the PMSG. In this case, the MPPT can be achieved on the MSC by tuning the rotor speed reference according to the wind speed. Differently, the GFL-PMSG with the dc voltage control on the MSC is presented in Fig. 4.1(b), where the GSC is utilized to control the output power. In this case, the MPPT is able to be

(a)

(b)
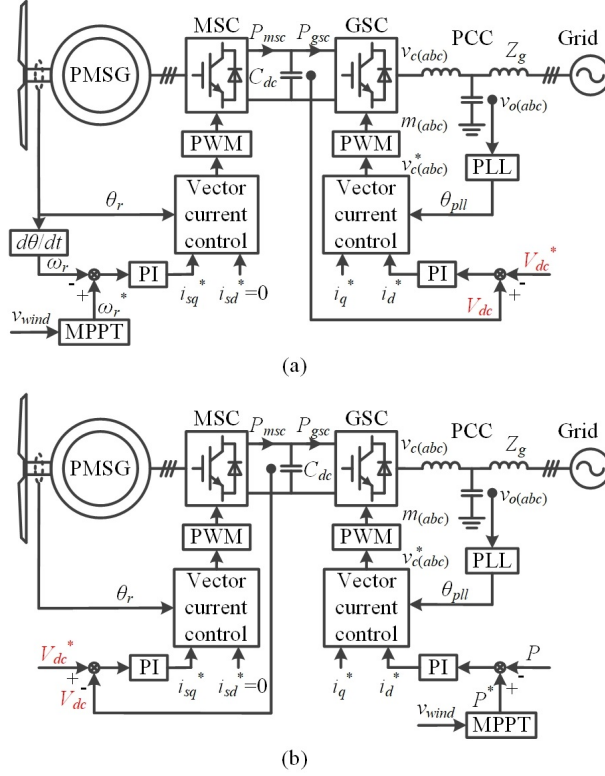
Fig. 4.1: Two typical but different GFL control approaches for Type-4 wind generators. (a) With dc voltage control on GSC; (b) With dc voltage control on MSC. Source: [C7].

achieved on the GSC by tuning the power reference according to the wind speed. Considering the mechanical variables (e.g., rotor speed) of wind turbines vary in a slow time scale, they are ignored when studying the small-signal stability issues in this thesis. Thus, a given rotor speed or input power are used for analysis. Besides, the MPPT control algorithm is also ignored, so the speed or power reference is given directly.

As aforementioned, the small-signal impedance model is a powerful tool to analyze the small-signal stability of the converter system. So, impedance modeling of GFL-PMSGs will be introduced in the following sections.

4.1.1 Impedance Modeling of GFL-PMSG

As shown in Fig. 4.1, the MSC and GSC in Type-4 wind generators are connected by a dc-link with a capacitor C_{dc}. Thus, the dc-link voltage V_{dc} plays a key role in modeling the whole system. The influence of the dc-link voltage on modeling is worth being discussed at first. In the pulse width modulation
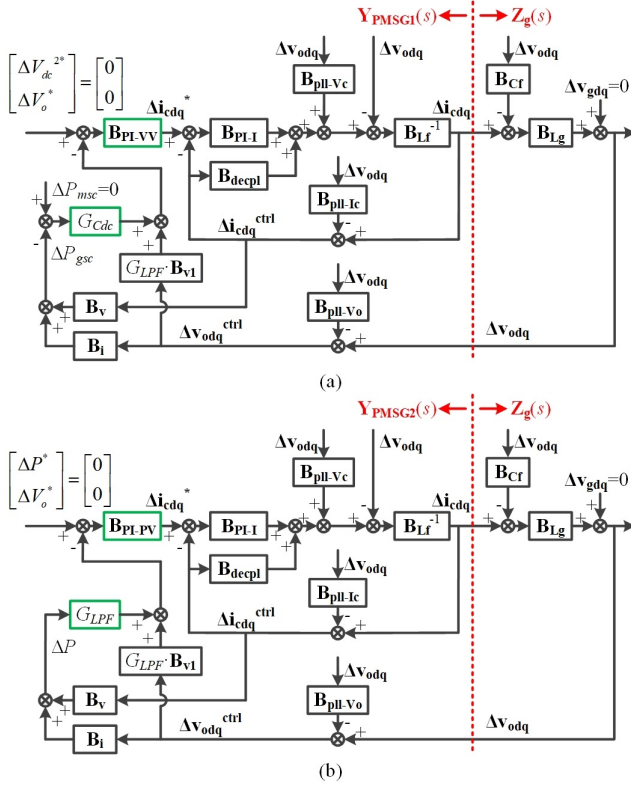
Fig. 4.2: Small-signal d-q impedance models of GFL-PMSGs shown in Fig. 4.1. (a) With dc voltage control on GSC; (b) With dc voltage control on MSC. Source: [C7].

(PWM) block shown in Fig. 4.1, either the measured value or the reference value of dc-link voltage can be used for modulation, but these two ways lead to different results. The relation between the converter output voltage and the dc-link voltage can be derived as (4.1).

$$
v_{c(abc)} = m_{(abc)} \cdot \frac{V_{dc}}{2} =
\begin{cases}
\frac{v^*_{c(abc)}}{V^*_{dc}/2} \cdot \frac{V_{dc}}{2} = \frac{v^*_{c(abc)} \cdot V_{dc}}{V^*_{dc}}, & if: \ m_{(abc)} = \frac{v^*_{c(abc)}}{V^*_{dc}/2} \\
\frac{v^*_{c(abc)}}{V_{dc}/2} \cdot \frac{V_{dc}}{2} = v^*_{c(abc)}, & if: \ m_{(abc)} = \frac{v^*_{c(abc)}}{V_{dc}/2}
\end{cases}
\quad (4.1)
$$

where $m_{(abc)}$ is the three-phase modulation voltage, V_{dc} is the actual/measured value of the dc-link voltage, V^*_{dc} is the reference value of the dc-link voltage, and $v^*_{c(abc)}$ is the reference value of the converter voltage.

As presented in (4.1), when the reference value V^*_{dc} is used for modulation, the converter output voltage $v_{c(abc)}$ is related to dc-link voltage V_{dc}. Differently, when the actual/measured value V_{dc} is used for modulation, the converter output voltage $v_{c(abc)}$ is not related to dc-link voltage V_{dc}. Thus, the measured value of the dc-link voltage is chosen to be used for modulation
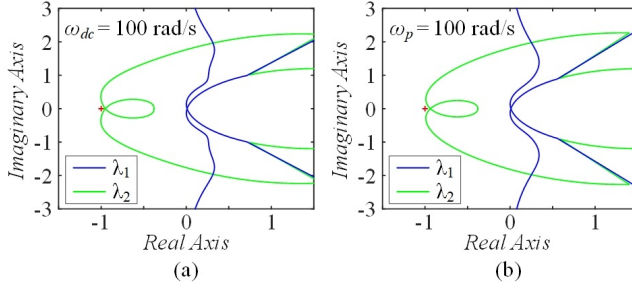
Fig. 4.3: Generalized Nyquist diagrams of impedance models in Fig. 4.2 ($P = 0.8$ p.u., SCR = 1). (a) $\mathbf{Y_{PMSG1}} \cdot \mathbf{Z_g}$ in Fig. 4.2(a); (b) $\mathbf{Y_{PMSG2}} \cdot \mathbf{Z_g}$ in Fig. 4.2(b). Source: [C7].
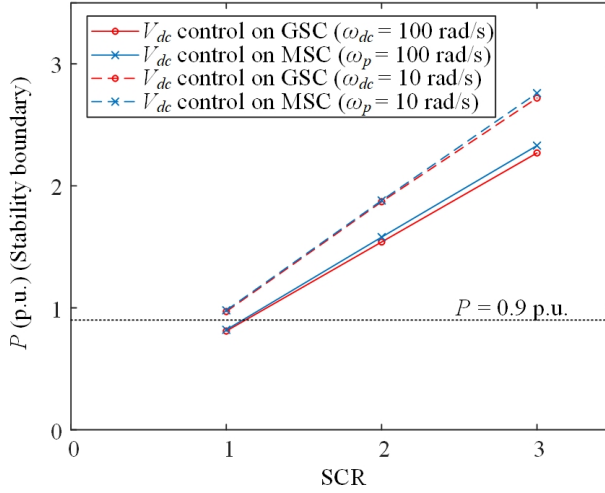
Fig. 4.4: Comparison of small-signal stability boundaries of GFL-PMSGs with grid-side and machine-side dc voltage control schemes (ω_{dc}: bandwidth of dc voltage control loop; ω_p: bandwidth of active power control loop). Source: [C7].

in this thesis, because it can simplify the small-signal model by eliminating the influence of dc-link voltage. The small-signal impedance models of GFL-PMSGs with dc voltage controls on the MSC and GSC are shown in Fig. 4.2.

Notably, the symbol **B** in Fig. 4.2 denotes a 2×2 matrix (See [C7] for detailed expressions). According to Fig. 4.2, the output admittances of GFL-PMSGs with grid-side and machine-side dc voltage control schemes can be deduced as (4.2) and (4.3), respectively.

$$\mathbf{Y_{PMSG1}}(s) = (\mathbf{B_{PI\text{-}I}} - \mathbf{B_{decpl}} + \mathbf{B_{Lf}} - \mathbf{B_{PI\text{-}I}}\mathbf{B_{PI\text{-}VV}}G_{Cdc}\mathbf{B_v})^{-1} \cdot$$
$$[\mathbf{I} - (\mathbf{B_{PI\text{-}I}} - \mathbf{B_{decpl}} - \mathbf{B_{PI\text{-}I}}\mathbf{B_{PI\text{-}VV}}G_{Cdc}\mathbf{B_v}) \cdot \mathbf{B_{pll\text{-}Ic}} - \mathbf{B_{pll\text{-}Vc}} \qquad (4.2)$$
$$+ \mathbf{B_{PI\text{-}I}}\mathbf{B_{PI\text{-}VV}}(G_{LPF}\mathbf{B_{v1}} - G_{Cdc}\mathbf{B_i})(\mathbf{I} - \mathbf{B_{pll\text{-}Vo}})]$$

68

Fig. 4.5: Simulation results of a 30 kW GFL-PMSG with grid-side and machine-side dc voltage control ($\omega_{dc} = \omega_p = 100$ rad/s, SCR = 1). (a) With dc voltage control on GSC and speed control on MSC; (b) With dc voltage control on MSC and power control on GSC. Source: [C7].

$$\mathbf{Y_{PMSG2}}(s) = (\mathbf{B}_{\text{PI-I}} - \mathbf{B}_{\text{decpl}} + \mathbf{B}_{\text{Lf}} + \mathbf{B}_{\text{PI-I}}\mathbf{B}_{\text{PI-PV}}G_{LPF}\mathbf{B}_{\text{v}})^{-1} \cdot$$
$$[\mathbf{I} - (\mathbf{B}_{\text{PI-I}} - \mathbf{B}_{\text{decpl}} + \mathbf{B}_{\text{PI-I}}\mathbf{B}_{\text{PI-PV}}G_{LPF}\mathbf{B}_{\text{v}}) \cdot \mathbf{B}_{\text{pll-Ic}} - \mathbf{B}_{\text{pll-Vc}} \quad (4.3)$$
$$+ \mathbf{B}_{\text{PI-I}}\mathbf{B}_{\text{PI-PV}}(G_{LPF}\mathbf{B}_{\text{v1}} + G_{LPF}\mathbf{B}_{\text{i}})(\mathbf{I} - \mathbf{B}_{\text{pll-Vo}})]$$

Then, the generalized Nyquist diagrams of $\mathbf{Y_{PMSG1}} \cdot \mathbf{Z_g}$ and $\mathbf{Y_{PMSG2}} \cdot \mathbf{Z_g}$ can be plotted based on (4.2) and (4.3), as presented in Fig. 4.3(a) and (b). Fig. 4.3 shows that when ω_{dc} and ω_p are the same, the generalized Nyquist diagrams of two impedance models in Fig. 4.2 are very similar.

Moreover, following the steps in Fig. 2.9, the small-signal stability boundary of the GFL inverter system can be found by changing steady-state operation points gradually. The small-signal stability boundaries of the GFL-PMSG with the machine-side and grid-side and dc voltage control approaches are compared in Fig. 4.4. It shows that when the control parameters of two control approaches are the same, their small-signal stability boundaries are very close to each other. Besides, a lower bandwidth of dc voltage/power control loop is beneficial for enhancing the small-signal stability.

To validate the correctness of above analysis, a 30 kW GFL-PMSG simulation model is built in MATLAB/Simulink. The detailed control and system parameters have been presented in [C7], which are omitted here. Like Fig. 4.4, a higher bandwidth of dc voltage/power control loop (i.e., 100 rad/s) and a lower bandwidth of dc voltage/power control loop (i.e., 10 rad/s) are chosen for analyses.
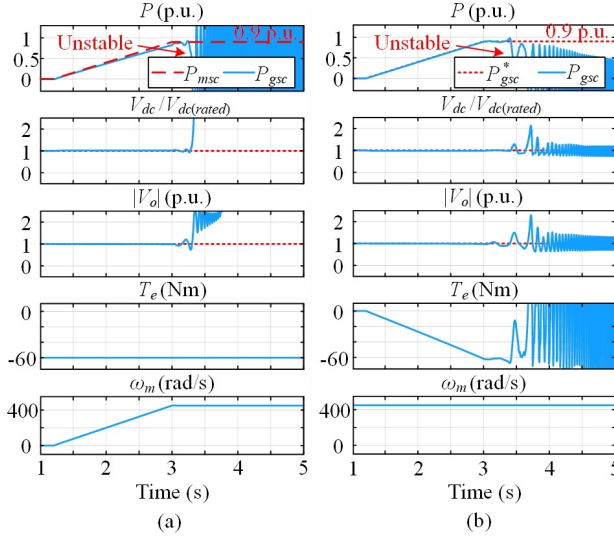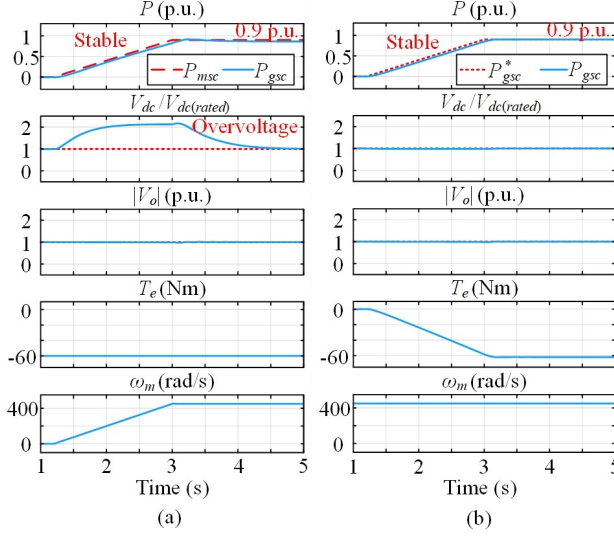
Fig. 4.6: Simulation results of a 30 kW GFL-PMSG with grid-side and machine-side dc voltage control ($\omega_{dc} = \omega_p = 10$ rad/s, SCR = 1). (a) With dc voltage control on GSC and speed control on MSC; (b) With dc voltage control on MSC and power control on GSC. Source: [C7].

The simulation outcomes of the aforementioned two GFL control approaches for PMSGs with a higher bandwidth of dc voltage/power control loop are illustrated in Fig. 4.5, while the outcomes with a lower bandwidth of dc voltage/power control loop are presented in Fig. 4.6. Fig. 4.5 shows that when the active power is increased to 0.9 p.u. in the case of $\omega_p = \omega_{dc} = 100$ rad/s and SCR = 1, both two control approaches become unstable. Reversely, Fig. 4.6 shows that when the active power is raised to 0.9 p.u. in the case of $\omega_p = \omega_{dc} = 10$ rad/s and SCR = 1, both two control approaches are stable. The above simulation outcomes are persistent to the stability analyses in Fig. 4.4.

Furthermore, Fig. 4.6(a) shows an overvoltage issue of the dc-link capacitor. Since a lower bandwidth of dc voltage control loop on the GSC ($\omega_{dc} = 10$ rad/s) is used, the power on the grid side varies more slowly than that on the machine side. So, the short-term energy accumulated on the dc-link capacitor leads to the increasement of the dc voltage, which might result in overvoltage problems. It is risky to hurt dc-link capacitors. So, a higher bandwidth of the dc voltage control loop has the advantage of avoiding the overvoltage issue. However, a lower bandwidth of the dc voltage control loop is beneficial for small-signal stability. Hence, a trade-off between the overvoltage issue and the stability needs to be considered to design the bandwidth of dc voltage control loop. Dissimilarly, it can be observed from Fig. 4.6(b) that there is no overvoltage problems to restrict the design of the power loop bandwidth on the GSC. So, a lower bandwidth of the power loop ($\omega_p = 10$ rad/s) can be used to enhance the small-signal stability. Based on the above analysis, the

70
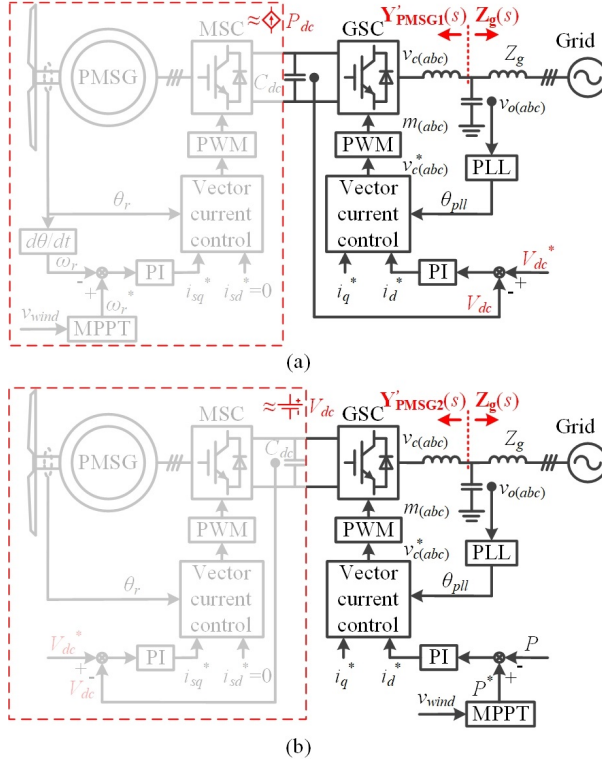
Fig. 4.7: Model reduction of GFL-PMSGs. (a) With dc voltage control on GSC; (b) With dc voltage control on MSC. Source: [C7].

machine-side dc voltage control seems to be better than the grid-side dc voltage control in weak grid cases. Hence, the machine-side dc voltage control for GFL-PMSGs will be used in this thesis.

4.1.2 Impedance Characteristic Analysis for GFL-PMSG

As aforementioned, when the measured value of the dc-link voltage is utilized for modulation in Type-4 wind generation systems, the output voltage of the GSC is not influenced by the dc voltage, which is beneficial for reducing the coupling relationship between the GSC and MSC. Thus, as shown in Fig. 4.7, the machine-side subsystem can be treated to be an ideal voltage or power source from a small-signal perspective.

To demonstrate the correctness of the simplified models in Fig. 4.7, a complete model and a simplified model of the GFL-PMSG are built in MATLAB/Simulink, where the simulation parameters are the same as that in [C7]. The measured admittances $\mathbf{Y}'_{\mathbf{PMSG1}}$ and $\mathbf{Y}'_{\mathbf{PMSG2}}$ by using simplified simulation models with an ideal power/voltage source on the machine side can
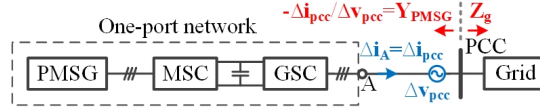
Fig. 4.8: Small-signal admittance measurement method for Type-4 wind generators ($\Delta\mathbf{v_{pcc}}$: injected small-signal voltage perturbation; $\Delta\mathbf{i_{pcc}}$: small-signal current response). Source: [J5].
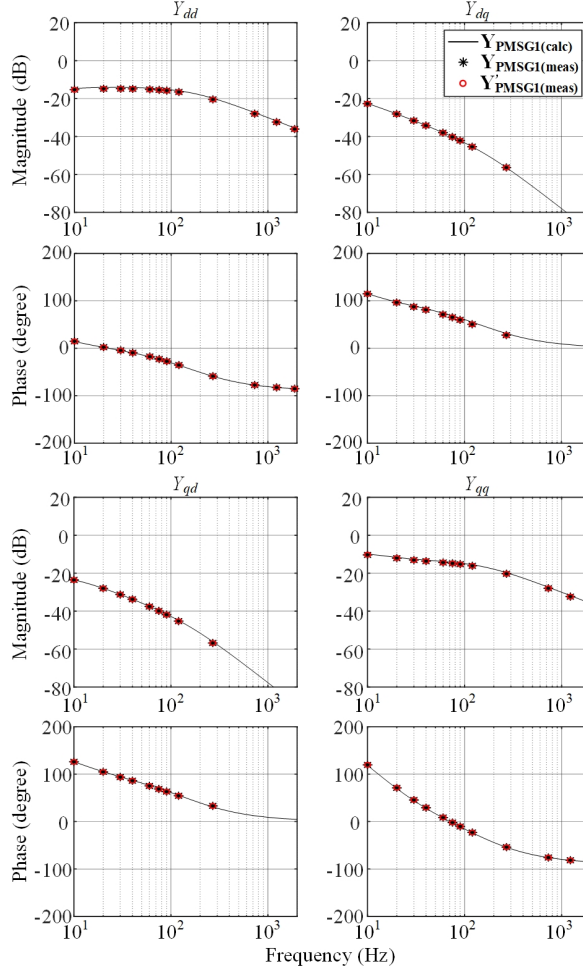
Fig. 4.9: Small-signal d-q admittance measurement results for GFL-PMSGs with grid-side dc voltage control and its simplified model ($\mathbf{Y_{PMSG1(meas)}}$: measured admittance by using complete model; $\mathbf{Y'_{PMSG1(meas)}}$:measured admittance by using simplified model shown in Fig. 4.7(a)).

be compared with the measured admittances $\mathbf{Y_{PMSG1}}$ and $\mathbf{Y_{PMSG2}}$ by using complete simulation models with the MSC plus PMSG to see the difference. Notably, as shown in Fig. 4.8, a typical admittance measurement method by
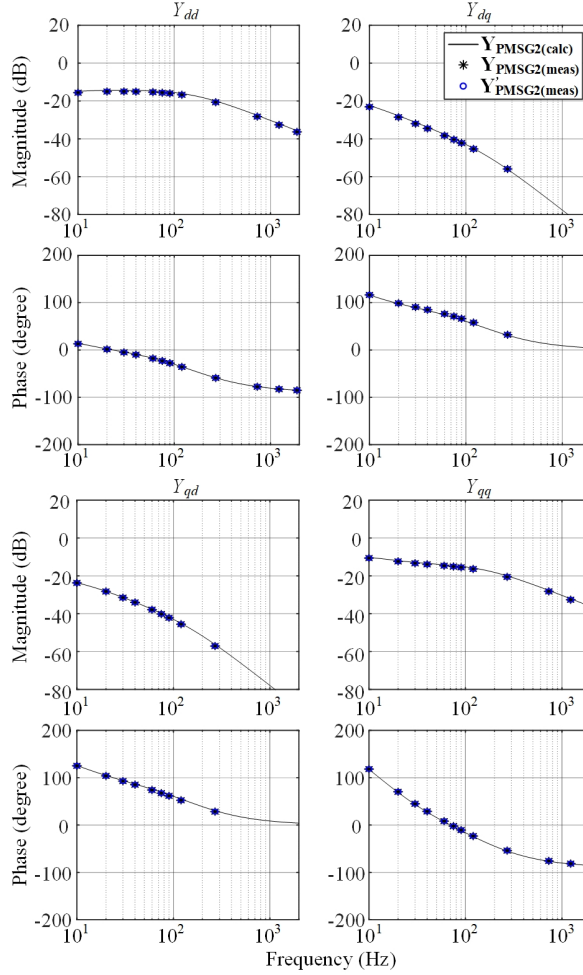
Fig. 4.10: Small-signal d-q admittance measurement results for GFL-PMSGs with machine-side dc voltage control and its simplified model ($\mathbf{Y_{PMSG2(meas)}}$: measured admittance by using complete model; $\mathbf{Y'_{PMSG2(meas)}}$:measured admittance by using simplified model shown in Fig. 4.7(b)).

injecting small-signal voltage disturbances and detecting small-signal current responses introduced in [77] is used to "measure" the admittances.

The small-signal d-q admittance measurement results for GFL-PMSGs with grid-side dc voltage control and its simplified model are shown in Fig. 4.9. It can be seen that both the measured admittances $\mathbf{Y_{PMSG1(meas)}}$ by using the complete model and $\mathbf{Y'_{PMSG1(meas)}}$ by using the simplified model are overlapped with the calculated admittance $\mathbf{Y_{PMSG1(calc)}}$. In addition, the small-signal d-q admittance measurement results for GFL-PMSGs with machine-side dc voltage control and its simplified model are shown in Fig. 4.10.

Fig. 4.11: Two typical GFM control approaches for Type-4 wind power generation system. (a) With dc voltage control on GSC; (b) With dc voltage control on MSC. Source: [J4].

It can be seen that both the measured admittances $\mathbf{Y_{PMSG2(meas)}}$ by using the complete model and $\mathbf{Y'_{PMSG2(meas)}}$ by using the simplified model are over-lapped with the calculated admittance $\mathbf{Y_{PMSG2(calc)}}$. The above admittance measurement results indicate that the ac terminal admittances of GFL-PMSGs are still accurate when the PMSG plus MSC is simplified as an ideal power or voltage source presented in Fig. 4.7. Thus, the simplified models in Fig. 4.7 is able to be utilized to study the small-signal stability of GFL-PMSGs.

4.2 Control and Impedance Modeling of GFM-PMSG

After analyzing GFL-PMSGs in the previous section, this section will move the research focus to GFM-PMSGs. As for the GFM-PMSG, there are two typical GFM control schemes, which are dc voltage control on the MSC and dc voltage control on the GSC [J4]. The GFM-PMSG with the dc voltage control on GSC is presented in Fig. 4.11(a), where the MSC is used to control the rotor
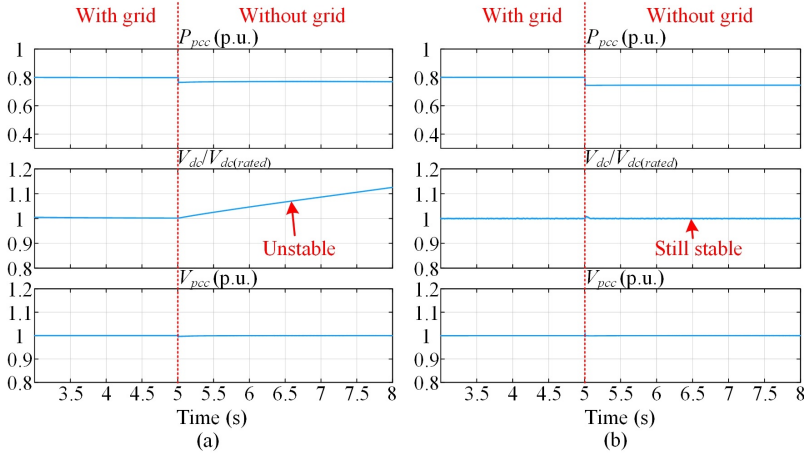
Fig. 4.12: Simulation results of a 30 kW GFM-PMSG by using grid-side and machine-side dc voltage controls in the cases with and without the grid. (a) Dc voltage control on GSC; (b) Dc voltage control on MSC. Source: [J4].

speed of the PMSG. Differently, the GFM-PMSG with the dc voltage control on MSC is presented in Fig. 4.11(b), where the GSC is used to control the output power. Besides, considering the island operation ability is important for GFM wind generators to operate in a 100% inverter-based power system or to operate in an ordinary power system during the blackout event, a local load is added at the PCC in Fig. 4.11 for the island operation test.

The simulation results of a 30 kW GFM-PMSG with dc voltage controls on the MSC and GSC are compared in Fig. 4.12. As presented in Fig. 4.12(a), when the dc voltage is controlled by the GSC, it is not able to be remained as a constant after the grid is removed. This is because the input power (determined by the wind speed) is no more equal to the output power (depending on the load in the islanded case). So, the dc voltage may decrease or increase continuously. Eventually, the GFM-PMSG will be unstable. However, as presented in Fig. 4.12(b), when the dc voltage is controlled by the MSC, it can be kept at the rated value no matter with or without the grid because the input power can be controlled as same as the output power. So, the dc voltage control approach on the MSC will be used in this thesis.

4.2.1 Impedance Modeling of GFM-PMSG

As aforementioned, when the measured dc voltage is used for modulation in the Type-4 wind generators, the output voltage of the GSC is not influenced by the dc-link voltage (the MSC and PMSG either). Thus, the small-signal impedance model of GFM-PMSGs with the dc voltage control on the MSC is presented in Fig. 4.13. Thereafter, $\mathbf{Y_{PMSG}}$ can be derived as (4.4), where $\mathbf{B}$ de-

Fig. 4.13: Small-signal d-q impedance model of GFM-PMSGs with machine-side dc voltage control. Source: [C5].

Fig. 4.14: Model reduction of GFM-PMSGs with machine-side dc voltage control.

notes a 2×2 matrix (See [C4] for detailed expressions). Then, the admittance characteristics of $\mathbf{Y_{PMSG}}$ can be analyzed by using Bode diagrams.

$$
\begin{aligned}
\mathbf{Y_{PMSG}}(s) = & \left\{ \mathbf{B_{PI\text{-}I}} - \mathbf{B_{decpl}} + \mathbf{B_{Lf}} + G_{LPF} \cdot \frac{m_p}{s} \cdot \left[\mathbf{B_{Vc\text{-}v}} + (\mathbf{B_{PI\text{-}I}} \right.\right. \\
& \left. - \mathbf{B_{decpl}}) \cdot \mathbf{B_{Ic\text{-}v}} + \mathbf{B_{PI\text{-}I}} \cdot \mathbf{B_{Lv}}^{-1} \cdot \mathbf{B_{Vo\text{-}v}} \right] \right\}^{-1} \cdot \left\{ \mathbf{I} + \mathbf{B_{PI\text{-}I}} \cdot \mathbf{B_{Lv}}^{-1} \right. \\
& + (\mathbf{B_{Lf}} + \mathbf{B_{PI\text{-}I}} - \mathbf{B_{decpl}}) \cdot \mathbf{B_{Cf}} + G_{LPF} \cdot \frac{m_p}{s} \cdot [\mathbf{B_{Vc\text{-}i}} + (\mathbf{B_{PI\text{-}I}} \\
& \left. - \mathbf{B_{decpl}}) \cdot \mathbf{B_{Ic\text{-}i}} + \mathbf{B_{PI\text{-}I}} \cdot \mathbf{B_{Lv}}^{-1} \cdot \mathbf{B_{Vo\text{-}i}} \right]\}
\end{aligned}
\tag{4.4}
$$

4.2.2 Impedance Characteristic Analysis for GFM-PMSG

Like Fig. 4.7(b), if the output voltage of the GSC is not influenced by the MSC and PMSG in the Type-4 wind generators, the machine-side subsystem

Fig. 4.15: Small-signal d-q admittance measurement results for GFM-PMSGs with machine-side dc voltage control and its simplified model ($\mathbf{Y_{PMSG(meas)}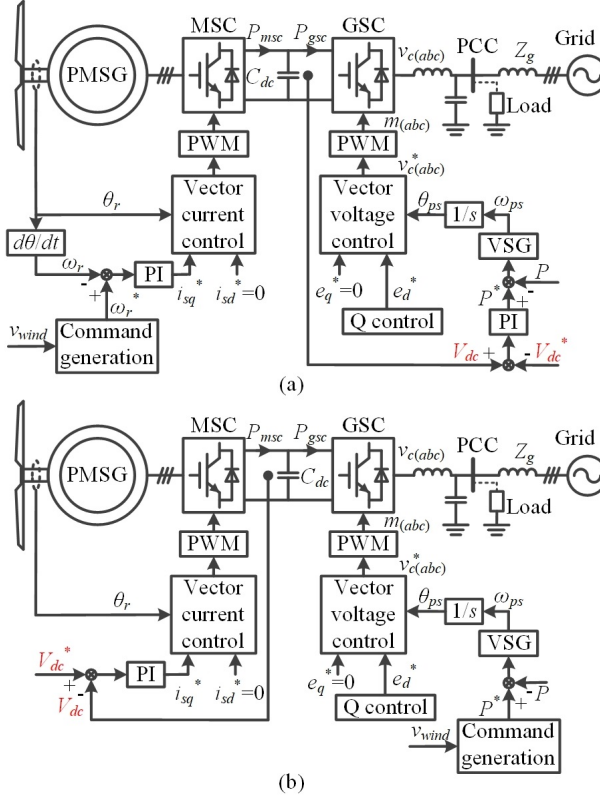}$: measured admittance by using complete model; $\mathbf{Y'_{PMSG(meas)}}$:measured admittance by using simplified model shown in Fig. 4.14).

can be considered as an ideal voltage source. Thus, the simplified system of GFM-PMSGs with machine-side dc voltage control is illustrated in Fig. 4.14.

To validate the correctness of the simplified model in Fig. 4.14, a complete model and a simplified model of the GFM-PMSG are built in MAT-LAB/Simulink, where the simulation parameters are the same as that in [C5]. The measured admittances $\mathbf{Y'_{PMSG}}$ by using simplified simulation model with an ideal voltage source on the machine side can be compared with the measured admittances $\mathbf{Y_{PMSG}}$ by using complete simulation models with MSC plus PMSG to see the difference between two models.
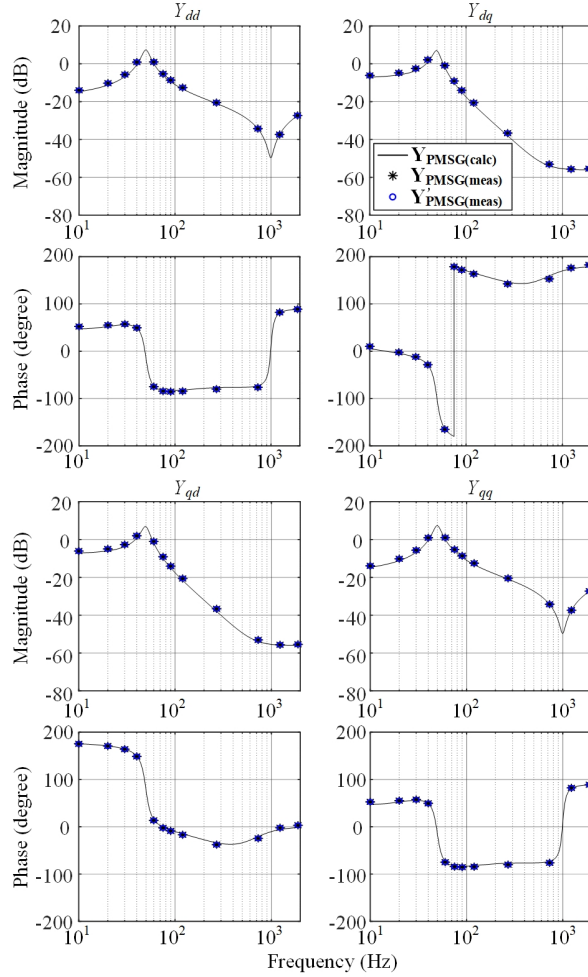
The small-signal d-q admittance measurement results for GFM-PMSGs with machine-side dc-link voltage control and its simplified model are shown in Fig. 4.15. It can be seen that both the measured admittances $\mathbf{Y_{PMSG(meas)}}$ by using the complete model and $\mathbf{Y'_{PMSG(meas)}}$ by using the simplified model are overlapped with the calculated admittance $\mathbf{Y_{PMSG(calc)}}$. These admittance measurement results indicate that the ac terminal admittances of GFM-PMSGs are still accurate when the PMSG plus MSC is simplified as an ideal voltage source presented in Fig. 4.14. Thus, the simplified model in Fig. 4.14 can be used to study the small-signal stability of GFM-PMSGs.

Additionally, as illustrated in Fig. 4.15, both the phases of Y_{dd} and Y_{qq} are within -90 $\sim$ 90 degrees, which means that there are no negative resistance characteristics on Y_{dd} and Y_{qq}. Thus, the small-signal stability of the GFM-PMSG designed in this thesis should be quite good.

4.3 Summary

This chapter has provided a systematic discussion of small-signal impedance modeling of GFL and GFM PMSGs. At first, GFL-PMSGs with dc voltage controls on the MSC and GSC are compared. It is found that the machine-side dc voltage control has better performance than the grid-side dc voltage control under weak grid conditions since a lower bandwidth of the active power control loop can be used to enhance the small-signal stability. Then, the admittance characteristics of GFL-PMSGs with complete models and simplified models are compared. It is found that the ac terminal admittance characteristics of GFL-PMSGs are still accurate when the machine-side subsystem is simplified to be an ideal power/voltage source.

Afterwards, GFM-PMSGs with dc voltage controls on the MSC and GSC are compared. It is found that the island operation might be a challenge for the GFM-PMSG with the grid-side dc voltage control, because the dc voltage is hard to be maintained to be a constant in the islanded case without the grid connection. Differently, the GFM-PMSG with the machine-side dc voltage control works well in both grid-connected and grid-disconnected cases. So, the GFM-PMSGs with dc voltage control on the MSC is chosen to study further. By comparing the admittance characteristics of GFM-PMSGs with complete models and simplified models, it is found that the ac terminal admittance characteristics of GFM-PMSGs are still accurate when the machine-side subsystem is simplified to be an ideal voltage source. Therefore, the simplified models are beneficial for analyzing the small-signal stability of the power system including plenty of Type-4 wind generators, which can shorten the simulation time.

Chapter 5

Control and Impedance Modeling of Grid-Connected DFIG

In the previous chapter, the control and impedance modeling of Type-4 wind generation systems have been discussed. This chapter will move the research focus to Type-3 wind generation systems, which is another type of wind generation solution with the DFIG and partial-scale converters. In this chapter, the control and small-signal impedance modeling approaches of GFL and GFM Type-3 wind generation systems will be introduced. Finally, the calculated and measured impedances in the frequency domain will be compared to demonstrate the correctness of the developed modeling approach.

5.1 Control and Impedance Modeling of GFL-DFIG

Currently, Type-3 wind generators with partial-scale power converters plus DFIGs and Type-4 wind generators with full-scale power converters plus PMSGs have been widely used in the field of wind generation. To make sure wind generators can operate stably in the power system, small-signal modeling and stability analysis for them are very important. For the Type-4 wind generation system, the PMSG and the back-to-back converter are connected in series (i.e., linear connection), so its impedance model can be easily derived according to the output voltage and current of the GSC. Differently, for the Type-3 wind generation system, the DFIG and the back-to-back converter are connected on both the rotor side and the stator side (i.e., circular connection), so the DFIG stator currents and the GSC output currents are influenced by each other, which increases the difficulty to derive its full-order

79
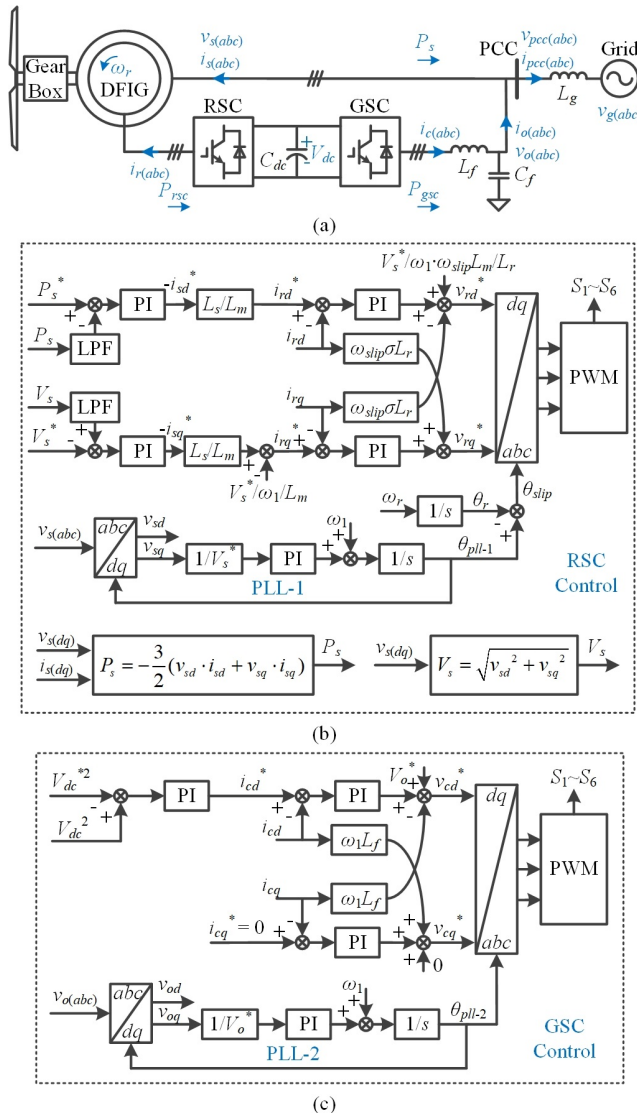
Fig. 5.1: Typical GFL control scheme for Type-3 wind generation systems. (a) Physical configuration of Type-3 wind generation systems; (b) GFL control scheme on the RSC; (c) PLL-based dc voltage control scheme on the GSC. Source: [J5].

impedance model. A conventional modeling method is ignoring the dc-link coupling by assuming that the dc voltage is constant, so the RSC and the GSC can be modeled separately [78–82]. However, the rationality of this assumption has not been demonstrated sufficiently. In this chapter, a novel decoupled impedance modeling method will be introduced to build the full-order impedance model of the DFIG system.

A typical GFL control scheme for Type-3 wind generation systems are shown in Fig. 5.1, where the GSC is responsible for controlling the dc-link voltage, and the RSC is used to control the output power of the DFIG. Fig. 5.1(a) presents the physical configuration of the Type-3 wind generation system, where a DFIG and a back-to-back converter are connected to the grid at the PCC. Notably, to simplify the analysis, the transformer of the Type-3 wind generator at the PCC is ignored. In Fig. 5.1(a), C_{dc} is the dc capacitor. C_f and L_f are the filter capacitors and inductors. L_g represents the grid impedance, where the resistance is ignored. Considering the rotor speed ω_r changes in a slower time scale compared to the fundamental frequency of the ac voltages and currents, the rotor speed ω_r is supposed to be constant.

Moreover, Fig. 5.1(b) shows the stator-voltage oriented control (SVOC) scheme on the RSC. It includes outer power control loops, inner current control loops, and a PLL. The active power is controlled on the d-axis, while the reactive power is controlled on the q-axis (Notably, the grid voltage needs to be supported in weak grid cases, so the stator voltage magnitude V_s is used for control rather than the reactive power Q_s). Besides, ω_1 represents the fundamental angular frequency of the stator voltage, and ω_{slip} represents the slip angular frequency, which is equal to ($\omega_1 - \omega_r$). Fig. 5.1(c) shows the PLL-based dc voltage control approach on the GSC. It includes an outer dc voltage control loop, inner current control loops, and a PLL. To differentiate two PLLs on the RSC and GSC, the PLL on the RSC is named "PLL-1", while the PLL on the GSC is name "PLL-2".

To study the stability of the Type-3 wind generation system, the small-signal impedance model is a commonly used approach. It will be introduced in the following sections.

5.1.1 Impedance Modeling of GFL-DFIG

Considering that the whole Type-3 wind generation system is relatively large, it can be divided into two subsystems for analysis (i.e., a rotor-side subsystem and a grid-side subsystem). Thus, small-signal impedance models of the rotor-side subsystem and the grid-side subsystem are introduced in this section initially.

A. Modeling of DFIG in d-q frame

Same as [78], the stator/rotor voltage and flux equations of the DFIG in the d-q frame are given by (5.1)-(5.4).

$$\begin{cases} v_{sd} = R_s i_{sd} + \frac{d\psi_{sd}}{dt} - \omega_1 \psi_{sq} \\ v_{sq} = R_s i_{sq} + \frac{d\psi_{sq}}{dt} + \omega_1 \psi_{sd} \end{cases} \tag{5.1}$$

$$\begin{cases} v_{rd} = R_r i_{rd} + \frac{d\psi_{rd}}{dt} - \omega_{slip} \psi_{rq} \\ v_{rq} = R_r i_{rq} + \frac{d\psi_{rq}}{dt} + \omega_{slip} \psi_{rd} \end{cases} \tag{5.2}$$

$$\begin{cases} \psi_{sd} = L_s i_{sd} + L_m i_{rd} \\ \psi_{sq} = L_s i_{sq} + L_m i_{rq} \end{cases} \tag{5.3}$$

$$\begin{cases} \psi_{rd} = L_r i_{rd} + L_m i_{sd} \\ \psi_{rq} = L_r i_{rq} + L_m i_{sq} \end{cases} \tag{5.4}$$

where L_s and R_s are the stator inductance and resistance, L_r and R_r are the rotor inductance and resistance, and L_m is the mutual inductance.

Substituting (5.3) and (5.4) into (5.2), the expression of the voltage and flux can be derived as (5.5).

$$\begin{cases} v_{rd} - \frac{L_m}{L_s}\frac{d\psi_{sd}}{dt} + \frac{L_m}{L_s}\omega_{slip}\psi_{sq} = R_r i_{rd} + \sigma L_r \frac{di_{rd}}{dt} - \omega_{slip}\sigma L_r i_{rq} \\ v_{rq} - \frac{L_m}{L_s}\frac{d\psi_{sq}}{dt} - \frac{L_m}{L_s}\omega_{slip}\psi_{sd} = R_r i_{rq} + \sigma L_r \frac{di_{rq}}{dt} + \omega_{slip}\sigma L_r i_{rd} \end{cases} \tag{5.5}$$

where $\sigma = (L_s L_r - L_m^2)/(L_s L_r)$.

Considering the stator resistance R_s in (5.1) is very small, it can be ignored in order to simplify the calculations. Thus, when (5.1), (5.3), and (5.5) are transformed into frequency-domain expressions by using Laplace transform, their small-signal expressions can be deduced as:

$$\begin{bmatrix} \Delta i_{sd} \\ \Delta i_{sq} \end{bmatrix} = \begin{bmatrix} sL_s & -\omega_1 L_s \\ \omega_1 L_s & sL_s \end{bmatrix}^{-1} \cdot \begin{bmatrix} \Delta v_{sd} \\ \Delta v_{sq} \end{bmatrix} - \frac{L_m}{L_s}\begin{bmatrix} \Delta i_{rd} \\ \Delta i_{rq} \end{bmatrix} \tag{5.6}$$

$$\begin{bmatrix} \Delta i_{rd} \\ \Delta i_{rq} \end{bmatrix} = \begin{bmatrix} R_r + s\sigma L_r & -\omega_{slip}\sigma L_r \\ \omega_{slip}\sigma L_r & R_r + s\sigma L_r \end{bmatrix}^{-1} \cdot \left(\begin{bmatrix} \Delta v_{rd} \\ \Delta v_{rq} \end{bmatrix} - \right.$$
$$\left. \begin{bmatrix} sL_m & -\omega_{slip}L_m \\ \omega_{slip}L_m & sL_m \end{bmatrix} \cdot \begin{bmatrix} sL_s & -\omega_1 L_s \\ \omega_1 L_s & sL_s \end{bmatrix}^{-1} \cdot \begin{bmatrix} \Delta v_{sd} \\ \Delta v_{sq} \end{bmatrix} \right) \tag{5.7}$$

where Δ represents small-signal perturbations of variables.

According to (5.6) and (5.7), the small-signal impedance model of the DFIG is presented in the blue area of Fig. 5.2, where $\mathbf{B}_{Lr}$, $\mathbf{B}_{Lm}$, and $\mathbf{B}_{Ls}$ represent the 2×2 matrixes in (5.7), respectively.

B. Modeling of RSC in d-q frame

According to the RSC control scheme presented in Fig. 5.1(b), the frequency-domain small-signal impedance model of the RSC is presented in Fig. 5.2. Notably, $\mathbf{B}_{PI-PV}$, $\mathbf{B}_{LPF}$, $\mathbf{B}_{v-1}$, $\mathbf{B}_{i-1}$, $\mathbf{B}_{PI-I-1}$, $\mathbf{B}_{decpl-1}$, $\mathbf{B}_{pll-1-Vr}$, and $\mathbf{B}_{pll-1-Ir}$ represent 2×2 matrixes (See [J5] for detailed expressions). Besides, the superscript 'ctrl' represents the control d-q frame. Since the DFIG is controlled by the RSC, the model of the DFIG is included in Fig. 5.2.

C. Modeling of GSC in d-q frame

Similarly, according to the GSC control approach presented in Fig. 5.1(c), the small-signal model of the GSC is presented in Fig. 5.3. Notably, $\mathbf{B}_{PI-Vdc}$,
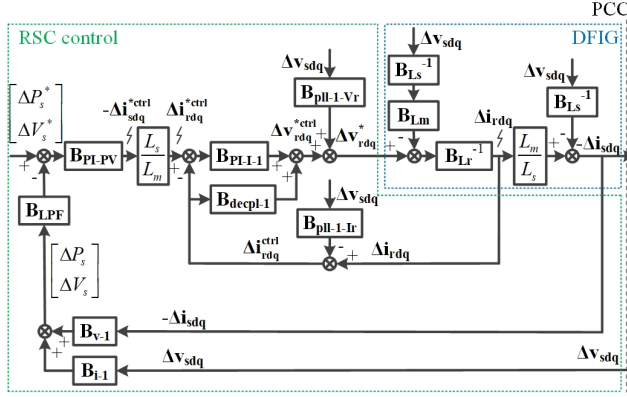
Fig. 5.2: Small-signal d-q impedance model of RSC in GFL-DFIG system. Source: [J5].
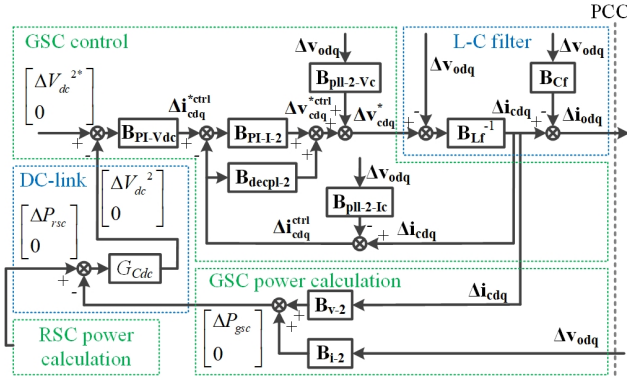
Fig. 5.3: Small-signal d-q impedance model of GSC in GFL-DFIG system. Source: [J5].

$\mathbf{B}_{\text{v-2}}$, $\mathbf{B}_{\text{i-2}}$, $\mathbf{B}_{\text{PI-I-2}}$, $\mathbf{B}_{\text{decpl-2}}$, $\mathbf{B}_{\text{pll-2-Vc}}$, $\mathbf{B}_{\text{pll-2-Ic}}$, $\mathbf{B}_{\text{Lf}}$, and $\mathbf{B}_{\text{Cf}}$ represent 2×2 matrixes (See [J5] for detailed expressions). Because the dc voltage is controlled by the GSC, the model of the dc capacitor is contained in Fig. 5.3.

5.1.2 Proposed Two-Port Network Modeling Method

After establishing the small-signal impedance models of the rotor-side and the grid-side subsystems, the ac terminal impedance of the whole DFIG system needs to be derived. Considering there are both dc-side and ac-side couplings, it is difficult to derive the terminal impedance/admittance of Type-3 wind generators directly. To address this difficulty, a decoupled impedance modeling method will be introduced in this section.

A. Derivation of total admittance of DFIG system

Fig. 5.4 shows the ac terminal small-signal admittance calculation or mea-
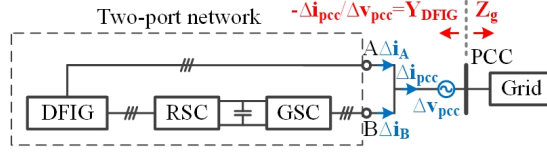
Fig. 5.4: Small-signal admittance measurement method for Type-3 wind generators ($\Delta\mathbf{v_{pcc}}$: injected small-signal voltage perturbation; $\Delta\mathbf{i_{pcc}}$: small-signal current response). Source: [J5].

surement method of Type-3 wind generators, where the total terminal admittance of the DFIG system is given by (5.8).

$$\mathbf{Y_{DFIG}}(s) = \frac{-\Delta\mathbf{i_{pcc}}(s)}{\Delta\mathbf{v_{pcc}}(s)} = \frac{-[\Delta\mathbf{i_A}(s) + \Delta\mathbf{i_B}(s)]}{\Delta\mathbf{v_{pcc}}(s)} \tag{5.8}$$

It can be seen from Fig. 5.4 that both the stator side of the DFIG and the grid side of the GSC are connected at the PCC, so the whole DFIG system can be treated as a two-port network. The DFIG stator current at port A is represented by $\mathbf{i_A}$, and the GSC output current at port B is represented by $\mathbf{i_B}$. Obviously, $\mathbf{i_A}$ and $\mathbf{i_B}$ have interactive couplings. Due to the coupling, the terminal admittance of the DFIG system cannot be calculated as simply as that of the PMSG system. To describe the coupling between port A and port B, a 2×2 matrix can be used. Namely, from the two-port network point of view, the relationship between voltages and currents at the two ports can be described by a 2×2 admittance matrix, as expressed in (5.9).

$$\begin{bmatrix} -\Delta\mathbf{i_A}(s) \\ -\Delta\mathbf{i_B}(s) \end{bmatrix} = \begin{bmatrix} \mathbf{Y_{AA}}(s) & \mathbf{Y_{AB}}(s) \\ \mathbf{Y_{BA}}(s) & \mathbf{Y_{BB}}(s) \end{bmatrix} \cdot \begin{bmatrix} \Delta\mathbf{v_A}(s) \\ \Delta\mathbf{v_B}(s) \end{bmatrix} \tag{5.9}$$

Substituting (5.9) into (5.8), the total terminal admittance of the DFIG system can be deduced by (5.10), which is equal to the sum of four admittance components. Thus, as long as the four admittance components can be calculated, the total terminal admittance $\mathbf{Y_{DFIG}}$ can be obtained accordingly.

$$\begin{aligned}
\mathbf{Y_{DFIG}}(s) &= \frac{-\Delta\mathbf{i_{pcc}}(s)}{\Delta\mathbf{v_{pcc}}(s)} = \frac{-\Delta\mathbf{i_A}(s) - \Delta\mathbf{i_B}(s)}{\Delta\mathbf{v_{pcc}}(s)} \\
&= \frac{[\mathbf{Y_{AA}}\Delta\mathbf{v_A}(s) + \mathbf{Y_{AB}}\Delta\mathbf{v_B}(s)] + [\mathbf{Y_{BA}}\Delta\mathbf{v_A}(s) + \mathbf{Y_{BB}}\Delta\mathbf{v_B}(s)]}{\Delta\mathbf{v_{pcc}}(s)} \\
&= \mathbf{Y_{AA}}(s) + \mathbf{Y_{AB}}(s) + \mathbf{Y_{BA}}(s) + \mathbf{Y_{BB}}(s)
\end{aligned} \tag{5.10}$$

In order to calculate or measure the four admittance components $\mathbf{Y_{AA}}$, $\mathbf{Y_{AB}}$, $\mathbf{Y_{BA}}$, and $\mathbf{Y_{BB}}$, a two-port-network-based decoupled impedance modeling method is illustrated in Fig. 5.5. The key idea of the proposed method is to decouple the ac-side connection of the DFIG system. Namely, port A and port B are connected to two grids with the same parameters, respectively. Thus, each admittance component can be calculated or measured independently. It is worth mentioning that as long as the two grid voltages at the PCC
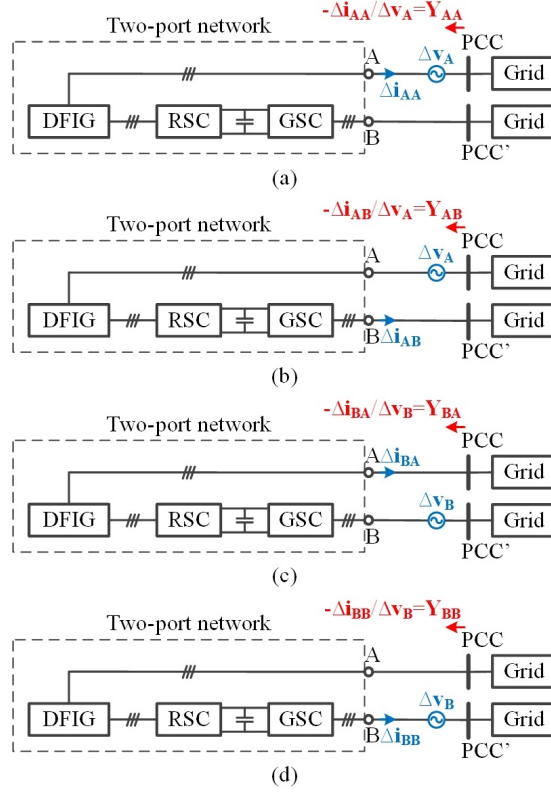
Fig. 5.5: Proposed two-port-network-based decoupled impedance modeling method for Type-3 wind generators. (a) Modeling from port A to port A; (b) Modeling from port A to port B; (c) Modeling from port B to port A; (d) Modeling from port B to port B. Source: [J5].

and PCC′ are the same, the modified DFIG system in Fig. 5.5 is equivalent to the normal DFIG system in Fig. 5.4. The detailed calculation process of the four admittance components will be introduced as follows.

B. Admittance calculation from port A to port A in d-q frame

As presented in Fig. 5.5(a), when injecting a small-signal voltage perturbation $\Delta\mathbf{v_A}$ into the two-port network from port A, there is a current response $\Delta\mathbf{i_{AA}}$ at port A. So, the admittance $\mathbf{Y_{AA}}$ can be expressed as (5.11).

$$\mathbf{Y_{AA}^{dq}}(s) = \frac{-\Delta\mathbf{i_{AA}^{dq}}(s)}{\Delta\mathbf{v_A^{dq}}(s)} = \frac{\Delta\mathbf{i_{sdq}}(s)}{\Delta\mathbf{v_{sdq}}(s)} \tag{5.11}$$

where $\Delta\mathbf{i_{sdq}}$ and $\Delta\mathbf{v_{sdq}}$ are the stator current and voltage of the DFIG.

Then, according to (5.11) and Fig. 5.2, $\mathbf{Y_{AA}}$ can be calculated, which is given by (5.12).

$$\mathbf{Y_{AA}^{dq}}(s) = [\frac{L_s}{L_m}(\mathbf{B_{PI\text{-}I\text{-}1}} - \mathbf{B_{decpl\text{-}1}} + \mathbf{B_{Lr}} + \mathbf{B_{PI\text{-}I\text{-}1}}\mathbf{B_{PI\text{-}PV}}\mathbf{B_{LPF}}\mathbf{B_{v\text{-}1}})]^{-1}$$

$$\cdot [\mathbf{B_{Lm}}\mathbf{B_{Ls}}^{-1} - (\mathbf{B_{PI\text{-}I\text{-}1}} - \mathbf{B_{decpl\text{-}1}}) \cdot \mathbf{B_{pll\text{-}1\text{-}Ir}} - \mathbf{B_{pll\text{-}1\text{-}Vr}} + \frac{L_s}{L_m}(\mathbf{B_{PI\text{-}I\text{-}1}} \quad (5.12)$$

$$- \mathbf{B_{decpl\text{-}1}} + \mathbf{B_{Lr}}) \cdot \mathbf{B_{Ls}}^{-1} + \frac{L_s}{L_m}(\mathbf{B_{PI\text{-}I\text{-}1}}\mathbf{B_{PI\text{-}PV}}\mathbf{B_{LPF}}\mathbf{B_{i\text{-}1}})]$$

C. Admittance calculation from port A to port B in d-q frame

As presented in Fig. 5.5(b), when injecting a small-signal voltage perturbation $\Delta\mathbf{v_A}$ into the two-port network from port A, there is a current response $\Delta\mathbf{i_{AB}}$ at port B. So, the admittance $\mathbf{Y_{AB}}$ can be expressed as (5.13).

$$\mathbf{Y_{AB}^{dq}}(s) = \frac{-\Delta\mathbf{i_{AB}^{dq}}(s)}{\Delta\mathbf{v_A^{dq}}(s)} = \frac{-\Delta\mathbf{i_{odq}}(s)}{\Delta\mathbf{v_{sdq}}(s)} \qquad (5.13)$$

where $\Delta\mathbf{i_{odq}}$ is the output current of the GSC and $\Delta\mathbf{v_{sdq}}$ is the stator voltage of the DFIG.

Taking the small-signal voltage $\Delta\mathbf{v_{odq}}$ in Fig. 5.3 to be zero, the transfer function from ΔP_{rsc} to $\Delta\mathbf{i_{odq}}$ can be deduced as:

$$\Delta\mathbf{i_{odq}}(s) = -(\mathbf{B_{Lf}} + \mathbf{B_{PI\text{-}I\text{-}2}} - \mathbf{B_{decpl\text{-}2}} - \mathbf{B_{PI\text{-}I\text{-}2}}\mathbf{B_{PI\text{-}Vdc}}G_{Cdc}\mathbf{B_{v\text{-}2}})^{-1}$$

$$\cdot (\mathbf{B_{PI\text{-}I\text{-}2}}\mathbf{B_{PI\text{-}Vdc}}G_{Cdc}) \cdot \begin{bmatrix} \Delta P_{rsc} \\ 0 \end{bmatrix} \qquad (5.14)$$

Since the output power of the RSC on the ac side is the same as the output power of the DFIG on the rotor side, the small-signal expression of the power ΔP_{rsc} is provided by (5.15).

$$\begin{bmatrix} \Delta P_{rsc} \\ 0 \end{bmatrix} = -\frac{3}{2} \cdot \begin{bmatrix} i_{rd0} & i_{rq0} \\ 0 & 0 \end{bmatrix} \cdot \begin{bmatrix} \Delta v_{rd} \\ \Delta v_{rq} \end{bmatrix} - \frac{3}{2} \cdot \begin{bmatrix} v_{rd0} & v_{rq0} \\ 0 & 0 \end{bmatrix} \cdot \begin{bmatrix} \Delta i_{rd} \\ \Delta i_{rq} \end{bmatrix}$$

$$(5.15)$$

where the subscript '0' represents the steady-state operation points.

Substituting (5.1), (5.3), and (5.5) into (5.15), the RSC output power ΔP_{rsc} can be deduced as (5.16).

$$\begin{bmatrix} \Delta P_{rsc} \\ 0 \end{bmatrix} = -\frac{3}{2} \cdot \left\{ \frac{(L_m^2 - L_sL_r)s - 2R_rL_s}{L_m} \cdot \begin{bmatrix} i_{rd0} & i_{rq0} \\ 0 & 0 \end{bmatrix} - \frac{\omega_{slip}}{\omega_1} \right.$$

$$\cdot \begin{bmatrix} v_{sd0} & v_{sq0} \\ 0 & 0 \end{bmatrix} \right\} \cdot \Delta\mathbf{i_{sdq}} - \frac{3}{2} \cdot \left\{ \frac{L_rs + 2R_r}{L_m} \cdot \begin{bmatrix} i_{rd0} & i_{rq0} \\ 0 & 0 \end{bmatrix} + \omega_{slip} \right. \qquad (5.16)$$

$$\left. \cdot \begin{bmatrix} -i_{sq0} & i_{sd0} \\ 0 & 0 \end{bmatrix} \right\} \cdot \begin{bmatrix} s & -\omega_1 \\ \omega_1 & s \end{bmatrix}^{-1} \cdot \Delta\mathbf{v_{sdq}}$$

According to (5.11), $\Delta\mathbf{i_{sdq}}$ can be expressed by "$\mathbf{Y_{AA}} \cdot \Delta\mathbf{v_{sdq}}$". Thus, (5.16) can be rewriten as (5.17).

86

$$
\begin{bmatrix} \Delta P_{rsc} \\ 0 \end{bmatrix} = -\frac{3}{2} \cdot \left\{ \frac{(L_m^2 - L_s L_r)s - 2R_r L_s}{L_m} \cdot \begin{bmatrix} i_{rd0} & i_{rq0} \\ 0 & 0 \end{bmatrix} - \frac{\omega_{slip}}{\omega_1} \right.
$$

$$
\left. \cdot \begin{bmatrix} v_{sd0} & v_{sq0} \\ 0 & 0 \end{bmatrix} \right\} \cdot \mathbf{Y^{dq}_{AA}}(s) \cdot \Delta \mathbf{v_{sdq}} - \frac{3}{2} \cdot \left\{ \frac{L_r s + 2R_r}{L_m} \cdot \begin{bmatrix} i_{rd0} & i_{rq0} \\ 0 & 0 \end{bmatrix} \right. \tag{5.17}
$$

$$
+ \omega_{slip} \cdot \begin{bmatrix} -i_{sq0} & i_{sd0} \\ 0 & 0 \end{bmatrix} \right\} \cdot \begin{bmatrix} s & -\omega_1 \\ \omega_1 & s \end{bmatrix}^{-1} \cdot \Delta \mathbf{v_{sdq}}
$$

Then, substituting (5.14) and (5.17) into (5.13), the admittance $\mathbf{Y_{AB}}$ can be calculated as (5.18).

$$
\mathbf{Y^{dq}_{AB}}(s) = -\frac{3}{2} \cdot (\mathbf{B}_{Lf} + \mathbf{B}_{PI\text{-}I\text{-}2} - \mathbf{B}_{decpl\text{-}2} - \mathbf{B}_{PI\text{-}I\text{-}2}\mathbf{B}_{PI\text{-}Vdc}G_{Cdc}\mathbf{B}_{v\text{-}2})^{-1}
$$

$$
\cdot (\mathbf{B}_{PI\text{-}I\text{-}2}\mathbf{B}_{PI\text{-}Vdc}G_{Cdc}) \cdot \left\{ \left[\frac{(L_m^2 - L_s L_r)s - 2R_r L_s}{L_m} \cdot \begin{bmatrix} i_{rd0} & i_{rq0} \\ 0 & 0 \end{bmatrix} \right. \right.
$$

$$
\left. - \frac{\omega_{slip}}{\omega_1} \cdot \begin{bmatrix} v_{sd0} & v_{sq0} \\ 0 & 0 \end{bmatrix} \right] \cdot \mathbf{Y^{dq}_{AA}}(s) + \left[\frac{L_r s + 2R_r}{L_m} \cdot \begin{bmatrix} i_{rd0} & i_{rq0} \\ 0 & 0 \end{bmatrix} \right. \tag{5.18}
$$

$$
\left. \left. + \omega_{slip} \cdot \begin{bmatrix} -i_{sq0} & i_{sd0} \\ 0 & 0 \end{bmatrix} \right] \cdot \begin{bmatrix} s & -\omega_1 \\ \omega_1 & s \end{bmatrix}^{-1} \right\}
$$

D. Admittance calculation from port B to port A in d-q frame

As presented in Fig. 5.5(c), when injecting a small-signal voltage perturbation $\Delta \mathbf{v_B}$ into the two-port network from port B, there is a current response $\Delta \mathbf{i_{BA}}$ at port A. So, the admittance $\mathbf{Y_{BA}}$ can be expressed as:

$$
\mathbf{Y^{dq}_{BA}}(s) = \frac{-\Delta \mathbf{i^{dq}_{BA}}(s)}{\Delta \mathbf{v^{dq}_{B}}(s)} = \frac{\Delta \mathbf{i_{sdq}}(s)}{\Delta \mathbf{v_{odq}}(s)} \tag{5.19}
$$

where $\Delta \mathbf{i_{sdq}}$ is the stator current of the DFIG and $\Delta \mathbf{v_{odq}}$ is the output voltage of the GSC.

Notably, when the measured dc voltage is used for the voltage modulation on the RSC, the output voltage of the RSC is independent from the dc voltage (A detailed mathematical explanation has been provided in Section 4.1.1). Thus, the injected small-signal voltage perturbation at port B is only able to be transferred to the dc-link, while it cannot be further transferred to port A. Therefore, the small-signal current response $\Delta \mathbf{i_{BA}}$ is equal to zero theoretically. The admittance $\mathbf{Y_{BA}}$ can be derived as:

$$
\mathbf{Y^{dq}_{BA}}(s) = \frac{\mathbf{0}}{\Delta \mathbf{v^{dq}_{B}}(s)} = \mathbf{0} \tag{5.20}
$$

E. Admittance calculation from port B to port B in d-q frame

As presented in Fig. 5.5(d), when injecting a small-signal voltage perturbation $\Delta \mathbf{v_B}$ into the two-port network from port B, there is a current response $\Delta \mathbf{i_{BB}}$ at port B. So, the admittance $\mathbf{Y_{BB}}$ can be expressed as (5.21).

Table 5.1: Parameters of DFIG and RSC.

Parameters	Values
Rated active power, P_{N1}	30 kW
Rated phase voltage (peak value), V_{N1}	311 V
Fundamental angular frequency, ω_1	$2\pi \cdot 50$ rad/s
Rotor angular speed, ω_r	$2\pi \cdot 60$ rad/s
Pole pairs, n_p	2
Stator inductance, L_s	82.7 mH
Rotor inductance, L_r	84.5 mH
Mutual inductance, L_m	79.3 mH
Stator resistance, R_s	0.44 mΩ
Rotor resistance, R_r	0.64 mΩ
Designed bandwidth of current loop, ω_{i1}	2000 rad/s
Designed bandwidth of PLL-1, ω_{pll-1}	250 rad/s

Table 5.2: Parameters of GSC.

Parameters	Values
Rated active power, P_{N2}	10 kW
Rated phase voltage (peak value), V_{N2}	311 V
Rated dc voltage, V_{dc}	700 V
Dc capacitance, C_{dc}	500 μF
Filter inductance, L_f	6.9 mH
Filter resistance, R_f	69 mΩ
Filter capacitance, C_f	5 μF
Designed bandwidth of current loop, ω_{i2}	2000 rad/s
Designed bandwidth of PLL-2, ω_{pll-2}	250 rad/s
Designed bandwidth of dc voltage loop, ω_{vdc}	100 rad/s

$$\mathbf{Y}_{\mathbf{BB}}^{\mathbf{dq}}(s) = \frac{-\Delta \mathbf{i}_{\mathbf{BB}}^{\mathbf{dq}}(s)}{\Delta \mathbf{v}_{\mathbf{B}}^{\mathbf{dq}}(s)} = \frac{-\Delta \mathbf{i}_{\mathbf{odq}}(s)}{\Delta \mathbf{v}_{\mathbf{odq}}(s)} \tag{5.21}$$

where $\Delta \mathbf{i}_{\mathbf{odq}}$ and $\Delta \mathbf{v}_{\mathbf{odq}}$ are the output current and voltage of the GSC.

Taking the small-signal input power ΔP_{rsc} in Fig. 5.3 to be zero, the transfer function from $\Delta \mathbf{v}_{\mathbf{odq}}$ to $\Delta \mathbf{i}_{\mathbf{odq}}$ can be deduced as (5.22).

$$\Delta \mathbf{i}_{\mathbf{odq}}(s) = -\{(\mathbf{B}_{\text{PI-I-2}} - \mathbf{B}_{\text{decpl-2}} + \mathbf{B}_{\text{Lf}} - \mathbf{B}_{\text{PI-I-2}}\mathbf{B}_{\text{PI-Vdc}}G_{Cdc}\mathbf{B}_{\text{v-2}})^{-1}$$
$$\cdot [\mathbf{I} - (\mathbf{B}_{\text{PI-I-2}} - \mathbf{B}_{\text{decpl-2}})\mathbf{B}_{\text{pll-2-Ic}} - \mathbf{B}_{\text{pll-2-Vc}} - \mathbf{B}_{\text{PI-I-2}}\mathbf{B}_{\text{PI-Vdc}}G_{Cdc}\mathbf{B}_{\text{i-2}}] \tag{5.22}$$
$$+ \mathbf{B}_{\text{Cf}}\} \cdot \Delta \mathbf{v}_{\mathbf{odq}}(s)$$

Substituting (5.22) into (5.21), then, the admittance $\mathbf{Y}_{\mathbf{BB}}$ can be calculated as (5.23).

$$\mathbf{Y_{BB}^{dq}}(s) = (\mathbf{B}_{\text{PI-I-2}} - \mathbf{B}_{\text{decpl-2}} + \mathbf{B}_{\text{Lf}} - \mathbf{B}_{\text{PI-I-2}}\mathbf{B}_{\text{PI-Vdc}}G_{Cdc}\mathbf{B}_{\text{v-2}})^{-1} \cdot [\mathbf{I}-$$
$$(\mathbf{B}_{\text{PI-I-2}} - \mathbf{B}_{\text{decpl-2}})\mathbf{B}_{\text{pll-2-Ic}} - \mathbf{B}_{\text{pll-2-Vc}} - \mathbf{B}_{\text{PI-I-2}}\mathbf{B}_{\text{PI-Vdc}}G_{Cdc}\mathbf{B}_{\text{i-2}}] + \mathbf{B}_{\text{Cf}} \quad (5.23)$$

Based on the above analysis, the four admittance components $\mathbf{Y_{AA}}$, $\mathbf{Y_{AB}}$, $\mathbf{Y_{BA}}$, and $\mathbf{Y_{BB}}$ are obtained in (5.12), (5.18), (5.20), and (5.23). Then, the total terminal admittance $\mathbf{Y_{DFIG}}$ can be obtained as "$\mathbf{Y_{DFIG}}$=$\mathbf{Y_{AA}}$+$\mathbf{Y_{AB}}$+$\mathbf{Y_{BA}}$+$\mathbf{Y_{BB}}$" according to (5.10).

5.1.3 Impedance Characteristic Analysis for GFL-DFIG

To demonstrate the correctness of the proposed two-port network decoupled impedance modeling method, a 30 kW GFL-DFIG simulation model is built in MATLAB/Simulink, where a typical impedance/admittance measurement method introduced in [77] is used to measure the admittances.

The system and control parameters of the DFIG, RSC, and GSC are provided in Table 5.1 and Table 5.2. The admittance measurement results of the GFL-DFIG are shown in Fig. 5.6, where the subscript '$_{\text{calc}}$' and '$_{\text{meas}}$' denote calculation and measurement, respectively.

As shown in Fig. 5.6, the red, green, and blue curves show the calculated results of the d-q admittance components $\mathbf{Y_{AA}}$, $\mathbf{Y_{AB}}$, and $\mathbf{Y_{BB}}$ (Notably, since the admittance component $\mathbf{Y_{BA}}$ is equal to zero, it is omitted). Besides, the black curves show the calculated results of the total terminal admittance $\mathbf{Y_{DFIG}}$, which is equal to the sum of $\mathbf{Y_{AA}}$, $\mathbf{Y_{AB}}$, $\mathbf{Y_{BA}}$, and $\mathbf{Y_{BB}}$. Moreover, the red, green, blue, and black '$*$' represent the measured results of the admittances $\mathbf{Y_{AA}}$, $\mathbf{Y_{AB}}$, $\mathbf{Y_{BB}}$, and $\mathbf{Y_{DFIG}}$ by simulation. Fig. 5.6 shows that the measured admittances are overlapped with the calculated admittances, which proves the proposed impedance modeling method is correct.

Notably, Fig. 5.6 shows that there is a resonant peak at 50 Hz for $\mathbf{Y_{AA(calc)}}$. This is because the stator resistance is assumed to be zero when calculating the admittance component $\mathbf{Y_{AA}}$. However, this resonant peak does not exist in the DFIG system, because no resonant phenomenon at 50 Hz can be observed in the time-domain simulation waveforms.

In addition, Fig. 5.6 shows that $\mathbf{Y_{AB}}$ has higher magnitude on the d–d and d–q channels at the low-frequency range, which means that the dc-link coupling has strong impact on the low-frequency admittance characteristics of $\mathbf{Y_{DFIG}}$. So, the conventional modeling method by ignoring the dc-link coupling may reduce the accuracy of the model [J5]. Furthermore, $\mathbf{Y_{DFIG}}$ has negative resistance characteristics on the q–q channel at the low-frequency range, which may worsen the small-signal stability. A simple way to mitigate the negative resistances is to reduce the bandwidth of the PLL, but the dynamic performance of the PLL will be sacrificed meanwhile. So, further exploration may be necessary to find a better solution.
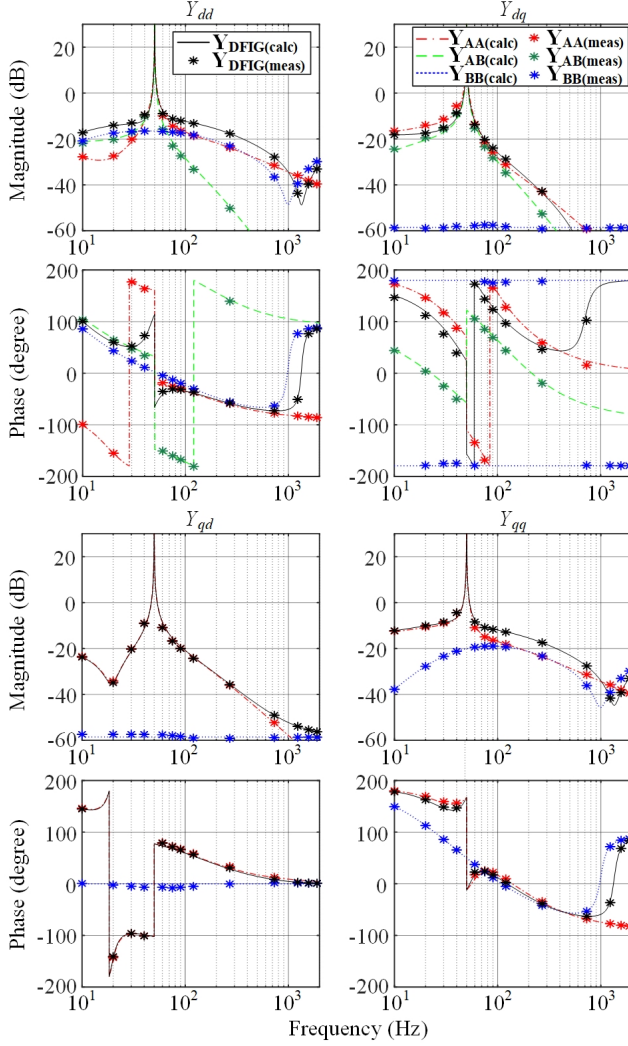
Fig. 5.6: Small-signal d-q admittance measurement results for GFL-DFIGs.

5.2   Control and Impedance Modeling of GFM-DFIG

After analyzing GFL-DFIGs in the previous section, this section will move the research focus to GFM-DFIGs. A typical GFM-PMSG with a PLL-based dc-link voltage control on the GSC is presented in Fig. 5.7, where the GFM function is realized on the RSC by using a virtual admittance control [83]. Fig. 5.7(a) shows the physical configuration of the Type-3 wind generation system. Considering that Fig. 5.7(a) is completely the same as Fig. 5.1(a), the
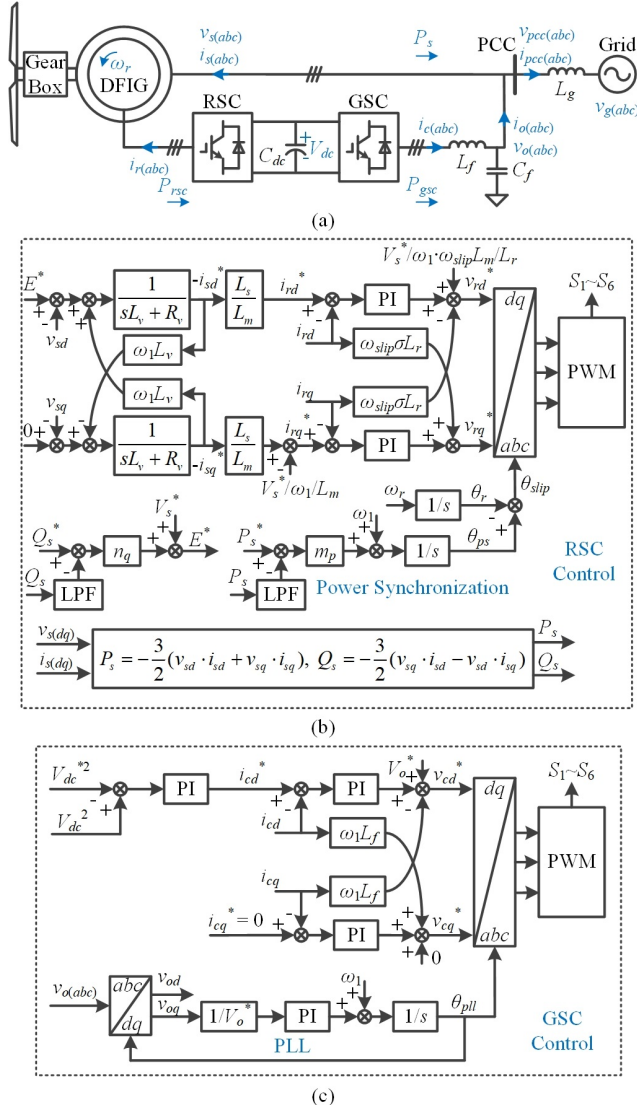
Fig. 5.7: Typical GFM control scheme for Type-3 wind generation systems. (a) Physical configuration of Type-3 wind generation systems; (b) GFM control scheme on the RSC; (c) PLL-based dc voltage control scheme on the GSC [J4].

description of the physical system is omitted.

Fig. 5.7(b) shows the power synchronization control scheme on the RSC, which includes outer power control loops and inner voltage and current control loops. The current and voltage controls are performed in the rotating d-q frame. The reactive power and active power are regulated to generate the voltage magnitude and angle. Moreover, Fig. 5.7(c) shows the PLL-based

(a)

(b)
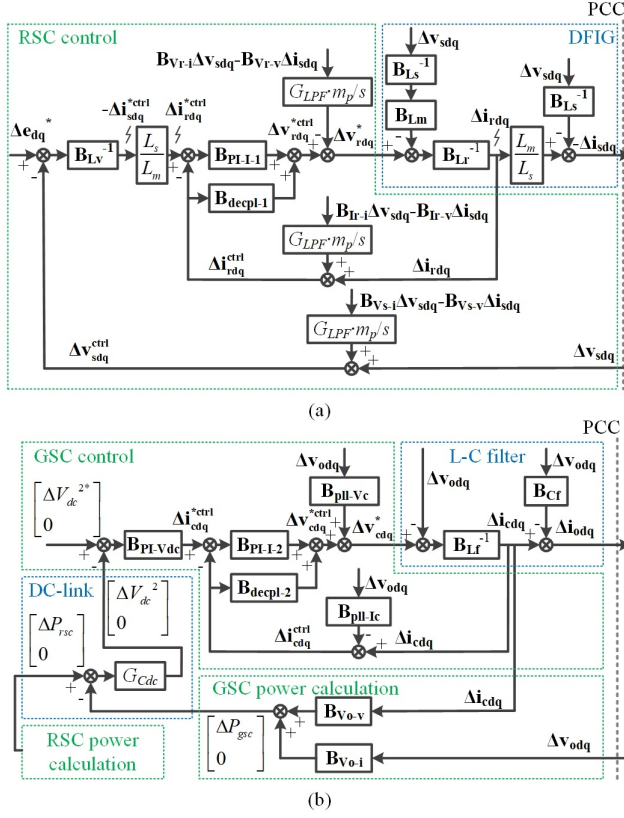
Fig. 5.8: Small-signal d-q impedance model of GFM-DFIG system presented in Fig. 5.7. (a) Impedance model of RSC; (b) Impedance model of GSC.

dc voltage control approach on the GSC, which is completely the same as Fig. 5.1(c). So, the description of this control approach is also omitted. Afterwards, the small-signal impedance model of GFM-DFIGs will be introduced.

5.2.1 Impedance Modeling of GFM-DFIG

Like the GFL-DFIG system introduced in previous sections, the GFM-DFIG system can be separated into a rotor-side subsystem and a grid-side subsystem for analysis. The small-signal d-q impedance model of the rotor-side subsystem is shown in Fig. 5.8(a), where the DFIG model is the same as that in Fig. 5.2 and the RSC model is similar to the model of GFM-PMSG presented in Fig. 4.13. Besides, the small-signal d-q impedance model of the grid-side subsystem is shown in Fig. 5.8(b), which is completely same as the GSC model of GFL-DFIG presented in Fig. 5.3. Hence, the detailed process of building the models shown in Fig. 5.8 is omitted here.

5.2.2 Proposed Two-Port Network Modeling Method

After building the small-signal impedance models of the rotor-side and the grid-side subsystems, the ac terminal impedance of the whole DFIG system needs to be derived. As aforementioned, a two-port-network-based decoupled impedance modeling method shown in Fig. 5.5 can be used to calculate the ac terminal admittance of the GFL-DFIG system. In fact, this method is also effective to calculate the ac terminal admittance of the GFM-DFIG system. According to (5.10), the total terminal admittance $\mathbf{Y_{DFIG}}$ is equal to the sum of the four admittance components $\mathbf{Y_{AA}}$, $\mathbf{Y_{AB}}$, $\mathbf{Y_{BA}}$, and $\mathbf{Y_{BB}}$. The calculation of the four admittance components will be introduced as follows.

A. Admittance calculation from port A to port A in d-q frame

As presented in Fig. 5.5(a), when injecting a small-signal voltage perturbation $\Delta \mathbf{v_A}$ into the two-port network from port A, there is a current response $\Delta \mathbf{i_{AA}}$ at port A. So, the admittance $\mathbf{Y_{AA}}$ can be expressed as (5.11). Then, according to (5.11) and Fig. 5.8(a), $\mathbf{Y_{AA}}$ can be calculated as:

$$
\mathbf{Y_{AA}^{dq}}(s) = \{ \frac{L_s}{L_m}(\mathbf{B_{Lr}} + \mathbf{B_{PI\text{-}I\text{-}1}} - \mathbf{B_{decpl\text{-}1}}) + G_{LPF} \cdot \frac{m_p}{s} \cdot [\mathbf{B_{Vr\text{-}v}} + (\mathbf{B_{PI\text{-}I\text{-}1}}
$$
$$
- \mathbf{B_{decpl\text{-}1}}) \cdot \mathbf{B_{Ir\text{-}v}} + \frac{L_s}{L_m} \cdot \mathbf{B_{PI\text{-}I\text{-}1}} \cdot \mathbf{B_{Lv}}^{-1} \cdot \mathbf{B_{Vs\text{-}v}}] \}^{-1} \cdot \{ \mathbf{B_{Lm}} \mathbf{B_{Ls}}^{-1} + \frac{L_s}{L_m}
$$
$$
\cdot \mathbf{B_{PI\text{-}I\text{-}1}} \cdot \mathbf{B_{Lv}}^{-1} + \frac{L_s}{L_m}(\mathbf{B_{Lr}} + \mathbf{B_{PI\text{-}I\text{-}1}} - \mathbf{B_{decpl\text{-}1}}) \cdot \mathbf{B_{Ls}}^{-1} + G_{LPF} \cdot \frac{m_p}{s}
$$
$$
\cdot [\mathbf{B_{Vr\text{-}i}} + (\mathbf{B_{PI\text{-}I\text{-}1}} - \mathbf{B_{decpl\text{-}1}}) \cdot \mathbf{B_{Ir\text{-}i}} + \frac{L_s}{L_m} \cdot \mathbf{B_{PI\text{-}I\text{-}1}} \cdot \mathbf{B_{Lv}}^{-1} \cdot \mathbf{B_{Vs\text{-}i}}] \}
$$

(5.24)

where the detailed expressions of the matrixes are given in (5.25).

$$
\begin{cases}
\mathbf{B_{PI\text{-}I\text{-}1}} = \begin{bmatrix} K_p + K_i/s & 0 \\ 0 & K_p + K_i/s \end{bmatrix}, & \mathbf{B_{Ls}} = \begin{bmatrix} sL_s & -\omega_1 L_s \\ \omega_1 L_s & sL_s \end{bmatrix} \\[2mm]
\mathbf{B_{decpl\text{-}1}} = \begin{bmatrix} 0 & -\omega_{slip}\sigma L_r \\ \omega_{slip}\sigma L_r & 0 \end{bmatrix}, & \mathbf{B_{Lm}} = \begin{bmatrix} sL_m & -\omega_{slip}L_m \\ \omega_{slip}L_m & sL_m \end{bmatrix} \\[2mm]
\mathbf{B_{Lv}} = \begin{bmatrix} sL_v + R_v & -\omega_1 L_v \\ \omega_1 L_v & sL_v + R_v \end{bmatrix}, & \mathbf{B_{Lr}} = \begin{bmatrix} s\sigma L_r + R_r & -\omega_{slip}\sigma L_r \\ \omega_{slip}\sigma L_r & s\sigma L_r + R_r \end{bmatrix} \\[2mm]
\mathbf{B_{Vs\text{-}i}} = \frac{3}{2}\begin{bmatrix} v_{sq0}i_{sd0} & v_{sq0}i_{sq0} \\ -v_{sd0}i_{sd0} & -v_{sd0}i_{sq0} \end{bmatrix}, & \mathbf{B_{Vs\text{-}v}} = \frac{3}{2}\begin{bmatrix} -v_{sq0}v_{sd0} & -v_{sq0}v_{sq0} \\ v_{sd0}v_{sd0} & v_{sd0}v_{sq0} \end{bmatrix} \\[2mm]
\mathbf{B_{Vr\text{-}i}} = \frac{3}{2}\begin{bmatrix} v_{rq0}i_{sd0} & v_{rq0}i_{sq0} \\ -v_{rd0}i_{sd0} & -v_{rd0}i_{sq0} \end{bmatrix}, & \mathbf{B_{Vr\text{-}v}} = \frac{3}{2}\begin{bmatrix} -v_{rq0}v_{sd0} & -v_{rq0}v_{sq0} \\ v_{rd0}v_{sd0} & v_{rd0}v_{sq0} \end{bmatrix} \\[2mm]
\mathbf{B_{Ir\text{-}i}} = \frac{3}{2}\begin{bmatrix} i_{rq0}i_{sd0} & i_{rq0}i_{sq0} \\ -i_{rd0}i_{sd0} & -i_{rd0}i_{sq0} \end{bmatrix}, & \mathbf{B_{Ir\text{-}v}} = \frac{3}{2}\begin{bmatrix} -i_{rq0}v_{sd0} & -i_{rq0}v_{sq0} \\ i_{rd0}v_{sd0} & i_{rd0}v_{sq0} \end{bmatrix}
\end{cases}
$$

(5.25)

B. Admittance calculation from port A to port B in d-q frame

As presented in Fig. 5.5(b), when injecting a small-signal voltage perturbation $\Delta \mathbf{v_A}$ into the two-port network from port A, there is a current response

$\Delta \mathbf{i_{AB}}$ at port B. So, the admittance $\mathbf{Y_{AB}}$ can be expressed as (5.13). Since the GSC model of the GFM-DFIG system is completely the same as that of the GFL-DFIG system, the calculation process of $\mathbf{Y_{AB}}$ is the same as (5.13)-(5.18). Therefore, according to (5.18), the admittance $\mathbf{Y_{AB}}$ can be calculated as:

$$
\begin{aligned}
\mathbf{Y_{AB}^{dq}}(s) = &-\frac{3}{2} \cdot (\mathbf{B}_{\text{PI-I-2}} - \mathbf{B}_{\text{decpl-2}} + \mathbf{B}_{\text{Lf}} - \mathbf{B}_{\text{PI-I-2}}\mathbf{B}_{\text{PI-Vdc}}G_{Cdc}\mathbf{B}_{\text{Vo-v}})^{-1} \\
&\cdot (\mathbf{B}_{\text{PI-I-2}}\mathbf{B}_{\text{PI-Vdc}}G_{Cdc}) \cdot \left\{ \left[\frac{(L_m{}^2 - L_sL_r)s - 2R_rL_s}{L_m} \cdot \begin{bmatrix} i_{rd0} & i_{rq0} \\ 0 & 0 \end{bmatrix} \right. \right. \\
&\left. - \frac{\omega_{slip}}{\omega_1} \cdot \begin{bmatrix} v_{sd0} & v_{sq0} \\ 0 & 0 \end{bmatrix} \right] \cdot \mathbf{Y_{AA}^{dq}}(s) + \begin{bmatrix} \frac{L_rs + 2R_r}{L_m} \cdot \begin{bmatrix} i_{rd0} & i_{rq0} \\ 0 & 0 \end{bmatrix} \end{bmatrix} \\
&\left. + \omega_{slip} \cdot \begin{bmatrix} -i_{sq0} & i_{sd0} \\ 0 & 0 \end{bmatrix} \right] \cdot \begin{bmatrix} s & -\omega_1 \\ \omega_1 & s \end{bmatrix}^{-1} \right\}
\end{aligned}
\tag{5.26}
$$

C. Admittance calculation from port B to port A in d-q frame

As presented in Fig. 5.5(c), when injecting a small-signal voltage perturbation $\Delta \mathbf{v_B}$ into the two-port network from port B, there is a current response $\Delta \mathbf{i_{BA}}$ at port A. So, the admittance $\mathbf{Y_{BA}}$ can be expressed as (5.19). Since the measured dc voltage is used for the voltage modulation on the RSC, the output voltage of the RSC is independent from the dc-link voltage. Thus, the injected small-signal voltage perturbation at port B cannot be transferred to port A. Therefore, the small-signal current response $\Delta \mathbf{i_{BA}}$ is equal to zero theoretically. The admittance $\mathbf{Y_{BA}}$ can be derived as:

$$
\mathbf{Y_{BA}^{dq}}(s) = \frac{\mathbf{0}}{\Delta \mathbf{v_B^{dq}}(s)} = \mathbf{0}
\tag{5.27}
$$

D. Admittance calculation from port B to port B in d-q frame

As presented in Fig. 5.5(d), when injecting a small-signal voltage perturbation $\Delta \mathbf{v_B}$ into the two-port network from port B, there is a current response $\Delta \mathbf{i_{BB}}$ at port B. So, the admittance $\mathbf{Y_{BB}}$ can be expressed as (5.21). Since the GSC model of the GFM-DFIG system is completely same as that of the GFL-DFIG system, the calculation process of $\mathbf{Y_{BB}}$ is the same as (5.21)-(5.23). Therefore, according to (5.23), the admittance $\mathbf{Y_{BB}}$ can be deduced as:

$$
\begin{aligned}
\mathbf{Y_{BB}^{dq}}(s) = &(\mathbf{B}_{\text{PI-I-2}} - \mathbf{B}_{\text{decpl-2}} + \mathbf{B}_{\text{Lf}} - \mathbf{B}_{\text{PI-I-2}}\mathbf{B}_{\text{PI-Vdc}}G_{Cdc}\mathbf{B}_{\text{Vo-v}})^{-1} \cdot [\mathbf{I} \\
&- (\mathbf{B}_{\text{PI-I-2}} - \mathbf{B}_{\text{decpl-2}})\mathbf{B}_{\text{pll-Ic}} - \mathbf{B}_{\text{pll-Vc}} - \mathbf{B}_{\text{PI-I-2}}\mathbf{B}_{\text{PI-Vdc}}G_{Cdc}\mathbf{B}_{\text{Vo-i}}] + \mathbf{B}_{\text{Cf}}
\end{aligned}
\tag{5.28}
$$

Based on the above analysis, the four admittance components $\mathbf{Y_{AA}}$, $\mathbf{Y_{AB}}$, $\mathbf{Y_{BA}}$, and $\mathbf{Y_{BB}}$ are obtained in (5.24), (5.26), (5.27), and (5.28). Then, the total terminal admittance $\mathbf{Y_{DFIG}}$ can be obtained by adding the four admittance components, namely, "$\mathbf{Y_{DFIG}} = \mathbf{Y_{AA}} + \mathbf{Y_{AB}} + \mathbf{Y_{BA}} + \mathbf{Y_{BB}}$".
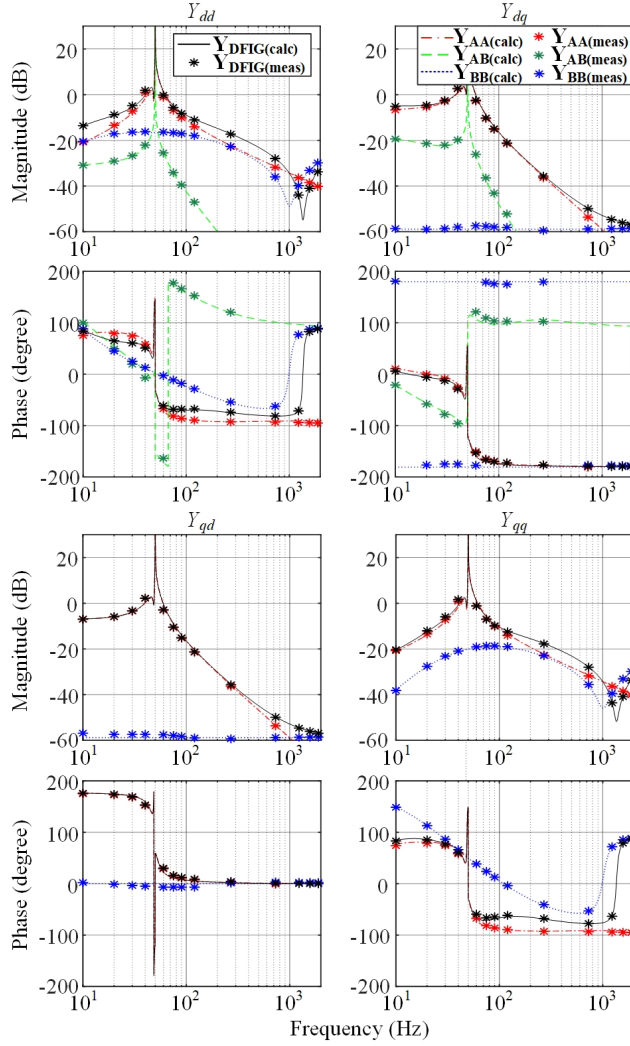
Fig. 5.9: Small-signal d-q admittance measurement results for GFM-DFIGs.

5.2.3 Impedance Characteristic Analysis for GFM-DFIG

To demonstrate the correctness of the proposed two-port network decoupled impedance modeling method, a 30 kW GFL-DFIG simulation model is built in MATLAB/Simulink. The parameters of the DFIG are same as that in Table 5.1. The parameters of the GSC are same as that in Table 5.2. Besides, the droop coefficient and the virtual admittance in the RSC control scheme are the same as that in [C5]. The d-q admittance measurement results of the GFM-DFIG are shown in Fig. 5.9, where the subscript 'calc' and 'meas' denote

calculation and measurement, respectively.

As presented in Fig. 5.9, the red, green, and blue curves show the calculated results of the d-q admittance components $\mathbf{Y_{AA}}$, $\mathbf{Y_{AB}}$, and $\mathbf{Y_{BB}}$ (Notably, $\mathbf{Y_{BA}}$ is omitted, because it is equal to zero). Besides, the black curves show the calculated results of the total terminal admittance $\mathbf{Y_{DFIG}}$, which is equal to the sum of $\mathbf{Y_{AA}}$, $\mathbf{Y_{AB}}$, $\mathbf{Y_{BA}}$, and $\mathbf{Y_{BB}}$. Moreover, the red, green, blue, and black '∗' represent the measured results of the admittances $\mathbf{Y_{AA}}$, $\mathbf{Y_{AB}}$, $\mathbf{Y_{BB}}$, and $\mathbf{Y_{DFIG}}$ by simulation. Fig. 5.9 shows that the measured admittances are overlapped with the calculated admittances.

In addition, Fig. 5.9 shows that the magnitudes of $\mathbf{Y_{AB}}$ are much lower than the magnitudes of $\mathbf{Y_{DFIG}}$, which means that the dc-link coupling has weak impact on the total admittance $\mathbf{Y_{DFIG}}$. So, it can be ignored approximately. Furthermore, $\mathbf{Y_{DFIG}}$ does not have negative resistance characteristics on either the d–d channel or the q–q channel, which indicates the small-signal stability of GFM-DFIG should be quite good.

5.3 Summary

This chapter has provided a systematic discussion of small-signal impedance modeling of GFL and GFM DFIGs. At first, a two-port network impedance modeling method for GFL-DFIGs is introduced. With the proposed modeling method, the whole DFIG system can be decomposed into four subsystems. Thus, the models of the RSC, GSC, and dc-link coupling can be built separately, so the complexity of the modeling process can be degraded. Then, the admittance characteristics of GFL-DFIGs are presented on Bode diagrams. It is found that the dc-link coupling has strong impact on the total terminal admittance of GFL-DFIGs at the low-frequency range, which should be considered in order to improve the accuracy of the model. Besides, negative resistance characteristics of GFL-DFIGs on both d–d and q–q channels can be observed, which may worsen the small-signal stability.

Afterwards, the proposed two-port network impedance modeling method is applied to GFM-DFIGs. With the proposed modeling method, a full-order impedance model of the GFM-DFIG is built. Then, the admittance characteristics of GFM-DFIGs are presented on Bode diagrams. It is found that the dc-link coupling in GFM-DFIGs has weak impact on the total terminal admittance, which can be ignored approximately. Moreover, there are no negative resistance characteristics for GFM-DFIGs on either the d–d channel or the q–q channel, which reflects the small-signal stability of GFM-DFIGs should be very good. Therefore, the GFM-DFIGs may be more suitable to operate in weak grid cases than the GFL-DFIGs.

Chapter 6

# Case Studies of Multiple Grid-Connected Wind Generators

In previous chapters, the case of a single wind generator connected to a Thevenin equivalent grid has been studied. This chapter will move the research focus to the multiple wind generators system to validate the effectiveness of the proposed solutions. In addition, considering most offshore wind power plants (e.g., Anholt in Denmark) are equipped with Type-4 wind generators, paralleled Type-4 wind generators will be evaluated in this section. Firstly, two paralleled Type-4 wind generators connected to a Thevenin equivalent grid will be analyzed. Then, a more realistic case of Anholt Offshore Wind Power Plant consisting of Type-4 wind generators with proposed control solutions will be studied.

6.1   Case 1: Two Paralleled 30 kW Wind Generators

To avoid the study case being too complicated to understand, a simple case of two paralleled Type-4 wind generators connected to a Thevenin equivalent grid is chosen to study first. The configuration of the study system is presented in Fig. 6.1, where two Type-4 wind generators are connected at the PCC. Besides, a load Z_{load} is intentionally added to evaluate the island operation ability of GFM wind generators. In order to differentiate the two generators, subscript '$_1$' denotes the variables of generator 1, while subscript '$_2$' denotes the variables of generator 2. Moreover, Q and P are the output reactive power and active power of the GSC. V_{dc} is the dc-link voltage. T_e and ω_m are the mechanical torque and angular speed of the PMSG, respectively.

Table 6.1: Parameters of 30 kW GFL-PMSGs [84].

Parameters	Values
Rated active power, P_N	30 kW (1 p.u.)
Rated phase voltage (peak value), V_N	$\sqrt{2/3}\cdot$ 380 V (1 p.u.)
Fundamental angular frequency, ω_N	$2\pi\cdot$50 rad/s
Pole pairs of PMSG, n_{pp}	4
Stator inductance of PMSG, L_s	0.8 mH
Stator resistance of PMSG, R_s	50 mΩ
Rotor flux of PMSG, Ψ_r	192 mWb
Rated dc-link voltage, V_{dc}	700 V
Sampling frequency, f_s	10 kHz
Dc-link capacitance, C_{dc}	3 p.u.
Output filter inductance & resistance, L_f, R_f	0.15 p.u., 0.005 p.u.
Output filter capacitance, C_f	0.02 p.u.
Current loop bandwidth on MSC, ω_{i-MSC}	4000 rad/s
Dc voltage loop bandwidth on MSC, ω_{Vdc}	100 rad/s
Current loop bandwidth on GSC, ω_{i-GSC}	4000 rad/s
PLL bandwidth on GSC, ω_{pll}	500 rad/s
Auxiliary PLL bandwidth on GSC, ω_{apll}	50 rad/s
Ac voltage magnitude loop bandwidth on GSC, ω_{Vac}	50 rad/s
Active power loop bandwidth on GSC, ω_p	10 rad/s
Output ac current limit on GSC (peak value), I_{lim}	1 p.u.
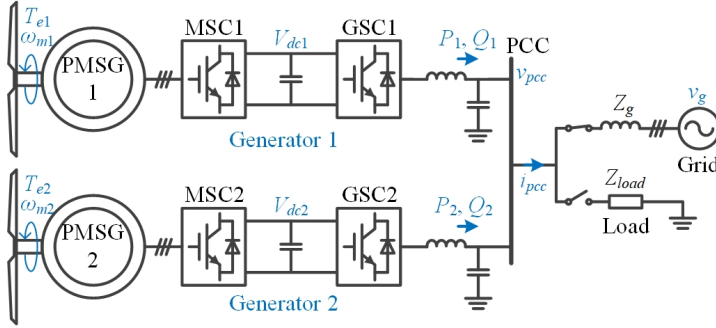
Fig. 6.1: System configuration of two paralleled Type-4 wind generators connected to a Thevenin equivalent grid or a load.

6.1.1   Paralleled GFL-PMSGs in Strong and Weak Grids

At first, two paralleled GFL-PMSGs with the proposed control solution are investigated. Specifically, the machine-side dc voltage control approach presented in Fig. 4.1(b) is used to control the MSC, and the proposed double-PLL-based impedance reshaping control approach presented in Fig. 2.18 is used to control the GSC. A 30 kW simulation model is built to study stability of paralleled GFL-PMSGs, where two GFL-PMSGs have the same parameters.

6.1. Case 1: Two Paralleled 30 kW Wind Generators

Fig. 6.2: Simulation results of two paralleled 30 kW GFL-PMSGs under grid frequency drop from 50 to 49.2 Hz. (a) A strong grid case (SCR = 15); (b) A weak grid case (SCR = 1.5).

The simulation parameters of GFL-PMSGs are listed in Table 6.1, where the parameters of a 30 kW PMSG are the same as that of a preset model of PMSG "No. 15" in the MATLAB/Simulink Library [84].

Referring to a standardized evaluation framework for weak grid-connected converters introduced in [85], the active power step, grid frequency drop, and voltage sag scenarios are chosen for testing. The simulation results of two paralleled 30 kW GFL-PMSGs under grid frequency drop cases are presented in Fig. 6.2. Since the simulation results of the two generators are completely the same, Fig. 6.2 only shows the results of generator 1. As illustrated in
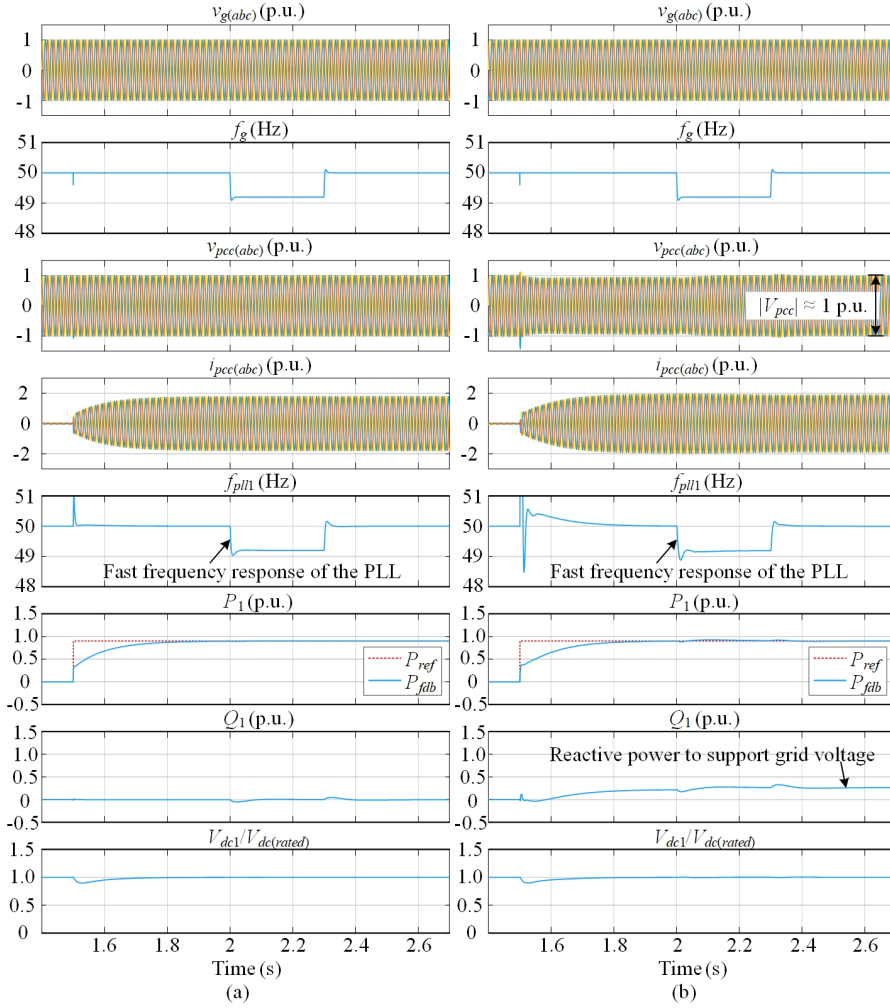
Fig. 6.3: Simulation results of two paralleled 30 kW GFL-PMSGs under grid voltage sag from 1 to 0.2 p.u. (a) A strong grid case (SCR = 15); (b) A weak grid case (SCR = 1.5).

Fig. 6.2, initially, given a 0.9 p.u. of power reference at the instant of 1.5s, the active power reaches 0.9 p.u. after 0.3 seconds. Then, the grid frequency is dropped from 50 Hz to 49.2 Hz at the instant of 2s. It shows that the frequency response of the PLL is very fast. This is because a high bandwidth of the PLL can be applied by using the proposed impedance reshaping control approach, which is beneficial for improving the transient performance [J2]. Besides, the GFL-PMSG can provide more reactive power in the weak grid case to support the grid voltage to meet the grid code requirement.

Moreover, the simulation results of two paralleled 30 kW GFL-PMSGs

Table 6.2: Parameters of 30 kW GFM-PMSGs.

Parameters	Values
Rated active power, P_N	30 kW (1 p.u.)
Rated phase voltage (peak value), V_N	$\sqrt{2/3}\cdot$ 380 V (1 p.u.)
Fundamental angular frequency, ω_N	$2\pi\cdot$50 rad/s
Pole pairs of PMSG, n_{pp}	4
Stator inductance of PMSG, L_s	0.8 mH
Stator resistance of PMSG, R_s	50 mΩ
Rotor flux of PMSG, Ψ_r	192 mWb
Rated dc-link voltage, V_{dc}	700 V
Sampling frequency, f_s	10 kHz
Dc-link capacitance, C_{dc}	3 p.u.
Output filter inductance & resistance, L_f, R_f	0.15 p.u., 0.005 p.u.
Output filter capacitance, C_f	0.02 p.u.
Current loop bandwidth on MSC, ω_{i-MSC}	4000 rad/s
Dc voltage loop bandwidth on MSC, ω_{Vdc}	100 rad/s
Current loop bandwidth on GSC, ω_{i-GSC}	4000 rad/s
Virtual resistance and inductance on GSC, L_v, R_v	0.5 p.u., 0.05 p.u.
Reactive power droop coefficient on GSC, n_q	2.5% V_N/P_N
Active power droop coefficient on GSC, m_p	2.5% ω_N/P_N
PLL bandwidth in virtual power angle limiter, ω_{pll}	50 rad/s
Output ac current limit on GSC (peak value), I_{lim}	1 p.u.

under grid voltage sag cases are presented in Fig. 6.3. Initially, the active power is controlled to be 0.9 p.u. Then, the grid voltage is sagged from 1 p.u. to 0.2 p.u. at the instant of 2s and lasts for 0.3 seconds. It can be seen that the GFL-PMSGs have the ability to ride through the fault in either strong or weak grid cases. Besides, during the fault period, the GFL-PMSG can inject reactive current and reactive power quickly to meet the grid code requirement. Fig. 6.3(b) also shows that during the fault recovery period, the proposed method has an overvoltage problem in the weak grid case. However, the transient performance during the fault recovery period is not the research focus of this thesis, which needs to be studied further in the future. And a typical method of switching the current reference to a constant during the fault period [86] is worth considering use in the future.

6.1.2 Paralleled GFM-PMSGs in Strong and Weak Grids

Afterwards, two paralleled GFM-PMSGs with the proposed control solution are investigated in this section. Specifically, the machine-side dc voltage control approach presented in Fig. 4.1(b) is used to control the MSC, and the virtual-admittance-based GFM control scheme with the proposed power-
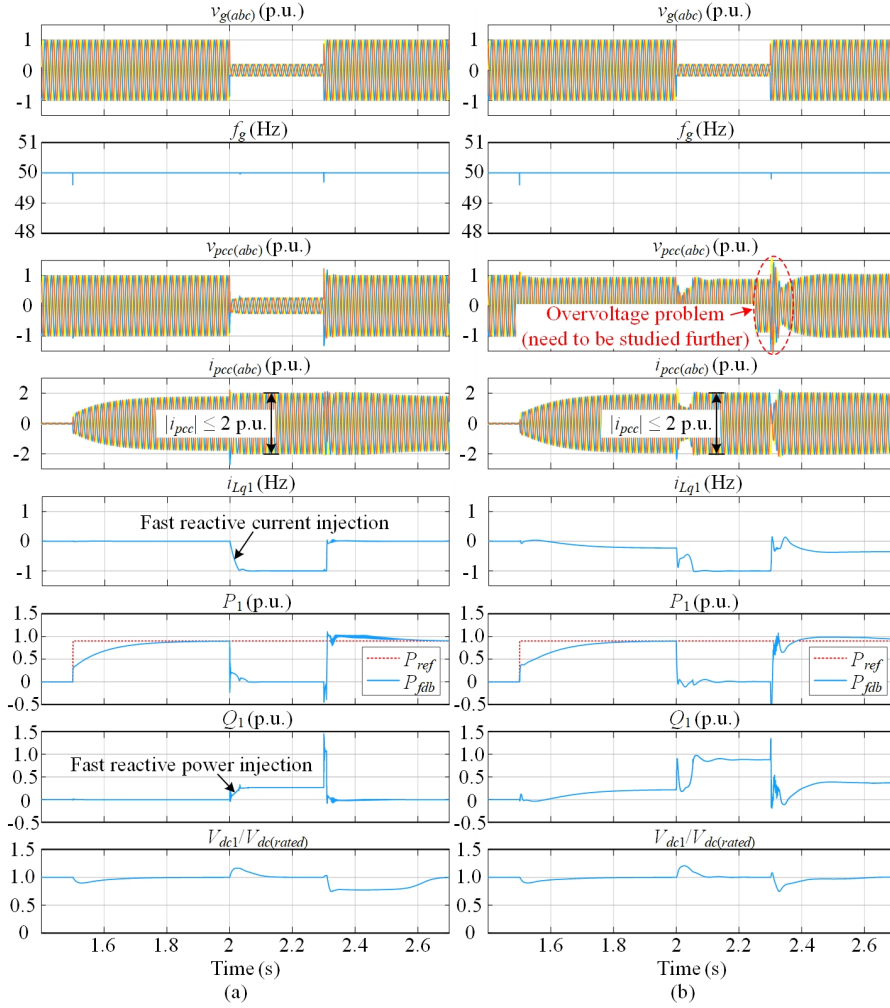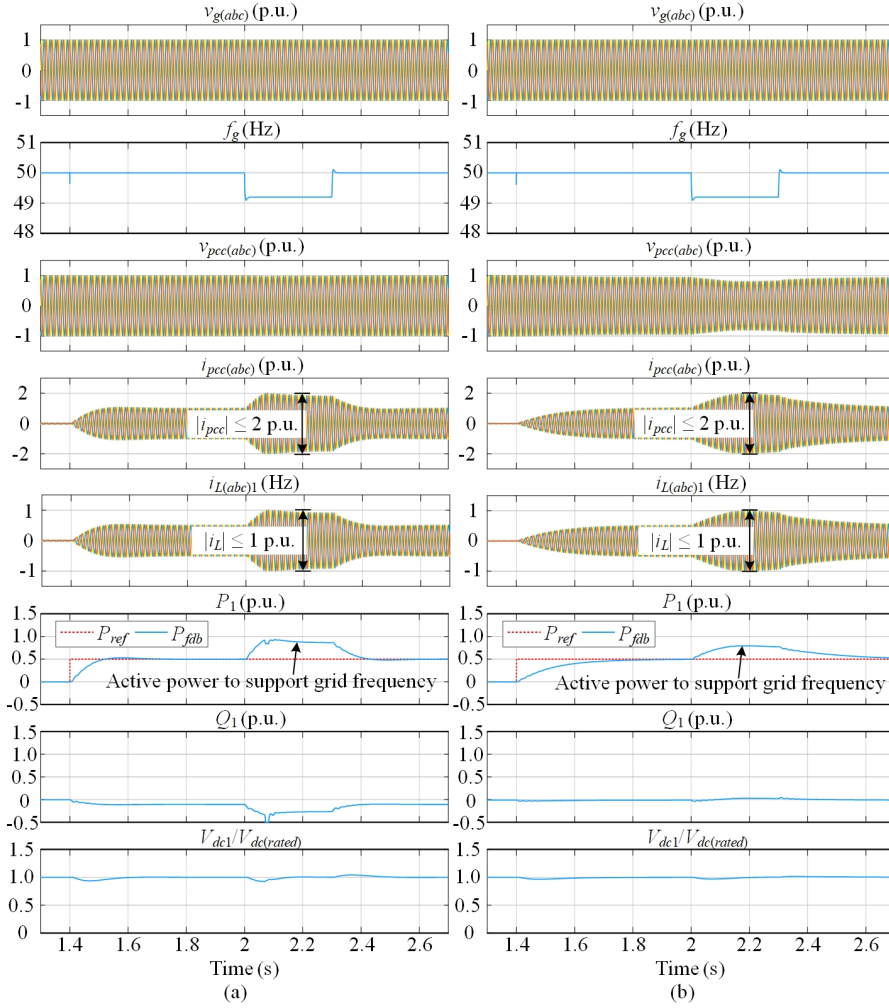
Fig. 6.4: Simulation results of two paralleled 30 kW GFM-PMSGs under grid frequency drop from 50 to 49.2 Hz. (a) A strong grid case (SCR = 15); (b) A weak grid case (SCR = 1.5).

angle-based overcurrent protection approach shown in Fig. 3.15 is used to control the GSC. A 30 kW simulation model is built to study stability of paralleled GFM-PMSGs, where two GFM-PMSGs have the same parameters. The simulation parameters of GFM-PMSGs are listed in Table 6.2.

The simulation results of two paralleled 30 kW GFM-PMSGs under grid frequency drop cases are presented in Fig. 6.4. Initially, the active power is controlled to be 0.5 p.u. Then, the grid frequency is dropped from 50 Hz to 49.2 Hz at the instant of 2s. The GFM-PMSG can provide more active power to support the grid frequency to meet the grid code requirement. More im-
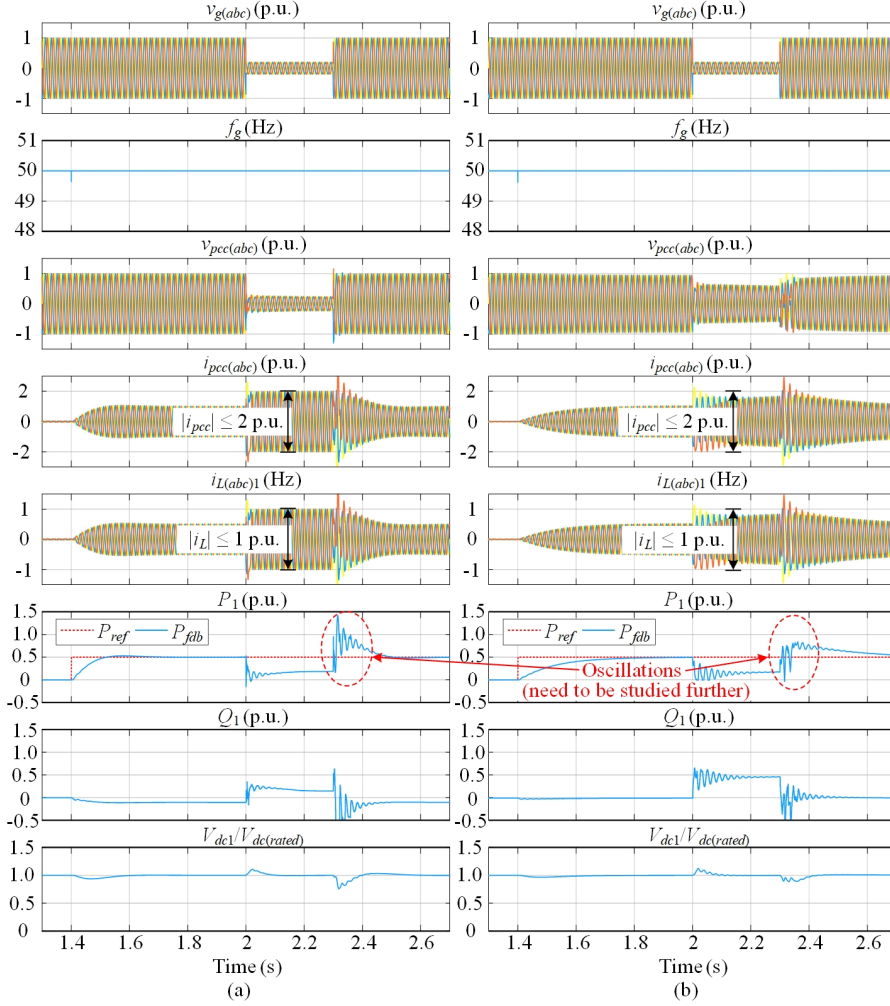
Fig. 6.5: Simulation results of two paralleled 30 kW GFM-PMSGs under grid voltage sag from 1 to 0.2 p.u. (a) A strong grid case (SCR = 15); (b) A weak grid case (SCR = 1.5).

portantly, the output current can be restricted within 1 p.u. and the stability of the GFM-PMSGs can be maintained by using the proposed approach.

Moreover, the simulation results of two paralleled 30 kW GFM-PMSGs under grid voltage sag cases are presented in Fig. 6.5. Initially, the active power is controlled to be 0.5 p.u. Then, the grid voltage is sagged from 1 p.u. to 0.2 p.u. at the instant of 2s and lasts for 0.3 seconds. It can be seen that the GFM-PMSGs have the ability to ride through the fault in either strong or weak grid cases. More importantly, the output current can be restricted within 1 p.u. during the fault period and the stability of the GFM-PMSGs

Table 6.3: Parameters of 4 MW grid-connected PMSGs [87].

Parameters	Values
Rated active power, P_N	4 MW (1 p.u.)
Rated phase voltage (peak value), V_N	$\sqrt{2/3}\cdot$ 690 V (1 p.u.)
Pole pairs of PMSG, n_{pp}	2
Stator inductance & resistance, L_s, R_s	1 mH, 2.5 mΩ
Rotor flux of PMSG, Ψ_r	5.84 Wb
Rated dc-link voltage, V_{dc}	1500 V
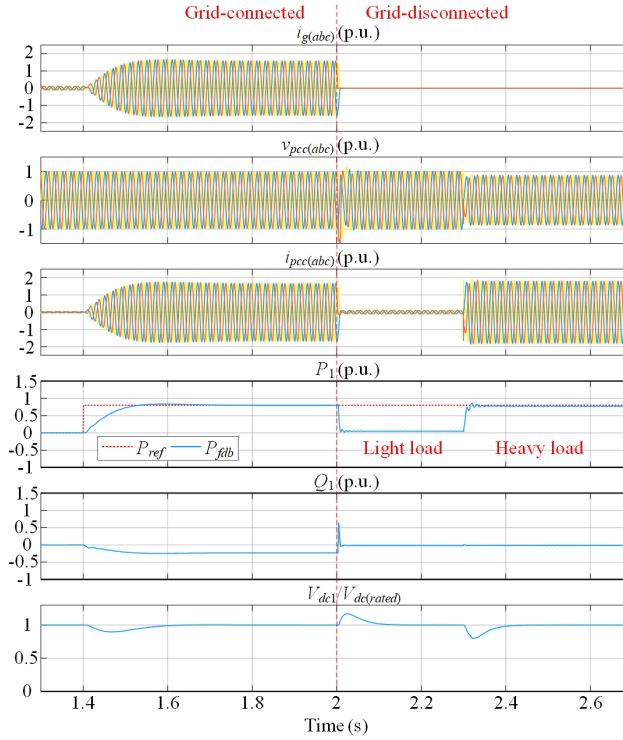
Fig. 6.6: Simulation results of two paralleled 30 kW GFM-PMSGs in an islanded case.

can be maintained by the proposed approach [J3]. However, during the fault recovery period, the proposed method has oscillation problems in both weak and strong grid cases, as presented in Fig. 6.5. This problem is still a challenging issue, which is worth studying further in the future.

Furthermore, having the island operation ability is another important feature of GFM-PMSGs. To evaluate the performance of GFM-PMSGs in islanded cases, the simulation results of two paralleled 30 kW GFM-PMSGs in an islanded case are shown in Fig. 6.6. In the beginning, the GFM-PMSGs
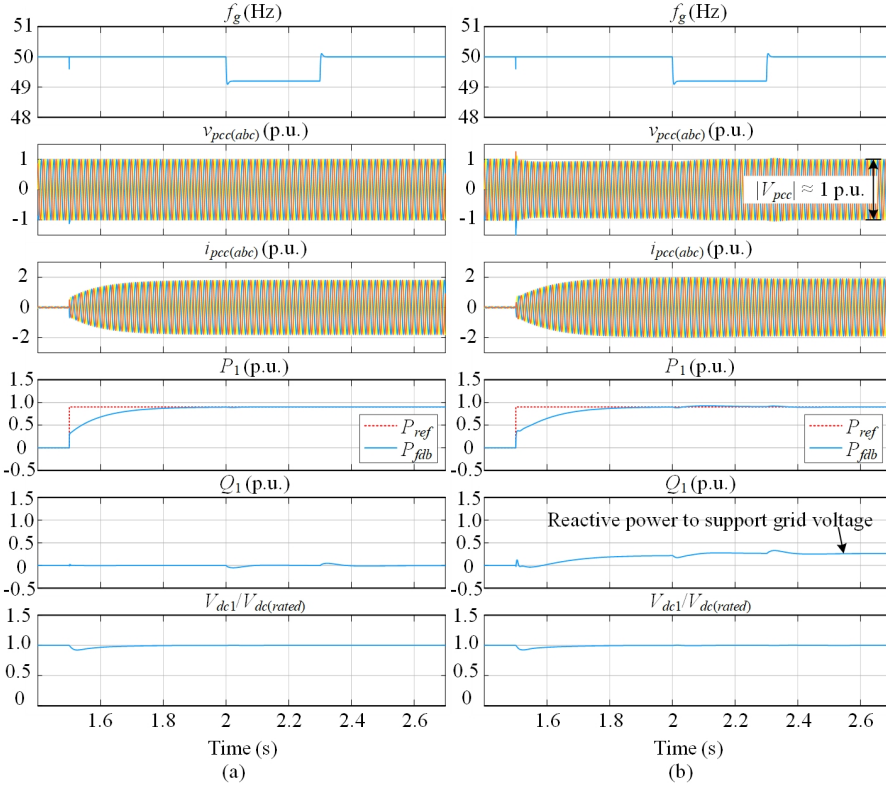
Fig. 6.7: Simulation results of two paralleled 4 MW GFL-PMSGs under grid frequency drop from 50 to 49.2 Hz. (a) A strong grid case (SCR = 15); (b) A weak grid case (SCR = 1.5).

have the connection with the grid. Then, the grid is disconnected at the instant of 2s. It shows that two paralleled GFM-PMSGs can still operate stably in the islanded case. Later, when the load is increased to the rated value at the instant of 2.3s, GFM-PMSGs are still stable.

6.2 Case 2: Two Paralleled 4 MW Wind Generators

After evaluating two paralleled Type-4 wind generators at a lower power level (i.e., 30 kW) in the previous section, a higher power level (i.e., 4 MW) case will be investigated in this section. The system configuration of two paralleled 4 MW Type-4 wind generators is basically same as that presented in Fig. 6.1. Namely, two paralleled Type-4 wind generators are connected to a Thevenin equivalent grid at the PCC. And the grid impedance can be changed to build weak and strong grid conditions. Referring to [87], the parameters of a 4 MW grid-connected PMSG is listed in Table 6.3.
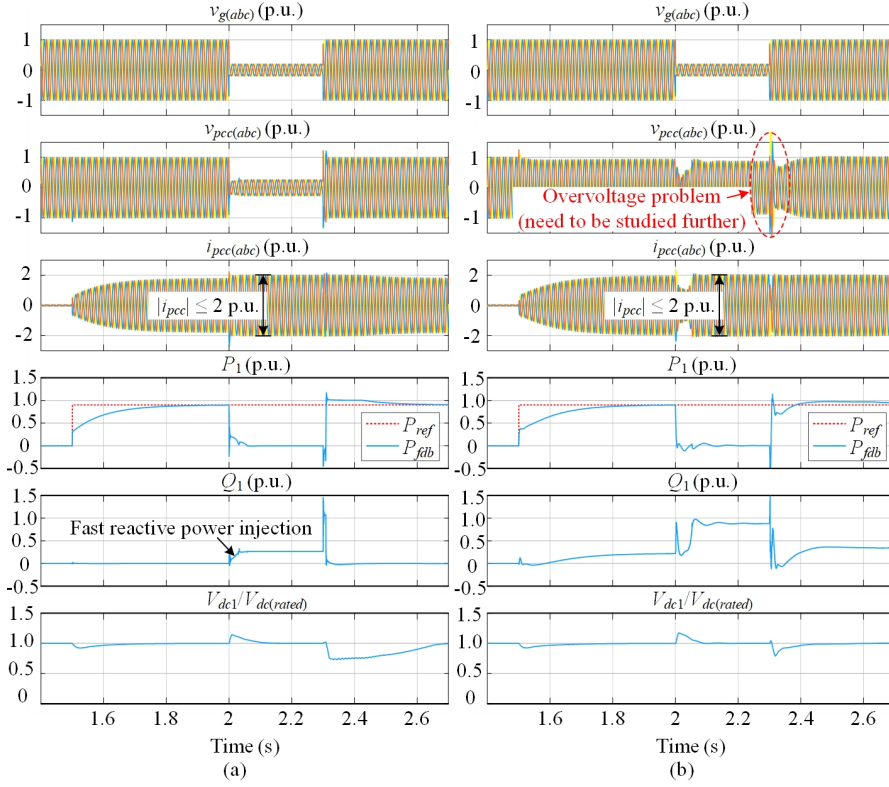
Fig. 6.8: Simulation results of two paralleled 4 MW GFL-PMSGs under grid voltage sag from 1 to 0.2 p.u. (a) A strong grid case (SCR = 15); (b) A weak grid case (SCR = 1.5).

6.2.1 Paralleled GFL-PMSGs in Strong and Weak Grids

At first, two paralleled 4 MW GFL-PMSGs with the proposed control solution will be studied in this section. A simulation model of two paralleled 4 MW GFL-PMSGs is built to study their stability. The control parameters on the MSC and GSC of the 4 MW GFL-PMSGs are same as that in Table 6.1.

The simulation results of two paralleled 4 MW GFL-PMSGs under grid frequency drop cases are presented in Fig. 6.7. Since the simulation results of two generators are the same, Fig. 6.7 only shows the results of generator 1. In the beginning, given a 0.9 p.u. of power reference at the instant of 1.5s, the active power reaches 0.9 p.u. after around 0.3 seconds. Then, after the grid frequency is dropped to 49.2 Hz at the instant of 2s, the output power does not change due to no frequency support function. However, the GFL-PMSG can provide more reactive power in the weak grid case to support the grid voltage, so the voltage magnitude at the PCC can be maintained nearly 1 p.u.

Moreover, the simulation results of two paralleled 4 MW GFL-PMSGs un-

106

Fig. 6.9: Simulation results of two paralleled 4 MW GFM-PMSGs under grid frequency drop from 50 to 49.2 Hz. (a) A strong grid case (SCR = 15); (b) A weak grid case (SCR = 1.5).

der grid voltage sag cases are presented in Fig. 6.8. Initially, the active power is controlled to be 0.9 p.u. Then, the grid voltage is sagged to 0.2 p.u. and lasts for 0.3 seconds. It shows that the GFL-PMSGs have the ability to ride through the fault in either strong or weak grid cases. However, during the fault recovery period, the proposed method has an overvoltage problem in the weak grid case, which need to be studied further in the future. Furthermore, how to properly manage the input power and the output power to minimize the dc-link voltage fluctuation should be considered in the future.

6.2.2   Paralleled GFM-PMSGs in Strong and Weak Grids

Afterwards, a simulation model of two paralleled 4 MW GFM-PMSGs with the proposed control solution is built, where the control parameters are same as that in Table 6.2. The simulation results of two paralleled 4 MW GFM-PMSGs under grid frequency drop cases are presented in Fig. 6.9. Initially, the active power is controlled to be 0.5 p.u. Then, the grid frequency is
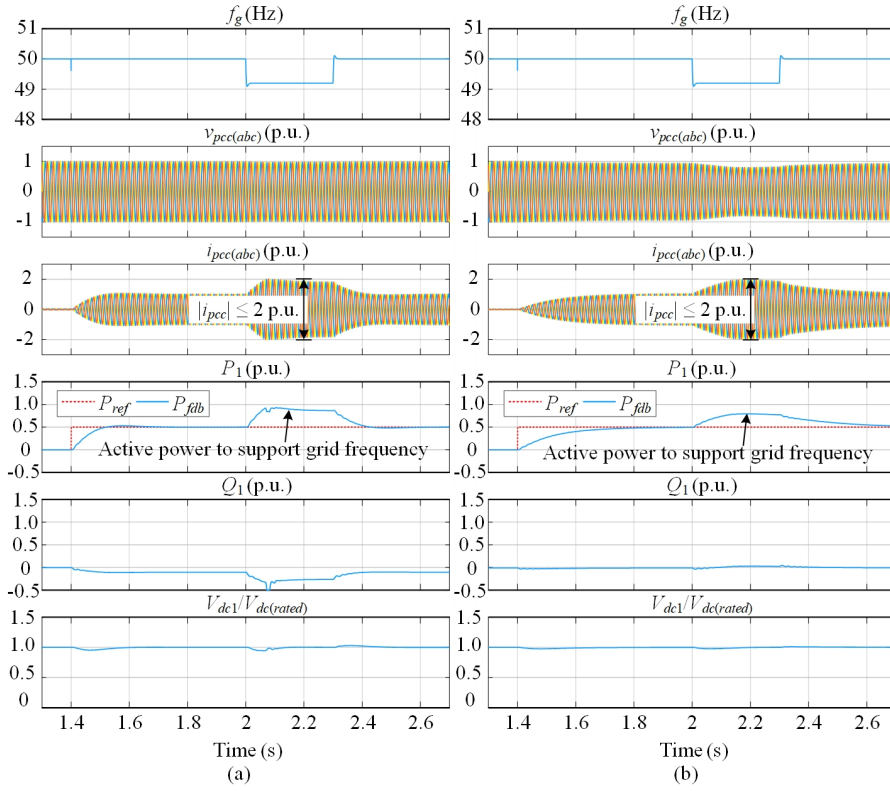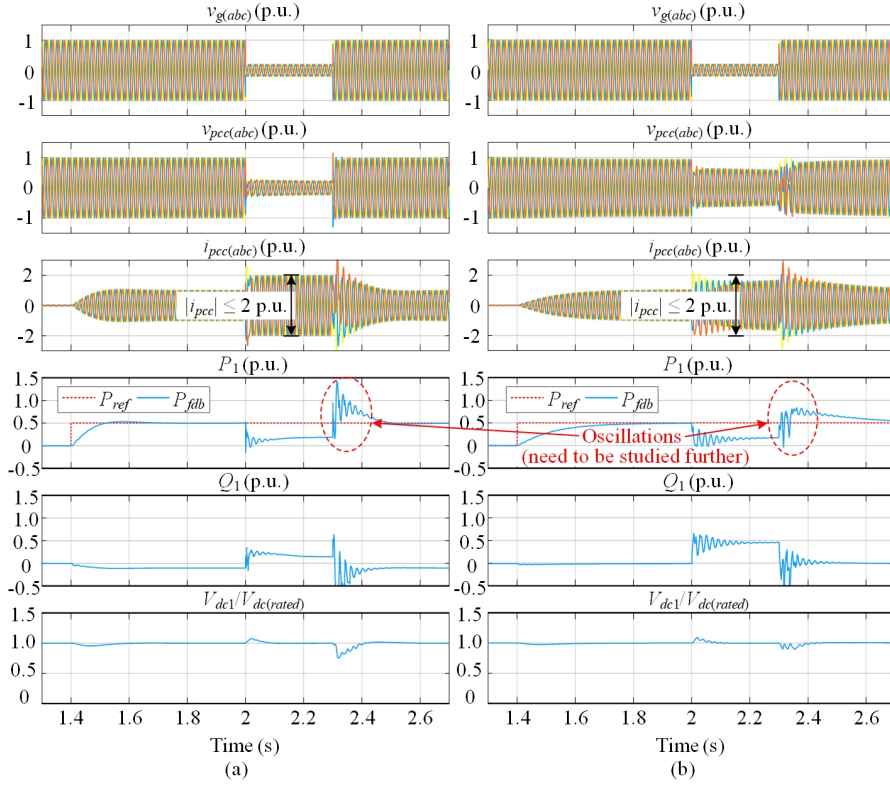
Fig. 6.10: Simulation results of two paralleled 4 MW GFM-PMSGs under grid voltage sag from 1 to 0.2 p.u. (a) A strong grid case (SCR = 15); (b) A weak grid case (SCR = 1.5).

dropped to 49.2 Hz at the instant of 2s. It shows that the GFM-PMSG can provide more active power to support the grid frequency. In addition, the output current of each wind generator can be restricted within 1 p.u., so the total output current of two generators are limited within 2 p.u. Consequently, the converters can operate safely within the rated range of the current.

Moreover, the simulation results of two paralleled 4 MW GFM-PMSGs under grid voltage sag cases are presented in Fig. 6.10. Initially, the active power is controlled to be 0.5 p.u. Then, the grid voltage is sagged to 0.2 p.u. and lasts for 0.3 seconds. The GFM-PMSGs have the ability to ride through the fault in either strong or weak grid cases. In addition, the output current of each wind generator can be restricted within 1 p.u. Thus, the converters can operate safely within the rated range of the current. However, during the fault recovery period, the proposed method has oscillation problems in both weak and strong grid cases. This problem is still a challenge for the GFM converters/wind generators. More exploration is worth doing in the future to find a solution for this problem.

Fig. 6.11: System configuration of 400 MW Anholt Offshore Wind Power Plant [88–90].

6.3   Case 3: Anholt Offshore WPP with Proposed Control Solutions

After analyzing a simple case of two paralleled WT generators connected to a Thevenin equivalent grid in previous sections, this section will study a more complicated case of paralleled WT generators at a larger scale, and the Anholt Offshore Wind Power Plant (WPP) is chosen to be a study case.

According to [88–90], the system configuration of Anholt Offshore WPP is shown in Fig. 6.11, which includes an onshore substation, 85 km transmission lines, an offshore substation, and 12 strings connected with 111 WTs. To simplify the analysis, String 1 with 9 WTs is chosen as an example for study in this thesis. The detailed configuration of String 1 with nine WTs is shown in Fig. 6.12, where the power rating of each WT is defined as 4 MVA [91]. The detailed parameters of the 4 MW PMSG have been provided in Table 6.3. Besides, in Fig. 6.12, "B33" represents the bus of 33 kV. v_{B33} denotes the voltage at the 33 kV bus, and i_{B33} denotes the current through String 1.

Afterwards, the proposed GFL-PMSG and GFM-PMSG control solutions will be applied to paralleled 4 MW WTs in Anholt Offshore WPP. More detailed analysis will be provided in the following sections.

Fig. 6.12: Selected study case of String 1 with 9×4 MW WTs in Anholt Offshore WPP.

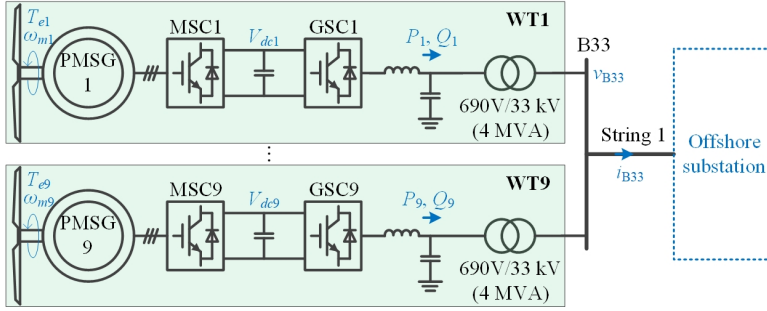## 6.3.1 Case Study of Anholt Offshore WPP with Proposed GFL-PMSG Control Solution

In this section, paralleled GFL-PMSGs with the proposed control solution at a larger scale will be discussed. Same as previous sections, the machine-side dc voltage control approach is used to control the MSC, and the proposed double-PLL-based impedance reshaping control approach is used to control the GSC. A simulation model of nine paralleled 4 MW GFL-PMSGs in a study case of Anholt Offshore WPP is built in MATLAB/Simulink. The control parameters of GFL-PMSGs are same as that in Table 6.1.

The simulation results of nine paralleled 4 MW GFL-PMSGs in the study case of Anholt Offshore WPP under grid voltage sag conditions is presented in Fig. 6.13, where v_{B400} is the three-phase voltage at the 400 kV bus, v_{B33} is the three-phase voltage at the 33 kV bus, and i_{B33} is the three-phase current through String 1. Besides, Q_1, P_1, V_{dc1}, i_{d1}, and i_{q1} are the output reactive power, active power, dc-link voltage, d-component current, and q-component current of the WT1. $P_2 \sim P_9$ are the active power of WT2 $\sim$ WT9, respectively.

As illustrated in Fig. 6.13, initially, given a 0.9 p.u. of power reference for each WT, the output active power of the WT1 $\sim$ WT9 reaches 0.9 p.u. after around 0.3 seconds. Then, the grid voltage is decreased from 1 p.u. to 0.2 p.u. gradually and lasts for 0.2 seconds. During the low-voltage (fault) period, the d-axis current i_d is reduced to zero and the absolute value of the q-axis current i_q is raised to 1 p.u. Meanwhile, the output active power of each WT is reduced to zero since the maximum reactive power is provided. After the grid voltage is recovered to 1 p.u., the output active power of each WT follows the reference and returns to 0.9 p.u. Therefore, the GFL-PMSG with proposed control solutions have the ability to ride through the low-voltage fault. Besides, it shows good stability, steady-state and transient performance in the study case of Anholt Offshore WPP. However, a fluatuation of the dc-link voltage during the fault recovery period can be observed. How to reduce the fluctuation of the dc-link voltage is worth considering in the future.
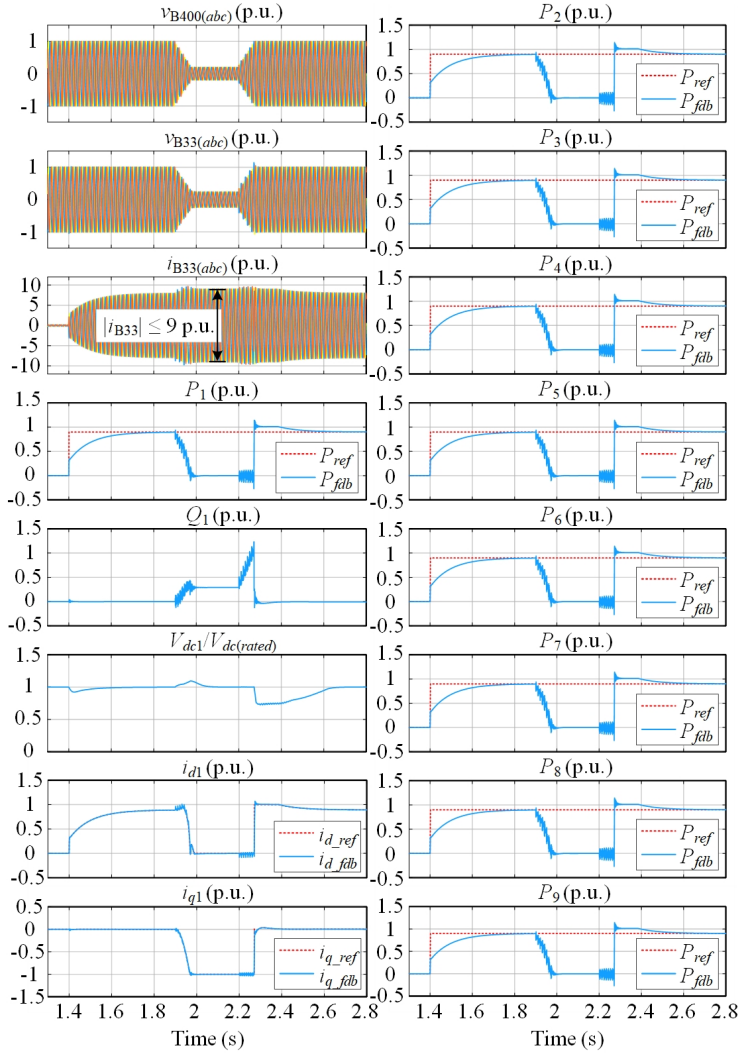
Fig. 6.13: Simulation results of 9×4 MW GFL-PMSGs in selected study case of String 1 under grid voltage sag conditions.

6.3.2 Case Study of Anholt Offshore WPP with Proposed GFM-PMSG Control Solution

Afterwards, paralleled GFM-PMSGs with the proposed control solution at a larger scale will be discussed. Same as previous sections, the machine-side dc voltage control approach is used to control the MSC, and the virtual-admittance-based GFM control approach with the proposed power-angle-based overcurrent protection solution is used to control the GSC. A simu-
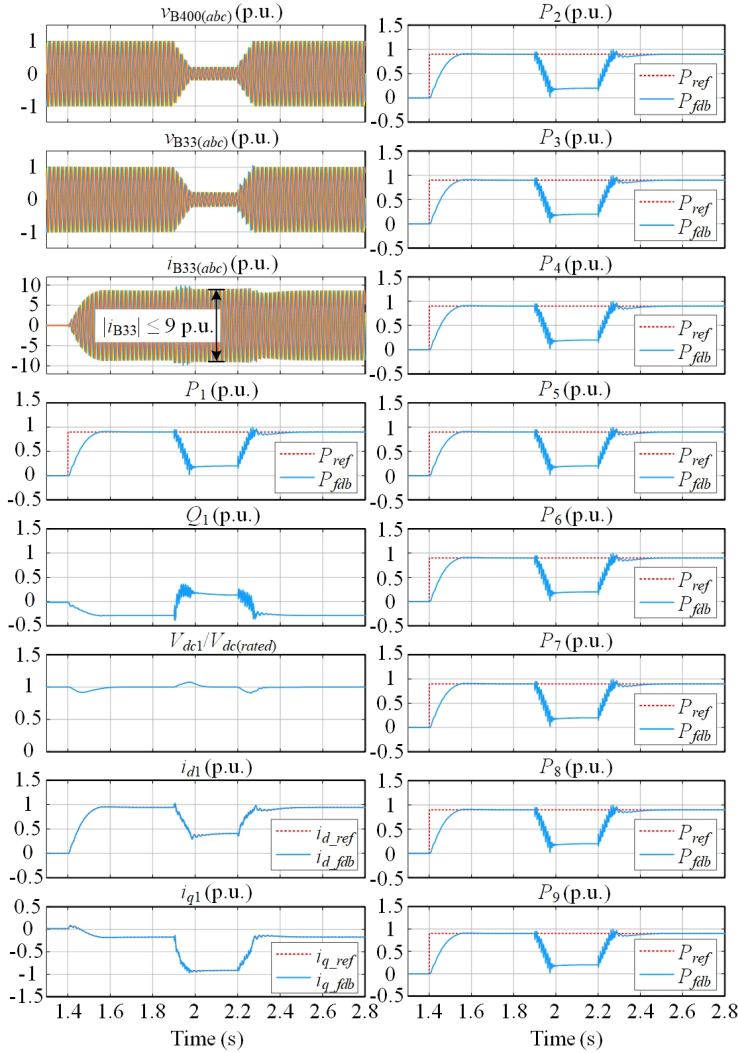
Fig. 6.14: Simulation results of 9×4 MW GFM-PMSGs in selected study case of String 1 under grid voltage sag conditions.

lation model of nine paralleled 4 MW GFM-PMSGs in a study case of Anholt Offshore WPP is built in MATLAB/Simulink. The control parameters of GFM-PMSGs are same as that in Table 6.2.

The simulation results of nine paralleled 4 MW GFM-PMSGs in the study case of Anholt Offshore WPP under grid voltage sag conditions is presented in Fig. 6.14. Initially, given a 0.9 p.u. of power reference for each WT, the output active power of the WT1 $\sim$ WT9 reaches 0.9 p.u. after around 0.2 seconds. Then, the grid voltage is decreased from 1 p.u. to 0.2 p.u. gradually
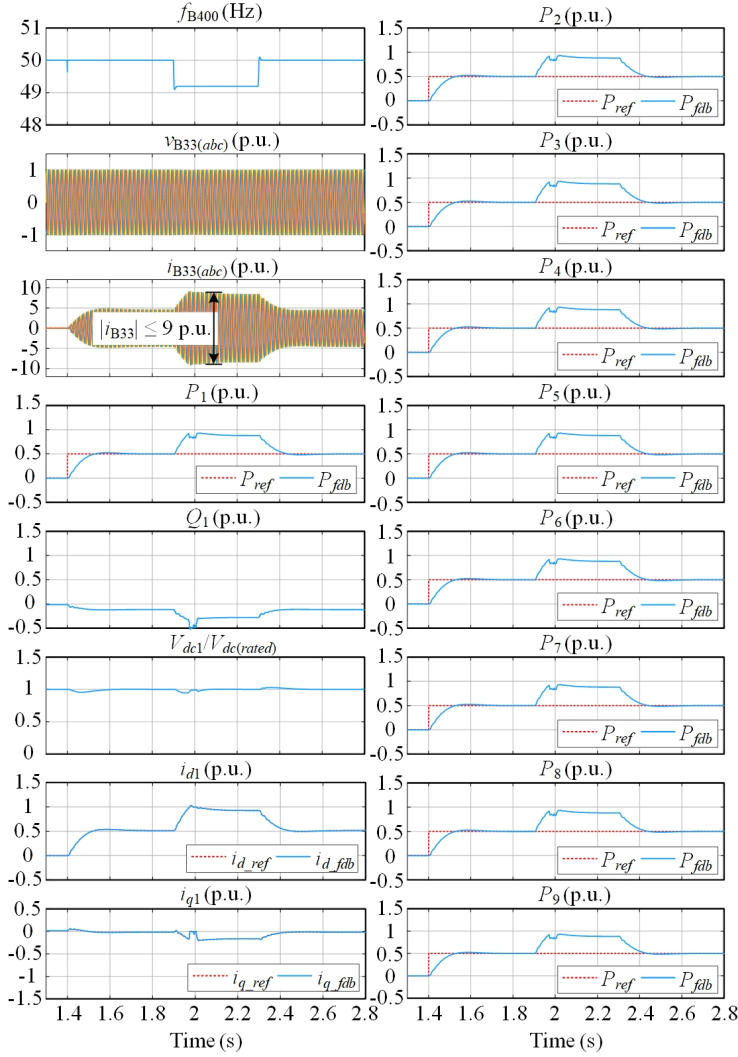
Fig. 6.15: Simulation results of 9×4 MW GFM-PMSGs in selected study case of String 1 under grid frequency drop conditions.

and lasts for 0.2 seconds. During the low-voltage (fault) period, the output active power of each WT is reduced adaptively based on the grid voltage amplitude. After the grid voltage is recovered to 1 p.u., the output active power of each WT follows the reference and returns to 0.9 p.u. In addtion, the output current of each WT is restricted within 1 p.u. (the total output current of nine WTs is limited within 9 p.u.). Therefore, the GFM-PMSG with proposed control solutions have the ability to ride through the low-voltage

fault. Besides, it shows good stability, steady-state and transient performance in the study case of Anholt Offshore WPP.

Moreover, the simulation results of nine paralleled 4 MW GFM-PMSGs in the study case of Anholt Offshore WPP under grid frequency drop conditions is presented in Fig. 6.15, where f_{B400} is the frequency of the grid voltage at the 400 kV bus. Initially, given a 0.5 p.u. of power reference for each WT, the output active power of the WT1 $\sim$ WT9 reaches 0.5 p.u. after around 0.2 seconds. Then, the grid frequency is dropped from 50 Hz to 49.2 Hz at the instant of 1.9s. The output active power of each WT is increased to support the grid frequency. After the grid frequency is recovered to 50 Hz, the output active power of each WT follows the reference and returns to 0.5 p.u. In addtion, the output current of each WT is restricted within 1 p.u. (the total output current of nine WTs is limited within 9 p.u.). Therefore, the GFM-PMSGs with proposed control solutions can protect themselves from overcurrent under large grid frequency disturbances.

At last, it is worth mentioning that the selected study case of String 1 with 9×4 MW WTs in Anholt Offshore WPP is still a stronger grid case. As the number of WTs increases, the grid strength will decrease. Another case of Anholt Offshore WPP including String 1 $\sim$ 12 with 111 WTs is worth studying in the future. However, the calculation burden of that study case by simulation will be heavy. Suitable model aggregation could be considered.

6.4   Summary

This chapter has studied paralleled Type-4 WTs with proposed GFL and GFM control solutions in three cases. At first, a simple case of two paralleled 30 kW WTs connected to a Thevenin equivalent grid is evaluated. Then, a second case of 4 MW WTs is investigated. The simulation results show that two paralleled WTs with either proposed GFL or GFM control solutions have good stability and transient performance in strong and weak grid cases. The GFL-PMSGs can provide voltage support in weak grid cases, while the GFM-PMSGs can provide frequency support during the grid frequency variation period. Thus, the voltage and frequency stability requirements specified in the grid code can be fulfilled. Besides, the WTs can also ride through the low-voltage fault in either a strong or a weak grid case. However, the transient performance during the fault recovery period is still unsatisfactory, which is worth studying further in the future.

Afterwards, a more realistic case of nine paralleled 4 MW WTs in Anholt Offshore WPP is evaluated. It shows that paralleled WTs with either proposed GFL or GFM control solutions have good stability, steady-state and transient performance, which indicates that the proposed methods could be potential control solutions for the WPP with Type-4 WTs.

Chapter 7

Conclusion

The research outputs and main contributions of the thesis are summarized in this chapter. Besides, some possible working directions in the future are also listed in the end.

7.1 Summary of the Thesis

The main research focus of the thesis is to enhance the stability of GFL-based or GFM-based wind generators to make them meet the requirements in the Grid Codes and enable them to operate stably in either strong or weak grid conditions. To this end, several challenging issues have been studied, and some solutions have been proposed. The research outcomes of this thesis are summarized as follows.

In *Chapter 1*, the main problems and challenges of existing wind generators connected to weak grids have been introduced. To address these problems, the research objectives of the thesis are defined accordingly. On one hand, an improved GFL control scheme based on original GFL control scheme needs to be found. On the other hand, an effective GFM control scheme needs to be invented to replace the existing GFL control scheme.

In *Chapter 2*, the instability reason of the conventional GFL inverter is discussed at first. Then, to enhance the small-signal stability of GFL inverters in weak grid cases, a double-PLL-based impedance reshaping control approach is proposed. With this proposed method, the small-signal stability limit can be extended nearly to the static limit. Besides, the bandwidth of the PLL can be designed higher when using this proposed method, which is beneficial for enhancing the transient performance. Thus, both stability and transient performance has been improved.

In *Chapter 3*, the small-signal stability of three typical GFM control approaches is compared initially. It is found that the virtual-admittance-based

GFM inverter has better stability. Then, an SISO stability analysis approach for the virtual-admittance-based GFM inverter is proposed, which can be used for the parameter design of the virtual admittance. In addition, to address the instability problems of GFM inverters with current limitations under large grid disturbances, a power-angle-based adaptive overcurrent protection approach is proposed. With this proposed method, the GFM inverters can operate stably under large grid frequency or voltage disturbances.

In *Chapter 4*, the machine-side dc voltage control approach and the grid-side dc voltage control approach for PMSG-based Type-4 WT generators are compared at first. It is found that the machine-side dc voltage control approach has better performance in weak grid cases. Then, the small-signal impedance models of GFL-PMSGs and GFM-PMSGs are built, and the corresponding impedance characteristics are analyzed. It is found that the PMSG plus MSC in Type-4 WT generators can be simplified to be an ideal voltage or power source, where the model is still accurate from the small-signal perspective. Thus, the simplified model can be used to evaluate a larger-scale system, which is beneficial for shortening the simulation time.

In *Chapter 5*, the small-signal impedance modeling of DFIG-based Type-3 WT generators is studied. To build the full-order small-signal impedance model, a two-port-network-based decoupled impedance modeling method for Type-3 wind generators is proposed, which is effective for both GFL-DFIGs and GFM-DFIGs. With this proposed modeling method, the impact of the RSC, GSC, and dc-link coupling can be analyzed separately.

In *Chapter 6*, two paralleled Type-4 WT generators under strong and weak grid conditions are investigated. It is found that the paralleled WT generators with either the proposed GFL or GFM control solutions can operate stably, which can basically meet the requirements specified in the Grid Codes. Finally, a more realistic study case of String 1 in Anholt Offshore WPP is used to evaluate the performance of the proposed control solutions. The simulation outcomes show good stability, steady-state and transient performance of paralleled Type-4 WT generators with the proposed control solutions at a larger scale.

7.2 Main Contributions

According to the research outcomes above, the main contributions of the thesis can be summarized as follows:

- The maximum power transfer capability of the grid-connected inverter system with different SCRs and grid impedance characteristics is analyzed quantitatively, which shows the potential maximum stability boundary of the system [J1].

- A double-PLL-based impedance reshaping control scheme is proposed to enhance the small-signal stability of GFL inverters in weak grid cases. With this proposed method, the bandwidth of the PLL can be designed higher to improve the transient performance [J2].

- A simple SISO small-signal stability analysis method for GFM inverters with virtual admittance control is proposed, which can be used for the parameter design of the virtual admittance [C5].

- A power-angle-based overcurrent protection method for GFM inverters is proposed to protect the inverters under abnormal grid conditions. With this proposed method, the GFM inverters can operate stably under large grid voltage or frequency disturbances. Besides, the output current is able to be restricted within 1 p.u. effectively [J3].

- A two-port-network-based decoupled impedance modeling method for the Type-3 wind generation system is proposed. With this proposed method, the full-order small-signal impedance model of the Type-3 wind generation system can be built [J5].

- A larger-scale Type-4 wind generation system in a more realistic case of Anholt Offshore WPP is evaluated. The analyses show good stability, steady-state and transient performance of wind generators with the proposed GFL or GFM control solutions, and they can be scaled up to even larger systems.

7.3 Future Work

Currently, the topic of "Modeling, stability, and control of wind power generation systems connected to weak grids" is still a challenging in the research field, which needs the collaboration of people with different background. Therefore, one Ph.D. project may not be enough to address all the challenges. In this Ph.D. thesis, only some challenges regarding the small-signal modeling and stability of Type-3/Type-4 WT generators under symmetrical grid conditions have been addressed and solved. Aside from the work in this thesis, some possible work are worth studying further in the future, which are listed as follows:

- When studying the PMSG and DFIG-based wind generation systems, the rotor speed of the generator is assumed to be constant in this thesis. However, to have a more realistic analysis results, the mechanical part including the WT model, gear box, and drive train system needs to be considered, which is important to be studied in the future.

- As for the power grid, only the symmetrical three-phase grid case is considered in this thesis. In the future, the asymmetrical grid cases (e.g., single-phase grid fault) are worth being studied further. In that case, only considering the positive sequence voltage and current is not enough. Namely, the negative sequence voltage and current also needs to be taken into account.

- As for the grid impedance, only the inductance-dominated case is considered in this thesis. In the future, the resistance-dominated case or the capacitance compensation case is worth being investigated.

- In this thesis, energy storage systems are not included in the WT generator. The impact of energy storage systems on the WT generator is worth being investigated in the future in order to achieve the GFM control more flexibly.

- In this thesis, only the case of pure GFL wind generators or pure GFM wind generators is studied. The case of mixed GFL wind generators and GFM wind generators is worth being explored in the future in order to achieve an optimal mixed solution.

- This thesis mainly focuses on the small-signal stability of grid-connected wind generators. In the future, the large-signal transient stability of wind generation systems is worth being explored, especially for the recovery moment of the low-voltage fault.

- Type-4 WT generators with the proposed GFL and GFM control solutions have been studied thoroughly in the thesis. However, the effect of the proposed control solutions on Type-3 WT generators needs to be analyzed further in the future.

- The stability of paralleled WTs at a farm-level (e.g., more than 100 WTs) is an interesting research topic, which needs to be studied in the future.

- Further improvement of the developed model to meet other requirements specified in the Grid Codes needs to be done consistently.

Bibliography

References

[1] F. Blaabjerg, Y. Yang, D. Yang, and X. Wang, "Distributed power-generation systems and protection," *Proc. IEEE*, vol. 105, no. 7, pp. 1311–1331, Jul. 2017.

[2] "Future of Wind: Deployment, investment, technology, grid integration and socio-economic aspects," International Renewable Energy Agency, Tech. Rep., 2019. [Online]. Available: https://www.irena.org/publications/2019/Oct/Future-of-wind

[3] "Getting fit for 55 and set for 2050," European Technology & Innovation Platform on Wind Energy, Tech. Rep., 2021. [Online]. Available: https://etipwind.eu/publications/getting-fit-for-55/

[4] "Denmark's Energy and Climate Outlook 2020," Danish Energy Agency, Tech. Rep., 2020. [Online]. Available: https://ens.dk/en/our-services/projections-and-models/denmarks-energy-and-climate-outlook

[5] "High Penetration of Power Electronic Interfaced Power Sources and the Potential Contribution of Grid Forming Converters," European Network of Transmission System Operators, Tech. Rep., 2020. [Online]. Available: https://www.entsoe.eu/events/2020/01/30/workshop-on-high-penetration-of-power-electronic-interfaced-power-sources-and-the-potential-contribution-of-grid-forming-converters/

[6] "System Operability Framework 2015," National Grid, Tech. Rep., 2015. [Online]. Available: https://www.nationalgrideso.com/document/63461/download

[7] D. Yang, X. Wang, F. Liu, K. Xin, Y. Liu, and F. Blaabjerg, "Adaptive reactive power control of PV power plants for improved power transfer capability under ultra-weak grid conditions," *IEEE Trans. Smart Grid*, vol. 10, no. 2, pp. 1269–1279, Mar. 2019.

[8] Y. Cheng, L. Fan, J. Rose, F. Huang, J. Schmall, X. Wang, X. Xie, J. Shair, J. Ramamurthy, N. Modi, C. Li, C. Wang, S. Shah, B. C. Pal, Z. Miao, A. Isaacs, J. Mahseredjian, and Z. J. Zhou, "Real-world subsynchronous oscillation events in power grids with high penetrations of inverter-based resources," *IEEE Trans. Power Syst.*, vol. 38, no. 1, pp. 316–330, Jan. 2023.

[9] N. Hatziargyriou, J. Milanovic, C. Rahmann, V. Ajjarapu, C. Canizares, I. Erlich, D. Hill, I. Hiskens, I. Kamwa, B. Pal, P. Pourbeik, J. Sanchez-Gasca, A. Stankovic, T. Van Cutsem, V. Vittal, and C. Vournas, "Definition and classification of power system stability – revisited & extended," *IEEE Trans. Power Syst.*, vol. 36, no. 4, pp. 3271–3281, Jul. 2021.

[10] X. Wang, M. G. Taul, H. Wu, Y. Liao, F. Blaabjerg, and L. Harnefors, "Grid-synchronization stability of converter-based resources – an overview," *IEEE Open J. Ind. Applicat.*, vol. 1, pp. 115–134, 2020.

[11] A. Basit, A. D. Hansen, I. Margaris, and J. C. Hansen, "A review of grid requirements for wind farm in Denmark and China," in *China Wind Power 2012*, Beijing, China, 2012, pp. 1–7.

[12] "The Grid Code," National Grid, Tech. Rep., 2022. [Online]. Available: https://www.nationalgrideso.com/industry-information/codes/grid-code/code-documents

[13] "System Operability Framework 2016," National Grid, Tech. Rep., 2016. [Online]. Available: https://www.nationalgrideso.com/document/63481/download

[14] "CM088 - Fault Ride Through Definition," National Grid, Tech. Rep., 2023. [Online]. Available: https://www.nationalgrideso.com/industry-information/codes/system-operator-transmission-owner-code-stc-old/modifications/cm088

[15] "GC0111 - Fast Fault Current Injection Specification Text," National Grid, Tech. Rep., 2020. [Online]. Available: https://www.nationalgrideso.com/codes/grid-code/modifications/gc0111-fast-fault-current-injection-specification-text

[16] "Great Britain power system disruption on 9 August 2019: interim report," Department for Business, Energy & Industrial Strategy, Tech. Rep., 2019. [Online]. Available: https://www.gov.uk/government/publications/great-britain-power-system-disruption-review

[17] R. Datta and V. Ranganathan, "Variable-speed wind power generation using doubly fed wound rotor induction machine – a comparison with

alternative schemes," *IEEE Trans. Energy Conv.*, vol. 17, no. 3, pp. 414–421, Sep. 2002.

[18] B. Wu, Y. Lang, N. Zargari, and S. Kouro, *Power Conversion and Control of Wind Energy Systems*. Wiley-IEEE Press, Aug. 2011.

[19] F. Blaabjerg and K. Ma, "Future on power electronics for wind turbine systems," *IEEE J. Emerg. Sel. Topics Power Electron.*, vol. 1, no. 3, pp. 139–152, Sep. 2013.

[20] A. Kushwaha and I. Singh, "Literature review paper on doubly fed induction generator wind turbine technology," *Int. J. Enh. Res. Sci. Tech. Eng.*, vol. 2, no. 9, pp. 44–50, Sep. 2013.

[21] E. Muljadi and A. Ellis, "Final Project Report WECC Wind Generator Development," National Renewable Energy Laboratory, Tech. Rep., 2010. [Online]. Available: https://escholarship.org/uc/item/02c6h0sm

[22] D. Zhou, F. Blaabjerg, M. Lau, and M. Tonnes, "Optimized reactive power flow of DFIG power converters for better reliability performance considering grid codes," *IEEE Trans. Ind. Electron.*, vol. 62, no. 3, pp. 1552–1562, Mar. 2015.

[23] A. Yogarathinam, J. Kaur, and N. R. Chaudhuri, "Impact of inertia and effective short circuit ratio on control of frequency in weak grids interfacing LCC-HVDC and DFIG-based wind farms," *IEEE Trans. Power Delivery*, vol. 32, no. 4, pp. 2040–2051, Aug. 2017.

[24] J. Kim, S. H. Lee, and J.-W. Park, "Inertia-free stand-alone microgrid – part II: inertia control for stabilizing dc-link capacitor voltage of PMSG wind turbine system," *IEEE Trans. Ind. Applicat.*, vol. 54, no. 5, pp. 4060–4068, Sep. 2018.

[25] E. Ebrahimzadeh, F. Blaabjerg, T. Lund, J. Godsk Nielsen, and P. Carne Kjær, "Modelling and stability analysis of wind power plants connected to weak grids," *Appl. Sci.*, vol. 9, no. 21, p. 4695, Nov. 2019.

[26] M. Davari and Y. A.-R. I. Mohamed, "Robust dc-link voltage control of a full-scale pmsg wind turbine for effective integration in dc grids," *IEEE Trans. Power Electron.*, vol. 32, no. 5, pp. 4021–4035, May 2017.

[27] A. H. Kasem Alaboudy, A. A. Daoud, S. S. Desouky, and A. A. Salem, "Converter controls and flicker study of PMSG-based grid connected wind turbines," *Ain Shams Eng. J.*, vol. 4, no. 1, pp. 75–91, Mar. 2013.

[28] G. O. Kalcon, G. P. Adam, O. Anaya-Lara, S. Lo, and K. Uhlen, "Small-signal stability analysis of multi-terminal VSC-based dc transmission

systems," *IEEE Trans. Power Syst.*, vol. 27, no. 4, pp. 1818–1830, Nov. 2012.

[29] L. Xu and L. Fan, "Impedance-based resonance analysis in a VSC-HVDC system," *IEEE Trans. Power Delivery*, vol. 28, no. 4, pp. 2209–2216, Oct. 2013.

[30] Y. Li, Y. Gu, Y. Zhu, A. Junyent-Ferre, X. Xiang, and T. C. Green, "Impedance circuit model of grid-forming inverter: visualizing control algorithms as circuit elements," *IEEE Trans. Power Electron.*, vol. 36, no. 3, pp. 3377–3395, Mar. 2021.

[31] H. Gong, D. Yang, and X. Wang, "Impact analysis and mitigation of synchronization dynamics for dq impedance measurement," *IEEE Trans. Power Electron.*, vol. 34, no. 9, pp. 8797–8807, Sep. 2019.

[32] J. Sun, "Impedance-based stability criterion for grid-connected inverters," *IEEE Trans. Power Electron.*, vol. 26, no. 11, pp. 3075–3078, Nov. 2011.

[33] L. Harnefors, "Modeling of three-phase dynamic systems using complex transfer functions and transfer matrices," *IEEE Trans. Ind. Electron.*, vol. 54, no. 4, pp. 2239–2248, Aug. 2007.

[34] A. Rygg, M. Molinas, C. Zhang, and X. Cai, "A modified sequence-domain impedance definition and its equivalence to the dq-domain impedance definition for the stability analysis of ac power electronic systems," *IEEE J. Emerg. Sel. Top. Power Electron.*, vol. 4, no. 4, pp. 1383–1396, Dec. 2016.

[35] X. Wang, L. Harnefors, and F. Blaabjerg, "Unified impedance model of grid-connected voltage-source converters," *IEEE Trans. Power Electron.*, vol. 33, no. 2, pp. 1775–1787, Feb. 2018.

[36] C. Zhang, X. Cai, A. Rygg, and M. Molinas, "Sequence domain SISO equivalent models of a grid-tied voltage source converter system for small-signal stability analysis," *IEEE Trans. Energy Convers.*, vol. 33, no. 2, pp. 741–749, Jun. 2018.

[37] G. Wu, H. Sun, X. Zhang, A. Egea-Alvarez, B. Zhao, S. Xu, S. Wang, and X. Zhou, "Parameter design oriented analysis of the current control stability of the weak-grid-tied VSC," *IEEE Trans. Power Delivery*, vol. 36, no. 3, pp. 1458–1470, Jun. 2021.

[38] Y. Li, L. Fan, and Z. Miao, "Stability control for wind in weak grids," *IEEE Trans. Sustain. Energy*, vol. 10, no. 4, pp. 2094–2103, Oct. 2019.

[39] J. F. Morris, K. H. Ahmed, and A. Egea-Alvarez, "Analysis of controller bandwidth interactions for vector-controlled VSC connected to very weak ac grids," *IEEE J. Emerg. Sel. Top. Power Electron.*, vol. 9, no. 6, pp. 7343–7354, Dec. 2021.

[40] B. Wen, D. Boroyevich, R. Burgos, P. Mattavelli, and Z. Shen, "Analysis of d-q small-signal impedance of grid-tied inverters," *IEEE Trans. Power Electron.*, vol. 31, no. 1, pp. 675–687, Jan. 2016.

[41] A. Egea-Alvarez, S. Fekriasl, F. Hassan, and O. Gomis-Bellmunt, "Advanced vector control for voltage source converters connected to weak grids," *IEEE Trans. Power Syst.*, vol. 30, no. 6, pp. 3072–3081, Nov. 2015.

[42] D. Yang, X. Wang, F. Liu, K. Xin, Y. Liu, and F. Blaabjerg, "Symmetrical PLL for SISO impedance modeling and enhanced stability in weak grids," *IEEE Trans. Power Electron.*, vol. 35, no. 2, pp. 1473–1483, Feb. 2020.

[43] R. Rosso, X. Wang, M. Liserre, X. Lu, and S. Engelken, "Grid-forming converters: control approaches, grid-synchronization, and future trends – a review," *IEEE Open J. Ind. Applicat.*, vol. 2, pp. 93–109, 2021.

[44] S. D'Arco and J. A. Suul, "Virtual synchronous machines – classification of implementations and analysis of equivalence to droop controllers for microgrids," in *IEEE Gren. Conf.*, Grenoble, France, Jun. 2013, pp. 1–7.

[45] Q. Zhong, P. Nguyen, Z. Ma, and W. Sheng, "Self-synchronized synchronverters: inverters without a dedicated synchronization unit," *IEEE Trans. Power Electron.*, vol. 29, no. 2, pp. 617–630, Feb. 2014.

[46] H. Bevrani, T. Ise, and Y. Miura, "Virtual synchronous generators: a survey and new perspectives," *Int. J. Electric. Power Energy Syst.*, vol. 54, pp. 244–254, Jan. 2014.

[47] L. Zhang, L. Harnefors, and H.-P. Nee, "Power-synchronization control of grid-connected voltage-source converters," *IEEE Trans. Power Syst.*, vol. 25, no. 2, pp. 809–820, May 2010.

[48] W. Zhang, A. M. Cantarellas, J. Rocabert, A. Luna, and P. Rodriguez, "Synchronous power controller with flexible droop characteristics for renewable power generation systems," *IEEE Trans. Sustain. Energy*, vol. 7, no. 4, pp. 1572–1582, Oct. 2016.

[49] D. Gros, M. Colombino, J.-S. Brouillon, and F. Dorfler, "The effect of transmission-line dynamics on grid-forming dispatchable virtual oscillator control," *IEEE Trans. Contr. Netw. Syst.*, vol. 6, no. 3, pp. 1148–1160, Sep. 2019.

[50] J. Rocabert, A. Luna, F. Blaabjerg, and P. Rodríguez, "Control of power converters in AC microgrids," *IEEE Trans. Power Electron.*, vol. 27, no. 11, pp. 4734–4749, Nov. 2012.

[51] K. Yu, Q. Ai, S. Wang, J. Ni, and T. Lv, "Analysis and optimization of droop controller for microgrid system based on small-signal dynamic model," *IEEE Trans. Smart Grid*, vol. 7, no. 2, pp. 695–705, Mar. 2016.

[52] S. Wang, Z. Liu, J. Liu, D. Boroyevich, and R. Burgos, "Small-signal modeling and stability prediction of parallel droop-controlled inverters based on terminal characteristics of individual inverters," *IEEE Trans. Power Electron.*, vol. 35, no. 1, pp. 1045–1063, Jan. 2020.

[53] H. Wu and X. Wang, "A mode-adaptive power-angle control method for transient stability enhancement of virtual synchronous generators," *IEEE J. Emerg. Sel. Top. Power Electron.*, vol. 8, no. 2, pp. 1034–1049, Jun. 2020.

[54] E. Rokrok, T. Qoria, A. Bruyere, B. Francois, and X. Guillaud, "Transient stability assessment and enhancement of grid-forming converters embedding current reference saturation as current limiting strategy," *IEEE Trans. Power Syst.*, vol. 37, no. 2, pp. 1519–1531, Mar. 2022.

[55] K. O. Oureilidis and C. S. Demoulias, "A fault clearing method in converter-dominated microgrids with conventional protection means," *IEEE Trans. Power Electron.*, vol. 31, no. 6, pp. 4628–4640, Jun. 2016.

[56] T. Liu, X. Wang, F. Liu, K. Xin, and Y. Liu, "A current limiting method for single-loop voltage-magnitude controlled grid-forming converters during symmetrical faults," *IEEE Trans. Power Electron.*, vol. 37, no. 4, pp. 4751–4763, Apr. 2022.

[57] A. D. Paquette and D. M. Divan, "Virtual impedance current limiting for inverters in microgrids with synchronous generators," *IEEE Trans. Ind. Applicat.*, vol. 51, no. 2, pp. 1630–1638, Mar. 2015.

[58] M. G. Taul, X. Wang, P. Davari, and F. Blaabjerg, "Current limiting control with enhanced dynamics of grid-forming converters during fault conditions," *IEEE J. Emerg. Sel. Top. Power Electron.*, vol. 8, no. 2, pp. 1062–1073, Jun. 2020.

[59] L. Huang, H. Xin, Z. Wang, L. Zhang, K. Wu, and J. Hu, "Transient stability analysis and control design of droop-controlled voltage source converters considering current limitation," *IEEE Trans. Smart Grid*, vol. 10, no. 1, pp. 578–591, Jan. 2019.

[60] W. Du, R. H. Lasseter, and A. S. Khalsa, "Survivability of autonomous microgrid during overload events," *IEEE Trans. Smart Grid*, vol. 10, no. 4, pp. 3515–3524, Jul. 2019.

[61] J. A. Suul, S. D'Arco, P. Rodríguez, and M. Molinas, "Impedance-compensated grid synchronisation for extending the stability range of weak grids with voltage source converters," *IET Gen. Transm. Distr.*, vol. 10, no. 6, pp. 1315–1326, Apr. 2016.

[62] Y. Liao and X. Wang, "Stationary-frame complex-valued frequency-domain modeling of three-phase power converters," *IEEE J. Emerg. Sel. Top. Power Electron.*, vol. 8, no. 2, pp. 1922–1933, Jun. 2020.

[63] R. Rosso, G. Buticchi, M. Liserre, Z. Zou, and S. Engelken, "Stability analysis of synchronization of parallel power converters," in *43rd Ann. Conf. IEEE Ind. Electron. Soc. (IECON)*, Beijing, China, 2017, pp. 440–445.

[64] K. M. Alawasa, Y. A.-R. I. Mohamed, and W. Xu, "Active mitigation of subsynchronous interactions between PWM voltage-source converters and power networks," *IEEE Trans. Power Electron.*, vol. 29, no. 1, pp. 121–134, Jan. 2014.

[65] J. Fang, X. Li, H. Li, and Y. Tang, "Stability improvement for three-phase grid-connected converters through impedance reshaping in quadrature-axis," *IEEE Trans. Power Electron.*, vol. 33, no. 10, pp. 8365–8375, Oct. 2018.

[66] M. Li, X. Zhang, Z. Guo, J. Wang, Y. Wang, F. Li, and W. Zhao, "The control strategy for the grid-connected inverter through impedance re-shaping in q-axis and its stability analysis under a weak grid," *IEEE J. Emerg. Sel. Top. Power Electron.*, vol. 9, no. 3, pp. 3229–3242, Jun. 2021.

[67] S. D'silva, M. Shadmand, S. Bayhan, and H. Abu-Rub, "Towards grid of microgrids: seamless transition between grid-connected and islanded modes of operation," *IEEE Open J. Ind. Electron. Soc.*, vol. 1, pp. 66–81, 2020.

[68] D. B. Rathnayake, M. Akrami, C. Phurailatpam, S. P. Me, S. Hadavi, G. Jayasinghe, S. Zabihi, and B. Bahrani, "Grid forming inverter modeling, control, and applications," *IEEE Access*, vol. 9, pp. 114 781–114 807, 2021.

[69] K. M. Cheema, "A comprehensive review of virtual synchronous generator," *Int. J. Electric. Power Energy Syst.*, vol. 120, p. 106006, Sep. 2020.

[70] W. Du, Z. Chen, K. P. Schneider, R. H. Lasseter, S. Pushpak Nandanoori, F. K. Tuffner, and S. Kundu, "A comparative study of two widely used

grid-forming droop controls on microgrid small-signal stability," *IEEE J. Emerg. Sel. Top. Power Electron.*, vol. 8, no. 2, pp. 963–975, Jun. 2020.

[71] Y. Liao, X. Wang, F. Liu, K. Xin, and Y. Liu, "Sub-synchronous control interaction in grid-forming VSCs with droop control," in *4th IEEE Worksh. Electron. Grid (eGRID)*, Xiamen, China, Nov. 2019, pp. 1–6.

[72] J. C. Vasquez, J. M. Guerrero, M. Savaghebi, J. Eloy-Garcia, and R. Teodorescu, "Modeling, analysis, and design of stationary-reference-frame droop-controlled parallel three-phase voltage source inverters," *IEEE Trans. Ind. Electron.*, vol. 60, no. 4, pp. 1271–1280, Apr. 2013.

[73] J. He and Y. W. Li, "Analysis, design, and implementation of virtual impedance for power electronics interfaced distributed generation," *IEEE Trans. Ind. Applicat.*, vol. 47, no. 6, pp. 2525–2538, Nov. 2011.

[74] Y. Guan, J. M. Guerrero, X. Zhao, J. C. Vasquez, and X. Guo, "A new way of controlling parallel-connected inverters by using synchronous-reference-frame virtual impedance loop – part I: control principle," *IEEE Trans. Power Electron.*, vol. 31, no. 6, pp. 4576–4593, Jun. 2016.

[75] P. Rodriguez, I. Candela, and A. Luna, "Control of PV generation systems using the synchronous power controller," in *IEEE Energy Conv. Congr. Exp. (ECCE)*, Denver, CO, USA, Sep. 2013, pp. 993–998.

[76] H. Xin, L. Huang, L. Zhang, Z. Wang, and J. Hu, "Synchronous instability mechanism of P-f droop-controlled voltage source converter caused by current saturation," *IEEE Trans. Power Syst.*, vol. 31, no. 6, pp. 5206–5207, Nov. 2016.

[77] G. Francis, R. Burgos, D. Boroyevich, F. Wang, and K. Karimi, "An algorithm and implementation system for measuring impedance in the D-Q domain," in *IEEE Energy Conv. Congr. Exp. (ECCE)*, Phoenix, AZ, USA, Sep. 2011, pp. 3221–3228.

[78] J. Hu, Y. Huang, D. Wang, H. Yuan, and X. Yuan, "Modeling of grid-connected DFIG-based wind turbines for DC-link voltage stability analysis," *IEEE Trans. Sustain. Energy*, vol. 6, no. 4, pp. 1325–1336, Oct. 2015.

[79] Y. Xu, H. Nian, T. Wang, L. Chen, and T. Zheng, "Frequency coupling characteristic modeling and stability analysis of doubly fed induction generator," *IEEE Trans. Energy Convers.*, vol. 33, no. 3, pp. 1475–1486, Sep. 2018.

[80] I. Vieto and J. Sun, "Sequence impedance modeling and analysis of type-III wind turbines," *IEEE Trans. Energy Convers.*, vol. 33, no. 2, pp. 537–545, Jun. 2018.

[81] W. Jin and Y. Lu, "Stability analysis and oscillation mechanism of the DFIG-based wind power system," *IEEE Access*, vol. 7, pp. 88 937–88 948, 2019.

[82] K. Sun, W. Yao, J. Fang, X. Ai, J. Wen, and S. Cheng, "Impedance modeling and stability analysis of grid-connected DFIG-based wind farm with a VSC-HVDC," *IEEE J. Emerg. Sel. Top. Power Electron.*, vol. 8, no. 2, pp. 1375–1390, Jun. 2020.

[83] B. Wang, R. Burgos, and B. Wen, "Grid-forming inverter control strategy with improved fault ride through capability," in *IEEE Energy Conv. Congr. Exp. (ECCE)*, Detroit, MI, USA, 2022, pp. 1–8.

[84] "Preset model of permanent magnet synchronous machine: No. 15," 2023. [Online]. Available: https://se.mathworks.com/help/sps/powersys/ref/permanentmagnetsynchronousmachine.html

[85] J. F. Morris, K. H. Ahmed, and A. Egea, "Standardized assessment framework for design and operation of weak AC grid-connected VSC controllers," *IEEE Access*, vol. 9, pp. 95 282–95 293, 2021.

[86] H. Wu, "Small-signal and transient stability analysis of voltage-source converters," Ph.D. Thesis, Aalborg University, Aalborg, Denmark, 2020.

[87] A. Avazov, F. Colas, J. Beerten, and X. Guillaud, "Application of input shaping method to vibrations damping in a Type-IV wind turbine interfaced with a grid-forming converter," *Electr. Power Syst. Res.*, vol. 210, p. 108083, Sep. 2022.

[88] L. H. Kocewiak, B. L. O. Kramer, O. Holmstrøm, K. H. Jensen, and L. Shuai, "Resonance damping in array cable systems by wind turbine active filtering in large offshore wind power plants," *IET Renew. Power Gen.*, vol. 11, no. 7, pp. 1069–1077, Jun. 2017.

[89] C. F. Jensen, "Harmonic background amplification in long asymmetrical high voltage cable systems," *Electr. Power Syst. Res.*, vol. 160, pp. 292–299, Jul. 2018.

[90] M. G. Taul, "Synchronization stability of grid-connected converters under grid faults," Ph.D. Thesis, Aalborg University, Aalborg, Denmark, 2020.

[91] J. N. Nielsen, V. Akhmatov, J. Thisted, E. Grøndahl, P. Egedal, M. N. Frydensbjerg, and K. H. Jensen, "Modelling and fault-ride-trough tests of Siemens wind power 3.6 MW variable-speed wind turbines," *Wind Eng.*, vol. 31, no. 6, pp. 441–452, Dec. 2007.